University College London

Mixing of complex oral health products: experimental and computational fluid dynamics investigations

by

Martí Cortada García

Submitted to the Department of Chemical Engineering
in partial fulfilment of the requirements for the degree of

Doctor of Philosophy in Chemical Engineering

at University College London

December 2018

I, Martí Cortada García confirm that the work presented in this thesis is my own. Where information has been derived from other sources, I confirm that this has been indicated in the thesis.

Acknowledgements

I would like to acknowledge the precious help of my academic supervisors, Prof. Panagiota Angeli and Dr. Luca Mazzei, for their advice and guidance during the whole duration of my PhD and for all the opportunities they gave me to disseminate my work. I would also like to express gratitude to my industrial supervisor, Dr. Valentina Dore, for her support during these years and for all the efforts she made to always make me feel part of GSK.

I wish to thank Dr. Weheliye Hashi Weheliye for his guidance setting up the optically based experiments, and Dr. Rashid Jamshidi for his invaluable help with the numerical simulations. I also wish to thank Simona Migliozzi for her help in the laboratory and with rheological-related considerations, and all the other members of the Advanced Multiphase Systems (ThAMeS) group and the 311 team for all the good times we shared.

I also want to thank Andrew Milner, Dr. Robert Sochon, Edward Mason and Laura Miles for their help in the GSK laboratory.

Per acabar, m'agradaria donar les gràcies a tota la gent de l'àmbit més personal que m'ha donat suport incondicional durant aquests quatre anys: als meus pares, Joaquim i Asun, als meus germans, Joan i Víctor, als meus avis, incloent-hi els que ja no hi són amb nosaltres, Blas, Clotilde, Lorea i Joaquim, i sobretot a la meva parella, Ariadna.

Abstract

The objective of this research is to provide insight into the mixing process of glycerol with a gel made of carbomer and Polyethylene glycol, which is a critical step in the manufacturing of non-aqueous toothpastes. Computational fluid dynamics (CFD) was used as a diagnostics tool, and experimental work was needed to validate the CFD models. First, the applicability of CFD was assessed in a simple stirred tank equipped with a Rushton turbine, and the computational model was validated against accurate experiments of power requirement for agitation obtained with the combination of an air bearing and a load cell. Then, a more geometrically similar mixing tank to the pilot plant scale mixer was built, and a CFD model was implemented to study the flow behaviour of two different mixtures of glycerol and the carbomer gel. The simulations indicated that the mixer prevents the formation of stagnant zones, the angular velocity component is notably greater than the other two components, and the velocity magnitude of the fluid decays fast away from the blades of the impeller. These simulations were validated with the particle image velocimetry (PIV) technique. The mixing time of different mixtures with passive tracers was studied using the previous CFD model, which was modified to include the transport of species equation. The simulation time was prohibitively long, and the alternative approach of studying the mixing time with a Lagrangian particle tracking method was also attempted. The mixing time was evaluated experimentally using the planar laser induced fluorescence (PLIF) technique. Finally, the mixing performance was assessed by means of the Poincaré maps and stretching fields.

Impact statement

This work originated from the industrial need of understanding the mechanisms of mixing complex non-Newtonian fluids in the Oral Health industry, and the output of this work helps to better understand this particular process. In this research, CFD was used as a tool to obtain relevant knowledge of the mixing process of glycerol and carbomer gel, and experimental work was conducted to validate the different models implemented in CFD.

The initial objective of this research was to develop a CFD model of a pilot plant scale mixer used in the GlaxoSmithKline Consumer Healthcare facilities to optimise the production strategy of non-aqueous toothpastes. Due to the geometrical complexity of the system and the working fluids, and the duration of the mixing process, this objective was broken down into intermediate steps, and it was clear since early stages that further research would be needed to attain the primary goal. For this reason, a new grant was awarded to the CORAL group, a multidisciplinary team at UCL lead by Prof. Angeli, to continue and expand the research on this field.

As part of this thesis, extensive experimental work was conducted at the GlaxoSmithKline Consumer Healthcare facilities in Weybridge to determine a constitutive equation that relates the viscosity of a mixture of carbomer gel and glycerol at different temperatures and shear rates. So far, this database has been used by members of the Process Engineering team at GSK Consumer Healthcare as a validating tool for new production strategies, as the rheological properties of this mixture are critical for the success of the final product.

This research lead to two publications in academic journals:

CORTADA-GARCIA, M., DORE, V., MAZZEI, L. & ANGELI, P. 2017. Experimental and CFD studies of power consumption in the agitation of highly viscous shear thinning fluids. *Chemical Engineering Research and Design,* 119**,** 171-182. (Cortada-Garcia et al., 2017).

CORTADA-GARCIA, M., WEHELIYE, W. H., DORE, V., MAZZEI, L. & ANGELI, P. 2018. Computational fluid dynamic studies of mixers for highly viscous shear thinning fluids and PIV validation. *Chemical Engineering Science,* 179**,** 133-149. (Cortada-Garcia et al., 2018).

Additionally, I was able to disseminate this work in the following international conferences:

- American Physical Society 68th Annual DFD Meeting, Boston, MA, USA, 2015.
- 11th European Fluid Mechanics Conference, Seville, Spain, 2016
- American Institute of Chemical Engineering Annual Meeting, San Francisco, CA, USA, 2016.
- International Symposium on Mixing in Industrial Processes IX, Birmingham, UK, 2017
- 10th World Congress of Chemical Engineering, Barcelona, Spain, 2017. I was awarded with the “Best poster presentation in the CFD in Chemical Engineering Symposium”.

Contents

Acknowledgements ... 5

Abstract ... 7

Impact statement ... 9

Contents ... 11

List of Figures ... 16

List of Tables ... 21

1. Introduction ... 23
  - 1.1. Background ... 23
  - 1.2. Motivation ... 25
  - 1.3. Objectives ... 26
  - 1.4. Description of the system to study ... 27
  - 1.5. Structure ... 28

2. Literature review ... 31
  - 2.1. Stirred tanks ... 31
  - 2.2. Fluid rheology ... 34
    - 2.2.1. Generalised Newtonian fluids ... 36
    - 2.2.2. Viscoelastic fluid behaviour ... 39
  - 2.3. Computational Fluid Dynamics ... 42
    - 2.3.1. Generalities ... 42
    - 2.3.2. Basic equations of fluid flow ... 43
    - 2.3.3. Rotating boundaries in CFD ... 44
    - 2.3.4. Modelling single phase multicomponent flows ... 46
  - 2.4. Relevant literature of CFD applied to mixing tanks ... 47
    - 2.4.1. Prediction of power consumption ... 47
      - 2.4.1.1. Experimental considerations ... 47

2.4.1.2. Computational considerations 52

2.4.2. Velocity fields generated in stirred tanks 53

2.4.2.1. Particle Image Velocimetry 53

2.4.2.2. Validation of CFD models using PIV 56

2.4.3. Estimation of mixing time 57

2.4.3.1. Measuring mixing 57

2.4.3.2. Experimental considerations 59

2.4.3.3. CFD as a tool to predict mixing time 61

2.4.3.4. Laminar mixing 62

3. Power analysis 67

3.1. Introduction 67

3.2. Methodology 68

3.2.1. Fluids 68

3.2.1.1. Protocol of rheological measurements 70

3.2.1.2. Rheological results 71

3.2.1.3. Viscoelasticity 73

3.2.2. Experimental setup 77

3.2.2.1. Design 77

3.2.2.2. Experimental protocol 81

3.2.3. CFD Solution 82

3.2.3.1. CFD approach 82

3.2.3.2. Rheology implementation 83

3.2.3.2.1. Power law model 83

3.2.3.2.2. Herschel-Bulkley model 84

3.2.3.3. Grid independence 84

3.3. Results and Discussion 90

3.3.1. Newtonian case 90

3.3.2. Non-Newtonian case 91
    3.3.2.1. Torque predictions 91
    3.3.2.2. Power curves 94
    3.3.2.3. Constant of the impeller 96
    3.3.2.4. Viscosity and velocity profiles 97
3.4. Conclusions 99
4. Flow dynamics in mixing tanks 101
4.1. Introduction 101
4.2. Methodology 102
4.2.1. Scaled-down version of the mixing system 102
4.2.2. Rheology characterization 104
4.2.3. PIV setup 108
4.3. CFD modelling strategy 112
4.3.1. Grid independence 114
4.3.2. Post-processing 116
4.4. Quantification of uncertainty between simulations and experiments 118
4.5. Results and discussion 122
4.5.1. Comparison of computational and experimental results 122
4.5.2. Flow in the vessel 129
4.5.3. Effect of the holes 133
4.5.4. Power consumption 135
4.6. Conclusions 138
5. Mixing time study of highly viscous fluids in stirred tanks 139
5.1. Introduction 139
5.2. Methodology 140
5.2.1. Apparatus 140
5.2.2. Fluids and flow conditions 141

5.2.3. PLIF: setup and image acquisition 141
5.2.4. Experimental mixing time calculations 142
5.3. Computational simulations 145
5.3.1. CFD modelling strategy 146
5.3.1.1. Mixing time 147
5.3.2. Particle tracking 149
5.3.2.1. Additional particle tracking considerations 151
5.3.2.2. Computational mixing time 151
5.4. Results and Discussion 153
5.4.1. Evaluation of mixing time 153
5.4.1.1. Experimental 153
5.4.1.2. CFD 154
5.4.1.3. Particle tracking 155
5.4.1.4. Comparison of methodologies 158
5.4.2. Mixing efficiency 161
5.4.2.1. Poincaré maps 161
5.4.2.2. Stretching fields 165
5.5. Conclusions 171
6. Conclusions 173
6.1. Final remarks 173
6.2. Suggestions for further research 177
References 179
Appendixes 185
Appendix I. Rheology function in a parallel plate 185
Appendix II. Coefficients of the power law model 188
Appendix III. Coefficients of the Herschel Bulkley model 192
Appendix IV. Power curves for all experiments in Chapter 3 197

Appendix V. Eulerian vs Lagrangian stretching 202
  Appendix V.1. Simple two-dimensional shear flow 202
    Appendix V.1.1. Eulerian approach 203
    Appendix V.1.2. Lagrangian approach 204
    Appendix V.1.3. Comparison of the two approaches 205
  Appendix V.2. Simple rotational flow 207

List of Figures

Figure 1. 1. Tooth anatomy (Blausen-Gallery, 2014) 24
Figure 1. 2. GSK turnovers by divisions 25
Figure 1. 3. Zoom in the turnovers of GSK Consumer Healthcare division 25
Figure 1. 4. Pilot plant scale mixer 26
Figure 1. 5. Impeller configuration 27
Figure 2. 1. From left to right, typical axial, mixed, and radial flow patterns. Adapted from Kresta et al. (2015) 32
Figure 2. 2. Common impeller designs. In the first row (axial impellers) from left to right there are represented: hydrofoil impeller, marine propeller and anchor. In the second row (radial impellers) from left to right there are represented: Rushton turbine, concave blade turbine, and double helical ribbon. In the third row (mixed impellers) there is represented: pitched blade turbine 32
Figure 2. 3. Types of generalised Newtonian fluids, adapted from (Chhabra and Richardson, 2011) 36
Figure 2. 4. Schematical representation of the viscosity of two fictitious fluids modelled with the power law and with the Carreau viscosity models. 38
Figure 2. 5. Schematics of a mixing tank equipped with a combination of an air bearing and a load cell to measure power requirement 49
Figure 2. 6. Typical power curve for different impeller geometries (Bates et al., 1963) 50
Figure 2. 7. Schematic representation of particles captured by a camera in four interrogation windows in a hypothetical PIV experiment. Blue and red dots correspond to the first and second images respectively 54
Figure 2. 8. Schematic representation of the correlation function for a 64 by 64 pixel interrogation window 55
Figure 2. 9. Representation of a closed system completely segregated. 57
Figure 2. 10. Examples of cases where a) intensity of segregation and b) scale of segregation can be used to calculate degree of mixing. c) shows a mixing problem where both, intensity of segregation and scale of segregation, can be simultaneously. Adapted from (Paul et al., 2004) 59
Figure 2. 11. Schematics of laminar mixing by consecutive stretching and folding operations, also known as baker's map. N represents periods of the flow. Adapted from (Paul et al., 2004) 63

Figure 2. 12. Schematical representation of the stretching of two infinitesimally close particles 65
Figure 3. 1. Representation of the rheometer (Anton-Paar, 2009) 69
Figure 3. 2. Viscosity profile of samples at different gel mass fractions and temperatures, power law fitting 71
Figure 3. 3. Viscosity profile of samples at different gel mass fractions and temperatures, Herschel-Bulkley fitting 73
Figure 3. 4. Storage (G') and loss (G'') moduli, and phase angle ($\boldsymbol{\delta}$) against the oscillatory shear stress for the 20% gel mixture at 50 ºC 75
Figure 3. 5. Storage (G') and loss (G'') moduli, and phase angle ($\boldsymbol{\delta}$) against the oscillatory shear stress for the 100% gel mixture at 50 ºC 75
Figure 3. 6. Standard ratios of a baffled tank and Rushton turbine (Rushton et al., 1950) 78
Figure 3. 7. Mixing tank, air bearing, and Rushton turbine 79
Figure 3. 8. Load cell and data acquisition system 80
Figure 3. 9. Experimental setup 80
Figure 3. 10. Mesh used in the numerical simulations 88
Figure 3. 11. Experimental, computational, and bibliographical power curves for Newtonian fluids agitated in an unbaffled tank equipped with a Rushton turbine for geometrically similar systems 90
Figure 3. 12. Torque vs impeller speed for 80% gel at 60 ºC 92
Figure 3. 13. Torque vs Impeller speed for 40% gel at 40 ºC 92
Figure 3. 14. Power curve for 80% gel mass fraction and 60 ºC 95
Figure 3. 15. Power curve for 40% gel mass fraction and 40 ºC 95
Figure 3. 16. Viscosity contours and velocity vectors for a) glycerol at 20 ºC, b) 80% gel at 60ºC, and c) 40% gel at 40ºC at 100 rpm 98
Figure 3. 17. Viscosity contours and velocity vectors for a) glycerol at 20 ºC, b) 80% gel at 60ºC, and c) 40% gel at 40ºC at 500 rpm 98
Figure 4. 1. Representation of the pilot plant scale mixer 102
Figure 4. 2. Schematic and dimensions of the tank, impeller, baffles, and liquid height 104
Figure 4. 3. Viscosity and shear stress as a function of the shear rate for the 5% gel mixture 105
Figure 4. 4. Viscosity and shear stress as a function of the shear rate for the 20% gel mixture 106
Figure 4. 5. Sketch of the main components of the experimental set-up for the PIV measurements 109

Figure 4. 6. Experimental profiles of the y- and z- velocity components (V and W respectively) with error bars along the Z-direction for Y = -0.053 m, and X = 0 m, for 5% gel and 40 rpm 111
Figure 4. 7. Schematics of the moving (yellow) and stationary (blue) zones. The final grid can also be seen. 113
Figure 4. 8. Profiles of the y- and z- velocity components (V and W respectively) along the positive Y direction at X = 0 at two different heights: a) and b) Z = 3cm, and c) and d) Z = 8 cm........ 115
Figure 4. 9. Transformation of velocity results from the CFD to the PIV grid - Velocities from the CFD simulations 116
Figure 4. 10. Transformation of velocity results from the CFD to the PIV grid - Velocities translated into the PIV grid 117
Figure 4. 11. Nominal case and position of impeller on PIV images (clockwise impeller rotation)........ 118
Figure 4. 12. Top view of the mixing tank and the effect of uncertainty in laser alignment119
Figure 4. 13. Scenarios of mispositioning the sensor with clockwise impeller rotation...... 120
Figure 4. 14. PIV vs CFD velocity profiles on the plane X = 0 using the y- and z- velocity components for 5% gel and 40rpm 123
Figure 4. 15. Velocity profiles of V [a) and c)] and W [b) and d)] at two different Y positions [6 cm in a) and b), and 3 cm in c) and d)] for 5% gel and 40rpm........ 125
Figure 4. 16. PIV vs CFD velocity profiles on the plane X = 0 using the y- and z- velocity components for 20% gel and 140 rpm 126
Figure 4. 17. Velocity profiles of V [a) and c)] and W [b) and d)] at two different Y positions [4.4 cm in a) and b), and 2.3 cm in c) and d)] for 20% gel and 140 rpm........ 127
Figure 4. 18. PIV vs CFD velocity profiles on the plane X = 0 using the y- and z- velocity components for 5% gel and 120rpm 128
Figure 4. 19. PIV vs CFD velocity profiles on the plane X = 0 using the y- and z- velocity components for 20% gel and 80 rpm 129
Figure 4. 20. Velocity streamlines for 5% gel and 40 rpm 130
Figure 4. 21. Velocity streamlines for 20% gel and 140 rpm 131
Figure 4. 22. Isosurfaces of velocities as fractions of the tip speed, a) 10%, b) 30%, c) 50%, and d) 70%........ 132
Figure 4. 23. Volume fraction of total fluid moving at different fractions of relative tip speed and cumulative volume fraction of fluid moving at velocities below $\mathbf{U/Vtip}$. The phase angle of the impeller is the same as in Figure 4.22 133

Figure 4. 24. a) Shear rate profiles on the top right blade a) 5% gel and 40 rpm, b) 20% gel and 140 rpm 134
Figure 4. 25. Shear rate profiles in the impeller and the baffles a) 5% gel and 40 rpm, b) 20% gel and 140 rpm 135
Figure 4. 26. Power curves of the mixing system with the two mixtures (20% and 5%wt gel) and with glycerol........ 136
Figure 5. 1. Calibration curve 144
Figure 5. 2. Example of six isovolumetric elements of a cylinder........ 148
Figure 5. 3. Location of particle P, and the four closest nodes from the CFD grid (A, B, C, and D) 150
Figure 5. 4. Concentration profiles for case 2 shown in Table 5. 1 at a) 10, b) 25, and c) 40 seconds for the mixing experiments........ 153
Figure 5. 5. Concentration profiles for case 2 shown in Table 5. 1 at a) 10, b) 25, and c) 40 seconds for the CFD simulations with the transport of species equation........ 155
Figure 5. 6. Concentration profiles for case 2 shown in Table 5. 1 at a) 10, b) 25, and c) 40 seconds for the particle tracking approach........ 156
Figure 5. 7. Number of particles in the 3D discretised elements as a function of time for case 2 shown in Table 5. 1 157
Figure 5. 8. Normalised standard deviation of the concentration profiles for all four cases presented in Table 5. 1 159
Figure 5. 9. Poincaré maps of the four cases shown in Table 5. 1 163
Figure 5. 10. Stretching maps after 200 periods for all four cases shown in Table 5. 1 168
Figure 5. 11. evolution of $\boldsymbol{\lambda}$ as function of the time periods........ 170
Figure APIV. 1. Power curve for 20% gel mass fraction and 40 ºC 197
Figure APIV. 2. Power curve for 20% gel mass fraction and 60 ºC 197
Figure APIV. 3. Power curve for 40% gel mass fraction and 40 ºC 198
Figure APIV. 4. Power curve for 40% gel mass fraction and 60 ºC 198
Figure APIV. 5. Power curve for 60% gel mass fraction and 40 ºC 199
Figure APIV. 6. Power curve for 60% gel mass fraction and 60 ºC 199
Figure APIV. 7. Power curve for 80% gel mass fraction and 40 ºC 200
Figure APIV. 8. Power curve for 80% gel mass fraction and 60 ºC 200
Figure APIV. 9. Power curve for 100% gel mass fraction and 40 ºC 201
Figure APIV. 10. Power curve for 100% gel mass fraction and 60 ºC 201
Figure APV. 1. Velocity profile of a simple shear flow produced by two parallel plates where the top one moves at v_t and the bottom one is stationary. A flow element is represented in light blue for the Eulerian perspective. Additionally, two particles are introduced in the flow, one on each extreme of the flow element for the Lagrangian study. 202

Figure APV. 2. Stretching of the fluid using both the Eulerian (Explicit) and the Lagrangian approaches........ 205

Figure APV. 3. Position of the two particles against time........ 206

Figure APV. 4. Velocity profile of a simple rotational flow produced by a circle rotating at a constant angular speed ω. A flow element is represented in light blue for the Eulerian perspective. Additionally, two particles are introduced in the flow, one on each extreme of the flow element for the Lagrangian study........ 207

Figure APV. 5. Stretching of the fluid using both the Eulerian (Explicit) and the Lagrangian approaches........ 210

Figure APV. 6. Position of the two particles against time........ 211

List of Tables

Table 3. 1. Coefficients of the power law model for different gel mass fractions and temperatures 72

Table 3. 2. Magnitudes of shear stress and shear rate at which the phase angle is 45 º 76

Table 3. 3. Typical values for ratios of the dimensions of a baffled tank and a Rushton turbine (Rushton et al., 1950) 78

Table 3. 4. Dimensions of the tank and Rushton turbine to use in the experiments in centimetres 78

Table 3. 5. Comparison among the three mesh qualities studied for the different modelling approaches using the geometry in Figure 3. 9, with glycerol at 27 ºC as working fluid and an impeller speed of 100 rpm 85

Table 3. 6. Comparison among the three mesh qualities studied for the different modelling approaches using the geometry in Figure 3. 9, with pure gel at 85 ºC as working fluid and an impeller speed of 1000 rpm 86

Table 3. 7. Comparison between the torques computed on the surface of the impeller and on the walls of the tank for the RF calculations using the geometry in Figure 3. 9, with glycerol at 27 ºC as working fluid and an impeller speed of 100 rpm 87

Table 3. 8. Comparison between the torques computed on the surface of the impeller and on the walls of the tank for the RF calculations using the geometry in Figure 3. 9, with pure gel at 85 ºC as working fluid and an impeller speed of 1000 rpm 87

Table 3. 9. $\boldsymbol{Ks}$ values for all the non-Newtonian power curves 96

Table 4. 1. Parameters of the Carreau model and average error in the fitting for the 5% gel mixture 107

Table 4. 2. Parameters of the Carreau model and average error in the fitting for the 20% gel mixture 107

Table 4. 3. Summary of the meshes studied, number of cells and simulation time per mesh size 114

Table 4. 4. List of experimental conditions 122

Table 5. 1. Flow conditions and the corresponding properties of the fluids of the mixing studies 141

Table 5. 2. Experimental and computational mixing times 160

Table APII. 1. Values of K [kg $s^{(n-2)}$ m^{-1}] for different temperatures and gel mass fractions 189

Table APII. 2. Values of n for different temperatures and gel mass fractions 190

Table APII. 3. Averaged percentage errors in the estimation of the *K* and *n* coefficients to be used in the power law model 191

Table APIII. 1. Values of $\boldsymbol{\tau 0}$ [Pa] for different temperatures and gel mass fractions for the Herschel-Bulkley model 193

Table APIII. 2. Values of *K* [kg $s(n^{-2})$ m^{-1}] for different temperatures and gel mass fractions for the Herschel-Bulkley model 194

Table APIII. 3. Values of *n* for different temperatures and gel mass fractions for the Herschel-Bulkley model 195

Table APIII. 4. Errors in the Herschel-Bulkley model 196

1. Introduction

1.1. Background

Toothpaste is the most common dentifrice in the world used every day by millions of people. It is used to protect the teeth against bacteria, to prevent tooth decay, to remove the plaque and for aesthetic purposes. Ancient civilisations used oral health products for the same ends, and the oldest manuscript found as a proof is the Ebers Papyrus, an Egyptian manual written about the 1500 B.C.E., which compiled works dating to 4000 B.C.E. that contain a recipe for compounding tooth-cleaning preparations (Fischman, 1992). It was not until the late 19th century that the first modern toothpastes appeared in Europe after W. D. Miller described his chemoparasitic theory of tooth decay (Fischman, 1997). Modern toothpastes are made in their greatest percentage of water and insoluble abrasive substances such as calcium salts, or silicas, which help to remove plaque from teeth. Additionally, they often contain other chemicals such as fluorides, flavourings, colourings, humectants, surfactants, and rheology modifiers, mainly to obtain certain desired properties to comply with either clinical or marketing purposes (Harman, 2001).

Teeth hypersensitivity is a generalised pathology that affects adults worldwide, affecting 3.8 - 57% of the population according to different studies (Hench, 2006, Rees and Addy, 2002, Rees, 2000, Irwin and McCusker, 1997). This occurs when the dentin becomes exposed and is no longer protected by the enamel (see Figure 1. 1 for tooth anatomy (Blausen-Gallery, 2014)).

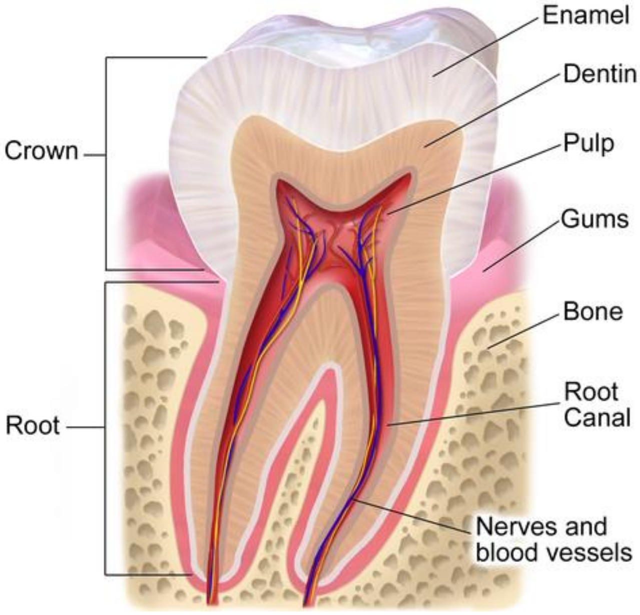

Figure 1. 1. Tooth anatomy (Blausen-Gallery, 2014)

The dentin has small openings or tubules that communicate with the pulp chamber. If the dentinal tubules become exposed, hot or cold may be transmitted to the nerves in the pulp, which causes pain. Prof. Larry Hench created in 1969 the Bioactive glass, a material compatible with the human body and commonly used in implants to repair or replace human bones. This material is formed of calcium, sodium, silica and phosphorus, and precipitates under aqueous conditions as hydroxycarbonate apatite, forming a layer that occludes the tubules in the teeth and prevents hypersensitivity (Hench, 2006). Bioactive glass can be included in toothpastes to prevent hypersensitivity, although this implies that an organic solvent needs to substitute water in the toothpaste formulation. This is precisely the case of the non-aqueous products that GlaxoSmithKline Consumer Healthcare developed under the Sensodyne® brand.

1.2. Motivation

GlaxoSmithKline Consumer Healthcare division accounted for almost a fifth of the total turnover of the company, with more than £4.3bn in 2014 (Figure 1. 2). Oral health was the greatest contributor to that success for the Consumer Healthcare division, carrying the 41% of the total sales of the different categories (£1.8M, Figure 1. 3); this is 4% more than that of the previous year. This increase was primarily driven by the 11% sales growth in the Sensodyne® brand (GSK, 2015).

Nevertheless, Sensodyne® is one of the newest brands in GSK, and there is room for increasing process understanding and process optimisation, which are targeted by the quality-by-design policies of the company. Amongst others, a powerful tool that can be used in this case to acquire relevant process and product information is computational fluid dynamics (CFD), which can be used to assess product homogeneity or to identify deficiencies in the process design and operating conditions.

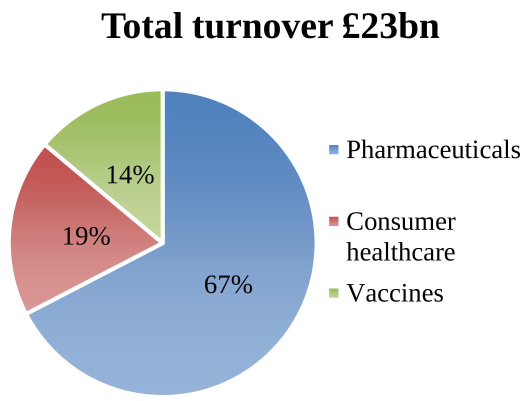

Figure 1. 2. GSK turnovers by divisions

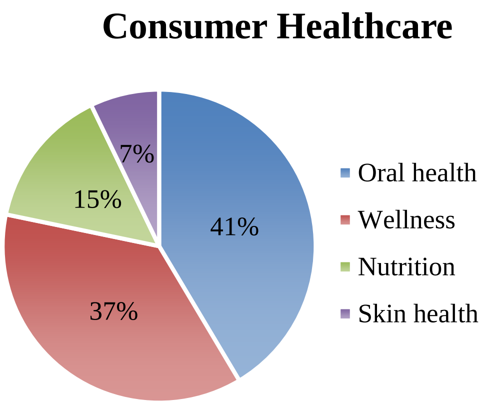

Figure 1. 3. Zoom in the turnovers of GSK Consumer Healthcare division

1.3. Objectives

The main objective of this research is to provide insight into the mixing process of glycerol with a gel made of carbomer and polyethylene glycol, which is a critical step in the manufacturing of non-aqueous toothpastes by GlaxoSmithKline Consumer Healthcare. Mixing these two materials is slow and energy intensive, and the properties of the final toothpaste are dramatically affected by the homogeneity of the product at the end of this processing stage. A picture of the pilot-scale mixer is shown in Figure 1. 4. Computational fluid dynamics (CFD) is identified as a powerful tool for flow diagnostics, and experimental work is needed to validate the CFD models. A fully validated CFD model of the real process would help in the identification of high shearing zones that can damage the product, the identification of stagnant zones where no effective mixing happens, the assessment of the homogeneity of the product, and the potential use of the model to explore different experimental conditions to optimise the production process.

Figure 1. 4. Pilot plant scale mixer

1.4. Description of the system to study

The process of interest is the mixing of glycerol with a gel, which is a mixture of Polyethylene glycol and carbomer. The carbomer molecule used in this study is not disclosed for confidentiality reasons, and the term “carbomer gel” will be used to refer to the gel. The mixing process occurs in a stirred tank with two coaxial counter-rotating impellers (Figure 1. 4 and Figure 1. 5).

Figure 1. 5. Impeller configuration

This is a jacketed tank and both cooling and heating are possible. In addition, the vessel is equipped with a vacuum system, a window that can be used to look the inside, a recycle line and a lateral inlet. There are two temperature probes, one at the bottom of the tank and the other in the recycle line. Additionally, there is a pressure sensor at the top of the tank, and the power of each impeller can be measured with two independent power indicators. The mixing of the aforementioned substances happens at a medium-low height level of the fluid in the tank. The tank is filled with glycerol (ideally at 60 ºC) first, and the gel is added gradually from the bottom of the tank. The gel addition time is approximately 10 minutes, and the mixing operation is carried out for more than 40 minutes.

1.5. Structure

This thesis contains six chapters. In Chapter 1, the research topic is introduced and the relevance of this project is highlighted. In Chapter 2, the general background necessary to understand complex fluid behaviour in mechanically agitated tanks is presented first. Then, generalities of CFD modelling are summarised, which are followed by a review of the different pieces of information that CFD can be used to obtain with the corresponding experimental techniques used to validate CFD models.

Chapters 3 to 5 are self-contained sections with individual methodology, results and conclusion subsections. Each chapter corresponds to individual milestones to obtain essential information for the modelling of the real system.

In Chapter 3, it is aimed to implement a CFD model of a simple stirred tank to model the flow behaviour of different mixtures of glycerol and the carbomer gel. First, the rheological properties of the mixtures of these two fluids are comprehensively studied to provide the CFD model with an adequate constitutive equation for the viscosity. Then, the CFD model is implemented and validated against accurate experimental results of power consumption obtained in a stirred vessel equipped with a frictionless air bearing and a load cell and with bibliographical data.

In Chapter 4, a simplified scaled down version of a pilot plant mixer is developed, keeping geometric similarity. A CFD model of the laboratory-scale mixing tank is implemented to study the fluid dynamics. The impeller performance is assessed qualitatively by plotting the velocity streamlines and the isosurfaces of velocity. The performance of the impeller is also studied quantitatively by calculating the percentage of the fluid that has speeds above given thresholds. The computational results are validated using the particle image velocimetry (PIV) technique.

In Chapter 5, the planar laser induced fluorescence (PLIF) technique is used to investigate the mixing time in glycerol and in glycerol (80% wt.)/carbomer gel (20% wt.) solutions, using a fluorescent tracer in the laboratory-scale mixer described in Chapter 4. The potential of CFD as a predictive tool for estimating mixing time is assessed for the two aforementioned solutions. An alternative method to estimate mixing time using a Lagrangian particle tracking approach is also presented. Finally, the performance of the mixer is assessed in terms of Poincaré maps and stretching fields.

In Chapter 6, the main findings of this research are highlighted, and steps for further investigation are presented.

2. Literature review

2.1. Stirred tanks

Mixing processes are core in industrial applications. Typical industrial mixing problems involve blending miscible liquids, suspending solids in liquids, dispersing gases in liquids, and creation of emulsions among others. There is not a piece of equipment capable of performing efficiently all the aforementioned tasks. Instead, engineers have developed different apparatuses for those specific applications, such as stirred tanks, in-line static mixers, or jet mixers (Nienow et al., 1997). Among those, stirred tanks are the most common piece of equipment used in industry to blend miscible fluids, which is of particular interest for this research. The terms mixing tank, mechanically agitated tank and stirred tank are used interchangably.

Stirred tanks are vessels that contain one or more mechanical stirrers. Although they are conceptually very simple, their design can be complex and commonly based on experience. The geometric configuration of both impeller and tank, together with the fluid physical properties, in particular viscosity, dramatically affect the fluid dynamics of the system. Any rotating impeller in a mixing tank creates a flow in the angular direction, and additionally, a characteristic flow pattern that can be axial, radial or mixed. Exhaustive experimental work was conducted in the second half of the last century to determine the flow patterns generated by standard impeller designs (Metzner and Taylor, 1960, Nienow and Miles, 1978, Yianneskis et al., 1987, Kresta and Wood, 1993, Jaworski et al., 1996). The three typical flow patterns can be schematically represented as in Figure 2. 1. Examples of typical radial, axial, and mixed impellers can be found in Figure 2. 2.

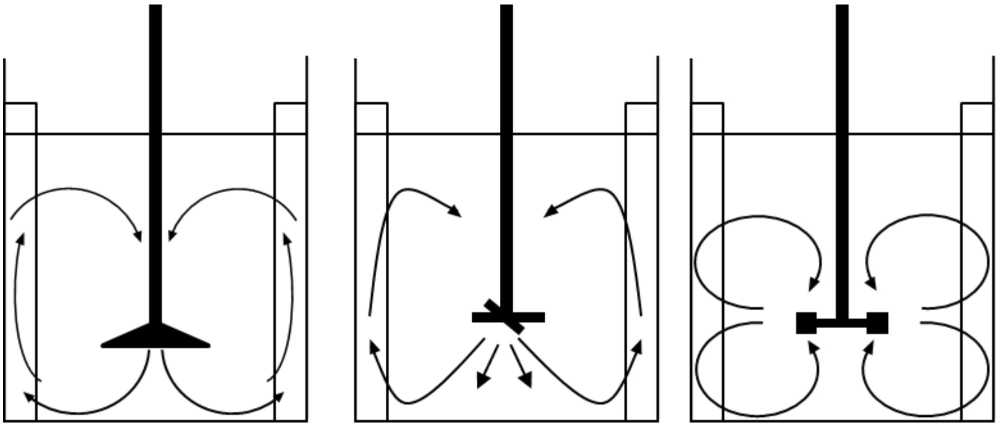

Figure 2. 1. From left to right, typical axial, mixed, and radial flow patterns. Adapted from Kresta et al. (2015)

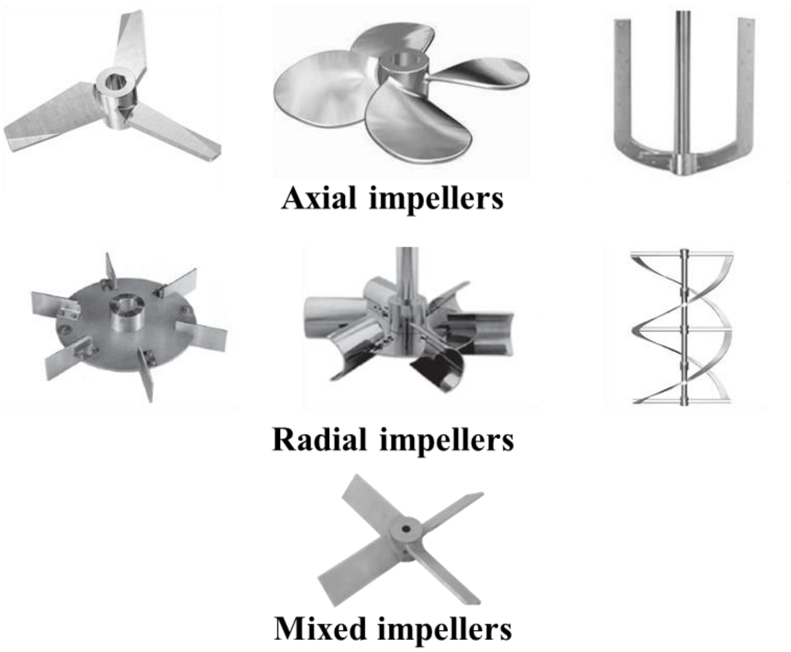

Figure 2. 2. Common impeller designs. In the first row (axial impellers) from left to right there are represented: hydrofoil impeller, marine propeller and anchor. In the second row (radial impellers) from left to right there are represented: Rushton turbine, concave blade turbine, and double helical ribbon. In the third row (mixed impellers) there is represented: pitched blade turbine

Guidelines for adequate mixer designs according to mixing application, volume to be mixed and fluid viscosity are readily available in the literature (Paul et al., 2004, Zlokarnik, 2003, Nienow et al., 1997). These guidelines are generally limited for mixing Newtonian fluids in the turbulent regime. Although non-Newtonian fluids are employed in many industrial processes, far less information is available about optimal mixer designs to deal with them. These fluids are complex to mix, and sophisticated designs which include multiple impellers inside the tank are often required (Kresta et al., 2015, Chhabra and Richardson, 2011). Moreover, complex fluids can also be sensitive to high shearing conditions or to temperature, which prohibits the operation in the turbulent regime and makes the optimal design of impellers even more critical. This is precisely the case in the oral health industry, where highly viscous non-Newtonian fluids are used in the production of non-aqueous toothpastes.

2.2. Fluid rheology

Fluid rheology is an overwhelmingly extensive topic. Entire books devoted to analysing every single aspect of fluid rheology have been written in the past. In this research, incompressible generalised Newtonian fluids are of interest. Hence, I focus on the relevant literature covering this type of fluids, and relevant concepts of the remaining disciplines of fluid rheology are also introduced.

Fluids can be approximated as continuum when the scale of the phenomena studied is of orders of magnitude greater than molecules (hypothetical infinitely divisible substance that can be treated by macroscopic methods). When the continuum hypothesis is applicable, fluid properties are assumed to have definite values on every point in space, and that those values are continuous functions of position and time (Papanastasiou et al., 2000). Viscosity is one of such properties.

Incompressible fluids can be classified according to the effects produced under the action of shear stress. The simplest fluids one can find are those that obey Newton's viscosity law:

$$\boldsymbol{\tau} = -2\mu \boldsymbol{D} \qquad \text{(Eq. 2.1)}$$

Where $\boldsymbol{\tau}$ is the viscous (or deviatoric) stress tensor, μ is the Newtonian viscosity (which is a constant at a given temperature for Newtonian fluids), and $\boldsymbol{D}$ is the rate of strain tensor, which is the symmetric part of the velocity gradient tensor ($\nabla\mathbf{v}$):

$$\nabla\mathbf{v} = \boldsymbol{D} + \boldsymbol{\Omega} = \frac{1}{2}[(\nabla\mathbf{v}) + (\nabla\mathbf{v})^T] + \frac{1}{2}[(\nabla\mathbf{v}) - (\nabla\mathbf{v})^T] \qquad \text{(Eq. 2.2)}$$

In equation 2.2, $\boldsymbol{\Omega}$ is the vorticity tensor.

Equation 2.1 can be rewritten as:

$$\boldsymbol{\tau} = -\,\mu\dot{\boldsymbol{\gamma}} \quad \text{with} \quad \dot{\boldsymbol{\gamma}} \equiv [(\nabla\mathbf{v}) + (\nabla\mathbf{v})^T] \qquad \text{(Eq. 2.3)}$$

where $\dot{\boldsymbol{\gamma}}$ is twice the rate of strain tensor. It is also convenient to define the magnitude of the tensors $\boldsymbol{\tau}$ and $\dot{\boldsymbol{\gamma}}$ (the latter commonly referred to as shear rate):

$$\tau \equiv \sqrt{\frac{1}{2}\,(\boldsymbol{\tau}\colon\boldsymbol{\tau})} \qquad \text{(Eq. 2.4)}$$

$$\dot{\gamma} \equiv \sqrt{\frac{1}{2}\,(\dot{\boldsymbol{\gamma}}\colon\dot{\boldsymbol{\gamma}})} \qquad \text{(Eq. 2.5)}$$

Non-Newtonian fluids are those that deviate from Newton's law of viscosity in any form. Non-Newtonian fluids are ubiquitous in industrial applications and in everyday life. Foodstuffs such as ketchup or mayonnaise, cosmetics, healthcare products, such as toothpaste, paints, and blood, are all examples of non-Newtonian fluids. Generally, they can be classified into three non-exclusive groups:

(1) Generalised Newtonian fluids are the simplest type of non-Newtonian fluids. For them, Eq. 2.3 still holds, but the viscosity of these fluids depends (only) on the local, instantaneous shear rate. A schematic of these types of fluids can be found in Figure 2. 3.

(2) Time-dependent fluids are those whose viscosity changes upon duration of shearing and their kinematic history.

(3) Visco-elastic fluids are those that exhibit both elastic and viscous behaviour.

Groups (1) and (3) are of particular interest for this thesis.

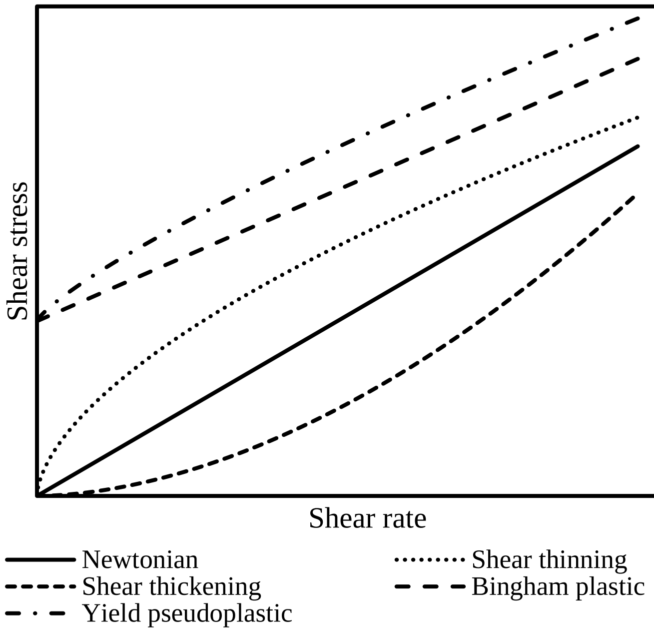

Figure 2. 3. Types of generalised Newtonian fluids, adapted from (Chhabra and Richardson, 2011)

2.2.1. Generalised Newtonian fluids

Full rheological characterisation of fluids requires the exploration of steady and non-steady fluid response under shearing conditions, and exploration of viscoelastic properties. Such a thorough investigation is often of interest to mathematicians and physicists (Bird, 2002). Complex rheological models are often impractical to use, and often, simplified models are able to capture the major rheological properties of fluids with great success. These are the models that engineers tend to use (Bird, 2002). Generalised Newtonian fluid models are the simplest from the above. The relationship between shear rate and viscous stress tensors is as follows:

$$\boldsymbol{\tau} = -\,\eta\dot{\boldsymbol{\gamma}} \qquad \text{(Eq. 2.6)}$$

where η is the non-Newtonian viscosity, which is a function of the shear rate magnitude for a specific temperature. A number of empirical correlations can be found in the literature to model the relationship in Eq. 2.6. For fluids that do not have a yield stress, the most common correlation is the power law (Eq. 2.7):

$$\eta = K\,\dot{\gamma}^{n-1} \begin{cases} \text{if } n < 1, \text{shear thinning fluids} \\ \text{if } n = 1, \text{Newtonian fluids} \\ \text{if } n > 1, \text{shear thickening fluids} \end{cases} \qquad \text{(Eq. 2.7)}$$

where K and n are characteristic constants of the fluid known as the consistency index and the flow behaviour index respectively.

Newtonian, shear thinning and shear thickening fluids are particular cases of the power law model as shown in Eq. 2.7. Despite the simplicity of the power law model, it has been proved to be adequate for a large number of fluids and it is often used in industrial applications (Chhabra and Richardson, 2011). Another constitutive equation for the non-Newtonian viscosity that is widely used is the Carreau viscosity model (Eq. 2.8), which includes the values of viscosity at virtual 0 and ∞ shear rates, and suitable for fluids whose viscosity plateaus at low and high values of shear rate.

$$\eta = \mu_\infty + (\mu_0 - \mu_\infty)[1 + (\lambda\,\dot{\gamma})^2]^{\frac{n-1}{2}} \qquad \text{(Eq. 2.8)}$$

In Equation 2.8, μ_∞ and μ_0 are the values of the fluid viscosity at infinite and zero shear rates respectively, and λ and n are characteristic constants of the fluid.

Comparison of the power law and the Carreau models for two hypothetical fluids can be found in Figure 2. 4.

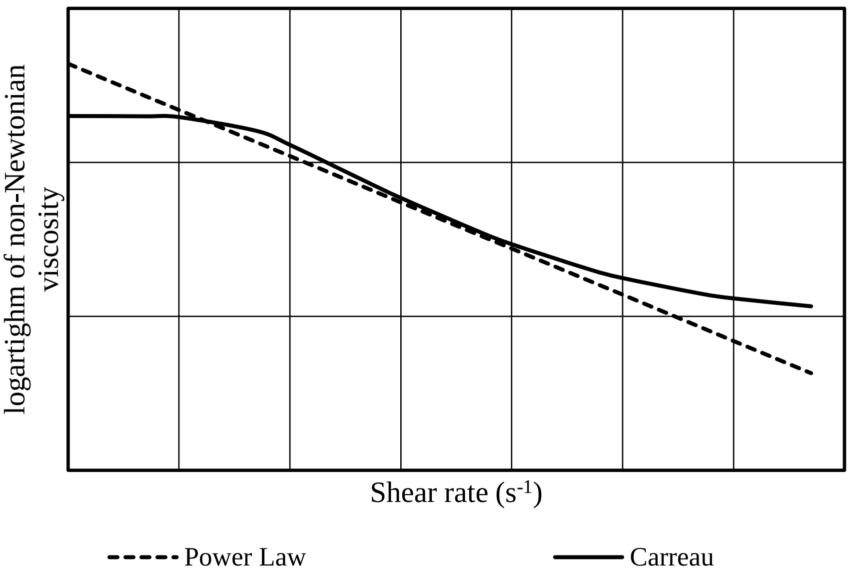

Figure 2. 4. Schematical representation of the viscosity of two fictitious fluids modelled with the power law and with the Carreau viscosity models.

Viscoplastic fluids are those characterised by the existence of a yield stress (τ_0) that needs to be exceeded before the fluid starts to flow. These fluids behave as elastic solids before the yield stress threshold is surpassed. After that, they start flowing as liquids, and their viscosity can either be constant (Bingham fluids) or vary as a function of the shear rate (Yield pseudoplastic fluids) (Chhabra and Richardson, 2011). The rheological model that is commonly used for these types of fluids is the Herschel-Bulkley model:

$$\eta = \begin{cases} \infty, & \tau \leq \tau_0 \\ \dfrac{\tau_0}{\dot{\gamma}} + K\dot{\gamma}^{(n-1)}\,, & \tau \geq \tau_0 \end{cases} \qquad \text{(Eq. 2.9)}$$

where τ_0 is the yield stress, and K and n coefficients have equivalent definitions as in the power law model. It is important to note that in Eq. 2.9 the magnitude of shear stress is used, so the yield stress is a scalar.

2.2.2. Viscoelastic fluid behaviour

Viscoelastic fluids are common in industrial applications such as the healthcare or the foodstuff industries; two examples are gels and pastes. These fluids present both viscous deformation as the generalised Newtonian fluids and elastic deformation. This means that a part of the stress applied to the fluid is stored as energy, which may cause a partial recovery of the original structure when the stress is removed (Macosko, 1994).

In the two extremes, the fluid behaves as an elastic (Hookean) solid (Eq. 2.10) and as a viscous fluid (Eq. 2.11):

$$\tau = G\gamma \qquad \text{(Eq. 2.10)}$$

$$\tau = \eta\dot{\gamma} \qquad \text{(Eq. 2.11)}$$

In Equations 2.10 and 2.11, the moduli of the deviatoric stress (τ), strain (γ), and shear rate $(\dot{\gamma})$ tensors are used. For this entire subsection, the following notation of the stress tensor is adopted (Bird, 2002), where p is the pressure and $\boldsymbol{I}$ is the identity tensor:

$$\boldsymbol{\pi} = \boldsymbol{\tau} + p\boldsymbol{I} \qquad \text{with } \begin{array}{c} \tau_{i,j} = \tau_{j,i} \text{ when } i \neq j \\ \tau_{i,j} = 0 \text{ when } i = j \end{array} \qquad \text{(Eq. 2.12)}$$

The viscoelastic material response to a stress depends both, on the specific structure of the material and on the conditions to which it has been subjected to. Within the range of the linear viscoelasticity, the effects of consecutive changes in strain are additive, and the instantaneous relation of the stress to the strain is independent from the stress magnitude. The stress and the resulting strain are connected by a constitutive equation from the Boltzmann superposition principle (Chhabra and Richardson, 2011):

$$\tau_{i,j}(t) = \int_{-\infty}^{t} G(t-t')\dot{\gamma}_{i,j}(t')dt' \qquad \text{with } i \neq j \qquad \text{(Eq. 2.13)}$$

where $G(t)$ is the stress relaxation modulus, and the integration is performed over all past times t' up to the current time (t).

If a periodic stress is applied with a given frequency to a viscoelastic material, the corresponding strain will also vary periodically at the same frequency but out of phase (and vice versa). Applying the following periodic deformation (Chhabra and Richardson, 2011):

$$\gamma = \gamma_m \sin(\omega t) \qquad \text{(Eq. 2.14)}$$

where γ_m is the amplitude and ω is the frequency.

The corresponding strain rate is:

$$\dot{\gamma} = \gamma_m \omega \cos(\omega t) \qquad \text{(Eq. 2.15)}$$

Substituting Eq. 2.15 in Eq. 2. 13, and replacing $(t-t')$ by s:

$$\tau_{i,j}(t) = \int_{0}^{\infty} G(s)\gamma_m \omega \cos[\omega(t-s)]\, ds = \gamma_m[G' \sin(\omega t) + G'' \cos(\omega t)] \qquad \text{(Eq. 2.16)}$$

where:

$$G' = \omega \int_{0}^{\infty} G(s) \sin(\omega s)\, ds \qquad \text{(Eq. 2.17)}$$

$$G'' = \omega \int_{0}^{\infty} G(s) \cos(\omega s)\, ds \qquad \text{(Eq. 2.18)}$$

G' and G'' are storage (or elastic) and the loss (or viscous) modulus respectively. These two terms are not function of time. Eq. 2.16 can be rearranged as:

$$\tau_{i,j}(t) = \tau_m \sin(\omega t + \delta) \tag{Eq. 2.19}$$

with:

$$G' = \frac{\tau_m}{\gamma_m} \cos(\delta) \tag{Eq. 2.20}$$

$$G'' = \frac{\tau_m}{\gamma_m} \sin(\delta) \tag{Eq. 2.21}$$

$$\frac{G''}{G'} = \tan(\delta) \tag{Eq. 2.22}$$

$$\sin(\omega t + \delta) = \cos(\delta)\sin(\omega t) + \sin(\delta)\cos(\omega t) \tag{Eq. 2.23}$$

Clearly, if the fluid behaves as an elastic solid, $\delta = 0$, and if it behaves as a viscous liquid, $\delta = \pi/2$.

2.3. Computational Fluid Dynamics

2.3.1. Generalities

Computational fluid dynamics (CFD) is the study of fluid flow by means of computer-based simulations. This is a powerful tool that can be used to model the dynamics of almost all types of fluids in almost any type of geometry provided that the physics of the system and the fluid properties are well characterised. Commercial CFD codes are composed of three main elements: pre-processor, solver, and post-processor (Versteeg and Malalasekera, 2007).

The pre-processing part is the most user intensive of the three. It involves the description of the problem. This includes the definition of the geometry and its discretisation in a grid, the definition of the fluid properties, the physical and chemical description of the system, and the specification of the boundary conditions (Versteeg and Malalasekera, 2007).

The selection of an adequate solver is as important as the pre-processing step. CFD users are seldom going to develop new solvers for their application; instead, they most likely will use one of the commercial ones. As per the current state of technology, CFD codes based on the Finite Volume Method (FVM) are by far the most used in research and industry because they provide the fastest convergence compared to others, and they are capable of dealing with complex geometrical systems. For these reasons, the commercial CFD package used in this research is based in FVM.

Information on other types of streams of numerical solution techniques can be found elsewhere (Anderson and Wendt, 1995). CFD codes have embedded different solver strategies, which control the way that the governing equations are discretised, and the way the algebraic equations are solved by iterative processes (Versteeg and Malalasekera, 2007).

The post-processing part involves the graphical representation of the variables of interest, normally velocity, pressure, or concentration, in a practical and appealing manner.

2.3.2. Basic equations of fluid flow

Equations of fluid flow are derived by physics, and they hold regardless of the CFD package used. As aforementioned, commercial CFD codes differ mainly in the way they discretise and integrate these equations. The main equation to model fluid flow is the linear momentum balance:

$$\frac{\partial}{\partial t}(\rho \mathbf{v}) = -\nabla \cdot (\rho \mathbf{v}\mathbf{v}) - \nabla p - \nabla \cdot \boldsymbol{\tau} + \rho \mathbf{g} \qquad \text{(Eq. 2.24)}$$

where $\frac{\partial}{\partial t}(\rho \mathbf{v})$ is the rate of increase of momentum per unit volume, $-\nabla \cdot (\rho \mathbf{v}\mathbf{v})$ is the rate of momentum addition by convection per unit volume, $-\nabla p - \nabla \cdot \boldsymbol{\tau}$ is the rate of momentum addition by molecular transport per unit volume, and $\rho \mathbf{g}$ is the external force on the fluid per unit volume (Bird, 2002).

The linear momentum balance always needs to be coupled with the equation of mass conservation:

$$\frac{\partial \rho}{\partial t} = -\nabla \cdot (\rho \mathbf{v}) \qquad \text{(Eq. 2.25)}$$

where $\frac{\partial \rho}{\partial t}$ is the rate of increase of mass per unit volume, and $-\nabla \cdot (\rho \mathbf{v})$ is the rate of mass addition per unit volume by convection. For incompressible flows, mass per unit volume cannot increase, and hence $\nabla \cdot \mathbf{v} = 0$ (Bird, 2002).

The model can be tailored to replicate the reality as much as possible by adding extra information such as turbulence models, single phase multicomponent flow, multiphase multicomponent flow, chemical reaction, or heat transfer among others. Additionally, the physical properties of the fluids involved in the study and the boundary conditions of the system need to be specified.

2.3.3. Rotating boundaries in CFD

Of particular interest to this research is the study of fluid behaviour in rotational motion about an axis. Most systems that involve rotating boundaries are unsteady by nature, although with a careful choice of the reference frame, the flow can be treated as steady. CFD software have the option to treat rotating systems as steady state problems by using reference frames of rotation, which consider fictitious centrifugal and Coriolis forces. This approach has the capability of obtaining relevant information of the system at very low computational and time costs. However, there are some restrictions e.g. (i) in cases where the angular velocity varies in time or (ii) under the presence of strong unsteady interaction between stationary and moving parts.

In ANSYS Fluent there are four models to deal with rotating boundaries: (1) Single Reference Frame (SRF), (2) Multiple Reference Frame (MRF), (3) Mixing Plane Model (MPM), and Sliding Mesh (SM). The first three can be used to model steady state flows; the Sliding Mesh is the only one that considers a time dependent solution.

The SRF model can only be used when the whole domain of simulation is in the rotating reference frame. An illustrative example of the applicability of the SRF is in an unbaffled tank. In this example, if the observer sits on the tip of the impeller spinning at a rotational speed $\boldsymbol{\omega}$, he will see the impeller as a steady object and the walls of the impeller as moving objects with a velocity $-\boldsymbol{\omega}$. However, the introduction of baffles in the tank, or any other non-axisymmetric body will make the SRF non-applicable.

The MRF can be used to provide a steady-state approximation for systems with multiple rotating and non-rotating boundaries. It is necessary to split the entire domain into subdomains connected by interfaces, which transmit the information from one subdomain to the other (Luo et al., 1994). An example of the applicability of the MRF is a baffled stirred tank, where one subdomain is the region around the impeller and the rest (walls of the tank and baffles) belongs to the second subdomain. In this case, the reference frame is applied to both subdomains, but the speed of each frame of reference is different: $\boldsymbol{\omega}$ for the rotating frame of reference and 0 for the stationary frame of reference. This method is only applicable when small variations in the flow dynamics occur in the latter frame of reference when the relative orientation of impeller blades/baffles is modified (Khan et al., 2004).

The MPM follows the same principles as the MRF, and the main difference is how the information is transmitted across the interfaces (Denton and Singh, 1979). In this case, the variables are averaged circumferentially before they are passed from one zone to the other to remove the differences in the tangential direction. This is often suitable when dealing with turbomachinery with rotor-stator elements (Marshall and Bakker, 2004).

Finally, the SM method can be used to model moving parts, and provides a time-dependent solution. Similarly to the MRF and MPM, the domain needs to be split into two subdomains, a moving one and a stationary one. For a mixing tank, the grid of the moving subdomain rotates at the same speed as the impeller, and it is updated at each time step, while the stationary mesh remains unchanged. The boundary between the two meshes needs to be a surface of revolution to allow the mesh to rotate relative to one another.

2.3.4. Modelling single phase multicomponent flows

Mixing two miscible chemical species is a particular case of a multiple component single phase flow. In this case, chemical species are scalars, and they can be modelled with transport equations of the following form:

$$\frac{\partial}{\partial t}(\rho Y_i) = -\nabla \cdot (\rho Y_i \mathbf{v}) - \nabla \cdot \mathbf{j}_i + r_i \qquad \text{(Eq. 2.26)}$$

where Y_i is the mass fraction of the i$^{\text{th}}$ species, $\frac{\partial}{\partial t}(\rho Y_i)$ is the rate of increase in mass of the i$^{\text{th}}$ species per unit volume, $-\nabla \cdot (\rho Y_i \mathbf{v})$ is the rate of addition of mass of the i$^{\text{th}}$ species by convection per unit volume, $-\nabla \cdot \mathbf{j}_i$ is the rate of addition of mass of the i$^{\text{th}}$ species by diffusion per unit volume, and r_i is the rate of production of mass of the i$^{\text{th}}$ species per unit volume by reaction (Bird, 2002).

Different expressions can be found in the literature for $\mathbf{j}_i$, and the simplest one is the Fick's law, which is a good approximation for isothermal binary systems (Bird, 2002):

$$\mathbf{j}_i = -\rho D_{i,m} \nabla Y_i \qquad \text{(Eq. 2.27)}$$

where $D_{i,m}$ is the mass diffusivity of the i$^{\text{th}}$ species in the mixture m (Bird, 2002).

Eq. 2.26 is the mass conservation equation for the i$^{\text{th}}$ species. If N is the total number of fluid phase chemical species present in the system, N-1 continuity equations are solved. Additionally, Eq. 2.28 is needed to close the mass conservation:

$$\sum_{i}^{N} Y_i = 1 \qquad \text{(Eq. 2.28)}$$

2.4. Relevant literature of CFD applied to mixing tanks

Computational Fluid Dynamics has been extensively used by researchers since the early 1990s to model all types of fluid dynamic problems. Indeed, researchers have used CFD codes to investigate the behaviour of fluids in mixing tanks (Chapple et al., 2002, Shekhar and Jayanti, 2002, Adams and Barigou, 2007, Bulnes-Abundis and Alvarez, 2013). The three main areas of study can be classified as: (i) calculation of the power requirement for agitation, (ii) study of the velocity profiles generated by different types of mixers and hence identification of their suitability for mixing, and (iii) estimation of mixing time. In general, the contribution of these types of articles lies on the novelty of the mixer design or in the evaluation of a particular design to mix fluids with complex rheological properties. One key aspect about CFD models developed for mixing equipment is the necessity of validation, generally via experimental work.

2.4.1. Prediction of power consumption

2.4.1.1. Experimental considerations

The power required for an impeller to efficiently move a fluid is a key design variable. For single phase agitation, power consumption depends on the geometry of the impeller, the impeller speed N [rev s^{-1}], the geometry of the tank, presence of baffles, and the fluid density ρ [kg m^{-3}] and viscosity μ [Pa s]. Experimentally, there are different ways to measure the power required for fluid agitation, with torquemeters the most used devices (Ascanio et al., 2004). Torque measurements can be used to calculate power consumption as:

$$P = 2\pi N M \qquad \text{(Eq. 2.29)}$$

where P is the power required [W] and M [N m] is the measured torque.

An alternative to measure power consumption is to use an air bearing system (Paul et al., 2004, Nienow and Miles, 1969); this is a simpler alternative to torquemeters, as there is no need to calibrate the instrument, and it is more robust against impeller vibrations. The air bearing is made of metal, has a cylindrical shape and consists of three parts: a main body, an air distribution plate and a rotational table. Air is pumped into the main body via a nozzle at the bottom of the air bearing and reaches the distribution plate at the top. The distribution plate has many holes at its periphery that generate a uniform air layer above it, which lifts the rotational plate. If a stirred tank is placed on top of the rotational plate, the tank is lifted with the plate. When the mechanical stirrer starts rotating, the force transmitted by the impeller to the fluid, and eventually to the tank, makes the tank and the rotational plate rotate at the same angular speed as the impeller. From the force that is required to stop the rotation of the rotational plate, the torque applied by the impeller, and thus the power required to agitate the fluid, can be calculated. This force is measured with a load cell. To measure the force, an arm attached to the rotational plate is brought to rest on the load cell. A schematic of this device is shown in Figure 2. 5. The power required is calculated using the following equation:

$$P = 2\pi NFx \qquad \text{(Eq. 2.30)}$$

where P [W] is the power required to drive the impeller, N [rev s^{-1}] is the impeller speed, F [N] is the force measured by the load cell, and x [m] is the radial distance from the axis of rotation of the impeller to the application point of the force F (at the centre of the measuring surface of the load cell).

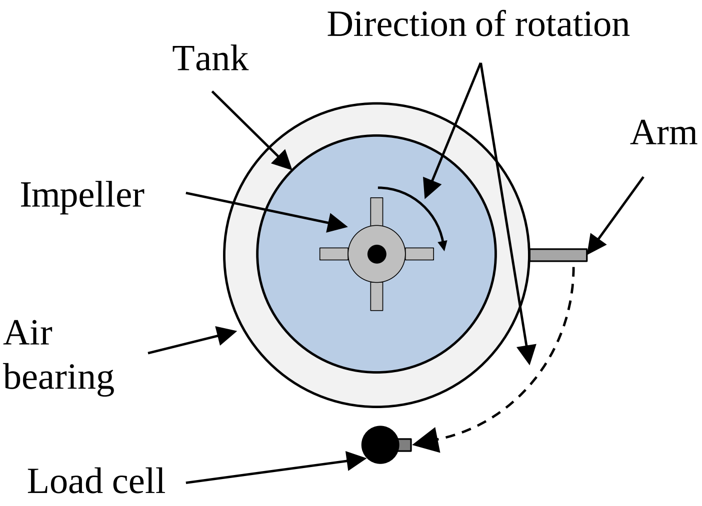

Figure 2. 5. Schematics of a mixing tank equipped with a combination of an air bearing and a load cell to measure power requirement

Using dimensional analysis to geometrically similar mixing tanks in the absence of vortex formation with Newtonian fluids, it is possible to prove that only two dimensionless groups are important: the Reynolds and the power numbers (Bates et al., 1963):

$$Re = \frac{\rho N D^2}{\mu} \tag{Eq. 2.31}$$

$$P_o = \frac{P}{\rho N^3 D^5} \tag{Eq. 2.32}$$

where Re is the Reynolds number and Po is the Power number, ρ [kg m^{-3}] is the density of the fluid, and D [m] is the diameter of the impeller. In case of vortex formation, the Froude number would also be important. Generally, vortex formation is undesired, and efforts are often made to eliminate its presence. For this reason, for the rest of this section, vortex formation is ignored.

Power curves are graphical representations of the power number against the Reynolds number. A typical power curve is shown in Figure 2. 6.

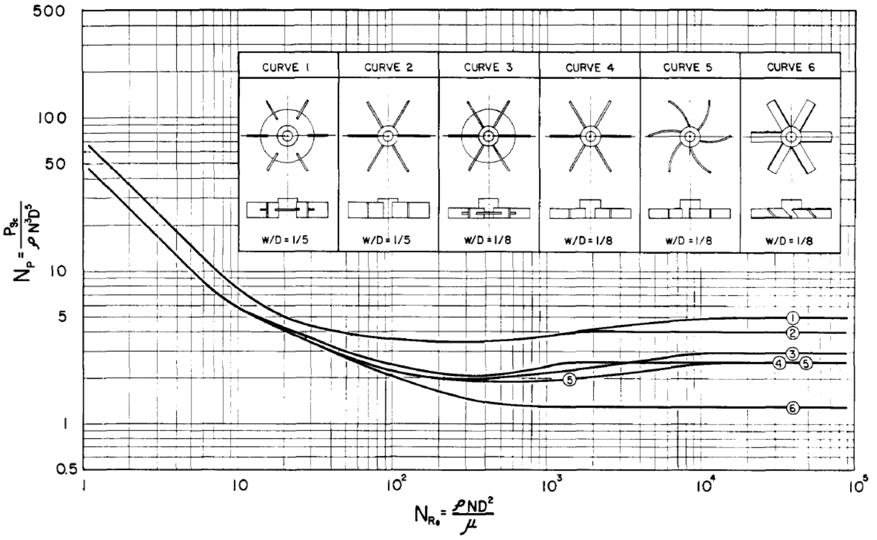

Figure 2. 6. Typical power curve for different impeller geometries (Bates et al., 1963)

Power curves have three different zones corresponding to the three possible regimes. The laminar regime corresponds to the left-hand side of the curve, where a linear decrease of the power number versus the Reynolds number occurs. In a log-log plot the slope has a constant value of -1, and the relationship of the Reynolds and Power number is as in Equation 2.33,

$$P_o = \frac{K_p}{Re} \qquad \text{(Eq. 2.33)}$$

where K_p is the power constant, which is characteristic of the impeller geometry.

On the right-hand side of the power curve it is possible to identify the turbulent regime, which is characterised by a constant value of the power number, which is independent of the Reynolds number and only depends on the geometry of the impeller and the tank. Finally, the section in-between these two extremes is the transition zone.

Metzner and Otto (1957) extended this analysis to generalised Newtonian fluids (as defined in section 2.2.1, time independent non-Newtonian fluids) that can be modelled with the power law model. In this case, the power law index (n) is the third dimensionless number required to close the dimensional analysis. In the laminar regime one can define an average shear rate for the impeller that depends only on the impeller rotational speed and on a characteristic constant of the impeller geometry (K_s):

$$\dot{\gamma}_{avg} = K_s\, N \qquad \text{(Eq. 2.34)}$$

Then, the non-Newtonian viscosity of the system, also called effective viscosity or apparent viscosity by the authors, can be calculated using the averaged shear rate described in Eq. 2.35:

$$\mu_{ef} = K(\dot{\gamma}_{avg})^{n-1} \qquad \text{(Eq. 2.35)}$$

Combining Eq. 2.31 and Eq. 2.35, the Reynolds number can be written as:

$$Re = \frac{\rho N D^2}{\mu_{ef}} = \frac{\rho N^{2-n} D^2}{K\, {K_s}^{n-1}} \qquad \text{(Eq. 2.36)}$$

Rieger and Novak (1973) proved that in the laminar regime, with generalised Newtonian fluids that can be modelled with the power law, the dependency of the power number on the Reynolds number is as follows:

$$Po = \frac{C(n)}{Re} \qquad \text{with} \qquad C(n) = K_p {K_s}^{n-1} \qquad \text{(Eq. 2.37)}$$

where K_p is the same constant as in equation 2.33, and K_s is the same constant as in equation 2.34. For Newtonian fluids, the power law index has a value of 1, and immediately it is possible to see that the straight line with slope of -1 in the power number against the Reynolds number in a double logarithmic plot is fulfilled.

2.4.1.2. Computational considerations

Power consumption is probably the most common approach to validate CFD models of stirred tanks. Computationally, the power consumption is calculated from the torque applied by the impeller to the fluid:

$$\boldsymbol{M} = \int_{A_I} \mathbf{r} \times (\boldsymbol{\pi} \cdot \mathbf{n}) dA \qquad \text{(Eq. 2.38)}$$

where **M** is the overall moment of the stress force about the point located at the bottom of the tank on the axis of rotation of the impeller (the z-axis), **r** is the position vector, **n** is the unit vector normal to the surface, A_I is the surface of the impeller and $\boldsymbol{\pi}$ is the stress tensor, equal to:

$$\boldsymbol{\pi} = p\boldsymbol{I} + \boldsymbol{\tau} \qquad \text{(Eq. 2.12 bis)}$$

where *p* is the fluid dynamic pressure, ***I*** is the identity tensor and $\boldsymbol{\tau}$ is deviatoric stress tensor of the fluid.

The power consumption of the impeller can easily be calculated using the following equation:

$$P = 2\pi N M_z \qquad \text{(Eq. 2.39)}$$

where M_z denotes the axial component (that is, the component in the z direction) of the vector **M**, and *N* is the impeller angular speed in rotations per unit time.

In the recent literature on non-Newtonian fluid mixing, researchers have extensively used torque meters or alike experimental equipment to measure power consumption mainly for validating CFD models, as in the following studies. Ameur (2015) studied the efficiency of four impeller configurations (Maxblend, gate, anchor, and double helical ribbon) for mixing yield stress fluids; he used experimental power consumption data available in the literature (Patel et al., 2012) for the anchor and Maxblend impellers to validate the model. Zhang et al. (2014) measured the power during mixing of corn-stover and water (shear thinning fluid) at three different scales (5, 50, and 500 litres), and used the findings to validate a CFD model. Pakzad et al. (2013a) studied computationally and experimentally the hydrodynamics and the mixing performance of a coaxial impeller that combined Scaba and anchor geometries for the mixing of yield stress fluids. They developed a correlation for the specific master power curve (power number versus generalised Reynolds number) that applies to the particular system investigated, which they used to validate a CFD model.

2.4.2. Velocity fields generated in stirred tanks

2.4.2.1. Particle Image Velocimetry

In Section 2.1, the concept of flow patterns was introduced, and their importance when designing mixing systems was discussed. Flow patterns provide qualitative information about flow circulation inside a stirred tank with a given impeller geometry. Quantitative flow measurement and in particular quantitative flow visualization techniques are much more valuable to understand the mechanics of a particular flow. Particle image velocimetry (PIV) is the state-of-the-art of optically based diagnostics tools for fluid mechanics. PIV is a non-intrusive quantitative technique that relies on the tracking of small tracer particles introduced in a fluid in motion to identify their velocity. To do so, neutrally buoyant tracer particles are seeded into the flow. A camera and a laser are synchronised to take two consecutive snapshots of the flow, and the velocity is calculated from the displacement of the particles in the time difference between the two laser pulses. Hence, the basic requirements for a PIV system are an optically transparent test-section, an illuminating light source (laser), an arrangement of lenses to transform the laser beam into a sheet, a recording hardware (camera), and a computer and specific software for image processing (Adrian and Westerweel, 2011).

PIV does not track each particle individually; instead, the ensemble of particles within an interrogation area is tracked. An interrogation window (W) is generally formed by n-number of pixels. Typically, 16x16, 32x32, and 64x64 pixels are used. Figure 2. 7 shows schematically the particle displacement within four interrogation windows. Blue and red dots correspond to particles captured in the first and second frames respectively.

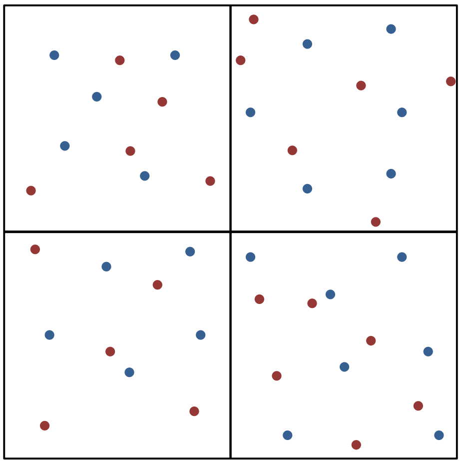

Figure 2. 7. Schematic representation of particles captured by a camera in four interrogation windows in a hypothetical PIV experiment. Blue and red dots correspond to the first and second images respectively

When adequate hardware is used, the fluid can be completely masked, and the camera captures only the position of the particles that are emitting sufficiently intense light; in other words, those that are illuminated by the laser on the plane of interest. In this case, each interrogation window has a specific intensity distribution (**I**). The aim of PIV is to find the average displacement of the particles in the interrogation window that makes the intensity distribution of the two images of the pair overlap. The mathematical expression of this is the cross-correlation function for an interrogation window:

$$R(\boldsymbol{s}) = \int_W \boldsymbol{I}_1(\boldsymbol{X})\boldsymbol{I}_2(\boldsymbol{X}+\boldsymbol{s})d\boldsymbol{X} \qquad \text{(Eq. 2.40)}$$

Where W is the interrogation window, $\boldsymbol{I}_1$ and $\boldsymbol{I}_2$ are the intensity distributions of the window on images 1 and 2 respectively, $\boldsymbol{X}$ is the grid point and $\boldsymbol{s}$ is the displacement or shift of the second image with respect to the first one. Typically, the 3D representation of $R(\boldsymbol{s})$ is a series of peaks within the $\boldsymbol{s}$-plane, and the objective of PIV is to locate the sharpest peak of $R(\boldsymbol{s})$, which determines the average displacement of the particles within the interrogation window. A schematic of this can be found in Figure 2. 8. Note that Figure 2. 8 is not the $R(\boldsymbol{s})$ profile of the example shown in Figure 2. 7.

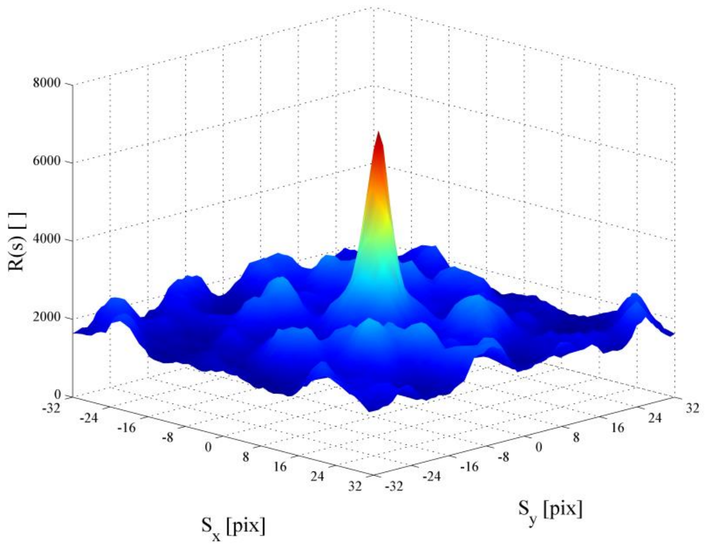

Figure 2. 8. Schematic representation of the correlation function for a 64 by 64 pixel interrogation window

Velocity vectors can be calculated from the average displacement of the particles in the interrogation window, the time difference between the images, and a pixel-to-distance scaling factor.

2.4.2.2. Validation of CFD models using PIV

CFD allows assessing the performance of stirred vessels in a more efficient manner than experimentally. As previously mentioned in Section 2.4, validation of CFD models is of major concern. PIV is a suitable method for this endeavour. To name a few examples, Sossa-Echeverria and Taghipour (2015) obtained velocity profiles of yield stress and shear thinning fluids stirred with three different side-entered axial flow impellers using particle image velocimetry (PIV) and they evaluated the cavern formation around the impeller. Comparable results were found with the CFD model.

Couerbe et al. (2008) studied the agitation of thixotropic shear thinning fluids exhibiting yield stress with a Mixel TT agitator (axial impeller) both experimentally with PIV and computationally (ANSYS CFX) in the laminar regime. They used both the modified Hershel-Bulkley model (Zhu et al., 2005) and the Coussot model simplified for steady state flows (Coussot et al., 2002). Comparable computational results were obtained in the sheared region, which indicates the applicability of simple rheological models such as the Herschel-Bulkley to model more complex characteristics such as thixotropic behaviour. Numerical simulations predicted the essential features of the flow, such as cavern formation, the location of recirculation regions and the overall magnitude of the velocities. Agreement of the computational and experimental results was achieved by covering the blades of the impeller with waterproof sand paper, which ensured the no-slip condition on these surfaces used in the simulation.

Arratia et al. (2006) used PIV as well as planar laser induced fluorescence (PLIF) and ultraviolet (UV) fluorescence to study velocity profiles and cavern formation during the mixing of glycerine and of a Herschel-Bulkley fluid (aqueous 0.1% Carbopol solution) with a centred triple Rushton turbine. They modelled the system with CFD and found good agreement with the experiments. They observed strong compartmentalization due to the yield stress, and they concluded that the mixing of shear thinning fluids with yield stress is enhanced by breaking the symmetry of the impeller.

2.4.3. Estimation of mixing time

2.4.3.1. Measuring mixing

Mixing is defined as a unit operation used to reduce heterogeneity in a system (Paul et al., 2004). Heterogeneities can appear in any form such as temperature, chemical composition, size or distribution. Figure 2. 9 shows a closed system completely segregated into A and B. Figure 2. 9 will help in the discussion that follows. A and B do not necessarily refer to chemical species, but to any heterogeneity of the system.

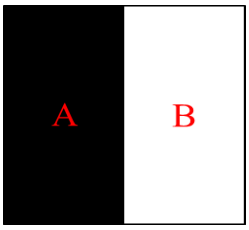

Figure 2. 9. Representation of a closed system completely segregated.

Mixing is achieved by two mechanisms: convection and diffusion. Convection refers to bulk motion, and diffusion to the spreading of segregated zones into one other. Often, the literature refers to macromixing when convection dominates and to micromixing when diffusion dominates, although other nomenclatures can also be found (Paul et al., 2004).

There are two main variables used to quantify mixing: intensity of segregation and scale of segregation (Kukukova et al., 2009, Danckwerts, 1952). Taking as an example the blending of two miscible fluids in a confined system in which the concentration can be measured at a certain number of points, intensity of segregation quantifies how much the concentration at those measuring points deviates from the mean. Generally, the concept of coefficient of variation (CoV) is used, which is the standard deviation of the concentration over the mean concentration:

$$\mathrm{CoV} = \frac{\sigma}{\bar{C}} = \sqrt{\frac{1}{N_t}\sum_{i=1}^{N_t}\left(\frac{C_i - \bar{C}}{\bar{C}}\right)^2} \qquad \text{(Eq. 2.41)}$$

where N_t is the number of measuring points, C_i is the concentration at the ith measuring point, $\bar{C}$ is the mean concentration of C_i, and σ is the standard deviation.

A typical example where the intensity of segregation can be used to calculate the degree of mixing is presented in Figure 2. 10 a). In this case, the concentration is represented on a greyscale, and the value of the mean concentration is constant during the mixing process, but the standard deviation of the concentration, and hence the CoV, will decrease as mixing progresses until these variables plateau at a constant value (Kukukova et al., 2009).

Scale of segregation measures the lengthscale that separates the heterogeneities of the system. Different methods are available to compute the scale of segregation (Kukukova et al., 2011). Despite its simple definition, scale of segregation is a rather difficult concept to apply to three dimensional flows, and it is sometimes impractical in applications where there is no clear interphase between the two segregated areas, or when there are smooth gradients of the variable of interest between the two segregated zones. Figure 2. 10 b) is an example of a case where the scale of segregation method can be used to quantify the mixing (Kukukova et al., 2011).

Figure 2. 10 c) shows a more realistic mixing process, where both reduction in the intensity and scale of segregation happen simultaneously.

a) Reduction in intensity of segregation only:

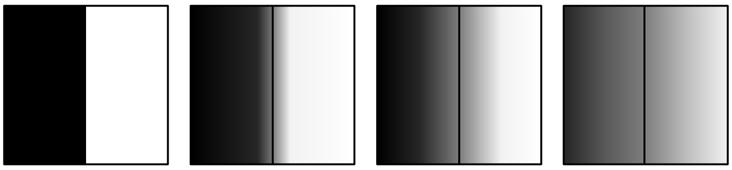

b) Reduction in scale of segregation only:

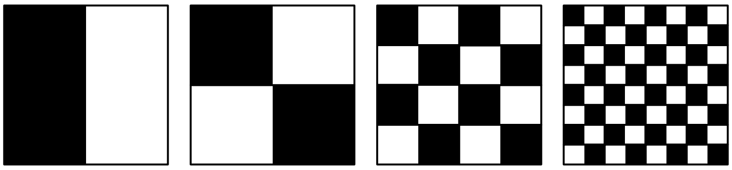

c) Simultaneous reduction of intensity and scale of segregation:

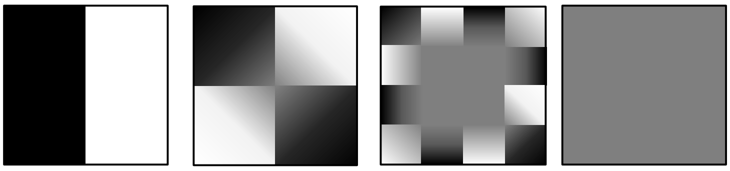

Figure 2. 10. Examples of cases where a) intensity of segregation and b) scale of segregation can be used to calculate degree of mixing. c) shows a mixing problem where both, intensity of segregation and scale of segregation, can be simultaneously. Adapted from (Paul et al., 2004)

2.4.3.2. Experimental considerations

Mixing time is defined as the time required for achieving a certain degree of homogeneity, and often, it refers to two or more fluids/chemical species that are initially segregated. Most methodologies to experimentally evaluate mixing time are based on the injection into the system of a tracer with similar physicochemical properties to the bulk fluid except one, and tracking that different property over time until a new steady state for that property is reached. Techniques such as colorimetry or conductometry have been widely used because of their simplicity. However, they have severe limitations, such as difficulty of obtaining quantitative data from a colorimetric experiment, or the scarcity of data points and the flow intrusiveness of the conductometry (Ascanio, 2015). For these reasons, more sophisticated techniques are preferred. The current state-of-the-art in experimental mixing time estimation is the use of optically based tools for flow diagnostics, and in particular, the planar laser induced fluorescence (PLIF) technique.

The main components of a PLIF setup are practically identical to those of the PIV: an optically transparent test-section, an illuminating light source (laser), an arrangement of lenses to transform the laser beam into a sheet, a recording hardware (camera), and a computer and specific software for image processing. Nevertheless, the principle is completely different. In this case, the variable of interest is the intensity of light emitted by a fluorescent dye, which often is correlated to the concentration of the tracer, and not the velocity of the fluid. Moreover, there is no need to cross-correlate pairs of images to calculate derivative properties such as velocity; instead, single snapshots of the system are taken per laser pulse.

In PLIF, the bulk fluid can be completely masked using a filter. Images are intensity distribution profiles, and with appropriate calibration, direct conversion from intensity of light to concentration can be obtained (Baumann and Mühlfriedel, 2002). For low concentrations of fluorescent dye, the intensity or fluorescence signal (I) recorded on the camera can be modelled as (Paul et al., 1990):

$$I_i = A\ E\ \Phi\ C_i \qquad \text{(Eq. 2.42)}$$

where A is a factor that accounts for the optical collection arrangement and the characteristics of the camera, E denotes the energy per laser pulse, Φ is the effective quantum yield, C is the concentration of the dye, and the subindex i refers to a given pixel. The ability to convert the signal, I, to concentration, C, depends on the ability to accurately determine (or factor out as constants) the parameters A, E, and Φ throughout the imaged region (Karasso and Mungal, 1997).

Time-resolved concentration profiles can be used to estimate mixing time. There are two common approaches to do so. The first method consists in selecting a number of points in the flow domain and plotting the evolution of the concentration in those points over time (Pakzad et al., 2013b). Careful selection of these points is critical in the study, particularly in cases with segregated zones where almost no mixing occurs. The second method is based on the concept of intensity of segregation presented by Danckwerts (1952), also reviewed in Section 2.4.3.1. In this case, the standard deviation of the concentration distribution is calculated and plotted over time. If the tracer and bulk fluids are initially segregated, an initial decay and a subsequent plateau in the standard deviation of the concentration are expected. Different criteria can be used to estimate mixing time, and the most common ones are 90%, 95%, and 99.5% of the proximity to the plateau (Paul et al., 2004).

2.4.3.3. CFD as a tool to predict mixing time

A number of studies have looked at the variation of properties in mixing system over time as a validating tool for CFD models. Kazemzadeh et al. (2016) studied the mixing time and efficiency of a coaxial mixer (Scaba-anchor system) using yield stress fluids. They developed a CFD model of the mixing system, and they validated experimentally the model using the electric resistance tomography (ERT) technique: they injected a tracer in the mixer and they tracked the concentration of it over time at different positions in the vessel. Then, they analysed the effect of the yield stress coefficients together with the speed ratio of the two impellers on the mixing time and power consumption.

Hurtado et al. (2015) developed a CFD model of a continuous stirred tank reactor (CSTR), used in wastewater treatment plants, agitated by recirculation of material (without mechanical stirrer). To validate the model experimentally, they introduced particles in the system and measured their concentration in the outlet line over time. Patel et al. (2015) developed a CFD model of a baffled stirred tank fitted with a Rushton turbine to quantify the mixing over the stagnant areas volume fraction as a function of the rheological properties of yield stress materials in continuous flow. To evaluate this, a tracer was injected into the inlet and the conductivity of the mixture was measured over time in the outlet. The good agreement between experiments and modelling in the works above demonstrated the applicability of this validation methodology (i.e. monitoring the change of properties over time).

2.4.3.4. Laminar mixing

Laminar mixing is common in processes dealing with high viscous fluids, non-Newtonian fluids, or shear sensitive fluids. Despite the general opinion that laminar mixing is ineffective, quite the opposite is true, although it generally requires significantly more time than turbulent mixing (Paul et al., 2004). Laminar mixing is currently best described from a dynamical systems perspective, and this theory is limited to incompressible fluids in the absence of molecular diffusion, which in general represents best highly viscous fluids (Ottino, 1989). Laminar mixing is achieved by a series of consecutive folding and stretching operations that increase the intermaterial contact area exponentially. It is clear that the objective of mixing in this context is to reduce the scale of segregation up to the point where diffusion takes place. A schematic of this is known as "baker's map", and this can be found in Figure 2. 11.

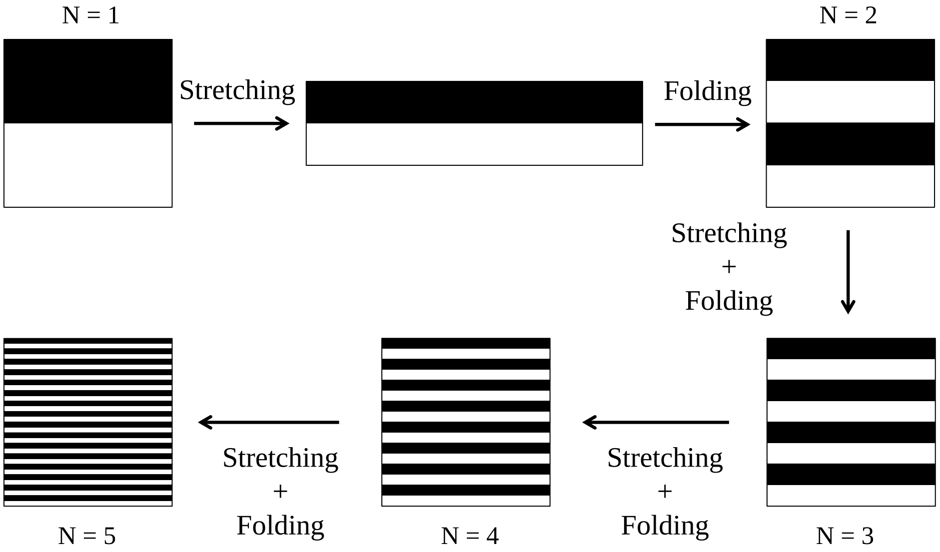

Figure 2. 11. Schematics of laminar mixing by consecutive stretching and folding operations, also known as baker's map. N represents periods of the flow. Adapted from (Paul et al., 2004)

Laminar mixing is known to happen because of chaotic advection. Aref (1984) was the first to introduce the concept of chaotic advection, which describes how a fully deterministic velocity field in the Eulerian view (e.g., laminar, time-dependent, and two-dimensional incompressible flow), produces a stochastic response in the Lagrangian advection characteristics of a passive tracer. These flows are non-integrable.

In contrast, integrable flows (those with analytical integral expression), lead to deterministic Lagrangian advection of passive tracers; in this case, the path-lines of the passive tracers coincide with the streamlines for the steady flow. In other words, when there is an analytical expression for the position of a passive tracer as function of time, the Lagrangian advection is considered deterministic, and if not, stochastic (Aref, 2002).

Additionally, he concluded that efficient mixing is achieved by inducing “chaos”. For instance, turbulence inherently renders a flow non-integrable. Three dimensional flows in the absence of geometrical symmetries are inherently non-integrable, even if they are time independent as demonstrated by Aref (2002).

Quantitative measurement of mixing intensities in chaotic flows is attained by computing the accumulated stretch of small fluid filaments. From a Eulerian perspective, these simulations are performed by placing small vectors in the flow. Each infinitesimal vector is deformed by the instantaneous deformation tensor (obtained with the velocity gradient) along its trajectory while being advected throughout the flow domain. The elongation experienced by each vector is directly related to the local intensity of mixing. All small vectors placed in regions of chaotic motion yield to exponential rates of stretching over time, while those in regions of regular flow yield to stretching rates that are at best linear over time (Zalc et al., 2002).

An equivalent method to compute the stretching of fluid elements using a Lagrangian perspective is to introduce massless particles on the two extremes of fluid elements. Particles are tracked over time, and the cumulative stretching experienced by the fluid elements is the distance that separates the particles. The stretching of a fluid element is calculated with Eq. 2.43:

$$\lambda = \frac{l_n}{l_0} \qquad \text{(Eq. 2.43)}$$

Where l_n and l_0 are the distances between the two particles at time n and at time 0 respectively. This can be represented schematically as in Figure 2. 12.

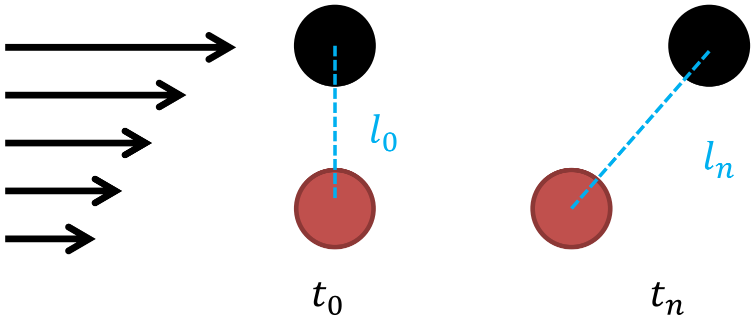

Figure 2. 12. Schematical representation of the stretching of two infinitesimally close particles

In Figure 2. 12, the arrows represent a unidirectional time independent velocity field; the red and black circles represent the two fictitious particles at initial time (t_0) and at t_n, and the dashed lines (l_0 and l_n) represent the distances that separate them. Pairs of particles can be introduced anywhere in the flow domain. High values of stretching indicate high divergence of the particles, which is clearly correlated with the definition of deterministic chaos: rapid divergence from small difference in initial conditions. Hence, chaotic flows are recognised by having stretching values higher than one. By placing these pairs of particles intelligently on the flow, one can determine effective injection locations, or in other words, locations that provide fast mixing.

Mixing efficiency can be correlated to both the geometric and the arithmetic means rate of stretching in chaotic flows represented in equations 2.44 and 2.45 respectively:

$$\langle\lambda\rangle = \left(\prod_{\mathrm{i}=1}^{N_p} \lambda_{\mathrm{i}}\right)^{\frac{1}{N_p}} \sim \mathrm{e}^{\Lambda n} \qquad \text{(Eq. 2.44)}$$

$$\bar{\lambda} = \sum_{\mathrm{i}=1}^{N_p} \frac{\lambda_{\mathrm{i}}}{N_p} \sim \mathrm{e}^{\Theta n} \qquad \text{(Eq. 2.45)}$$

In equations 2.44 and 2.45, N_p is the number of pairs of particles introduced in the flow, and n is the number of periods (e.g. number of impeller revolutions). Λ and Θ are known as the Lyapunov exponent and the topological entropy respectively.

For historical reasons, the Lyapunov exponent has been used more extensively to determine the rate of area growth in chaotic mixing processes. However, computational studies have shown that the Lyapunov exponent under-predicts the true exponential rate of area growth, and that the topological entropy predicts more accurately this parameter (Muzzio et al., 2000, Alvarez et al., 1998). Values of topological entropy can be used to quantify mixing efficiency by predicting the amount of interfacial area available provided by the mixer over time. It is important to note that there is not a reference number that quantifies how good or bad the mixing is. Instead, this number can be used to comparatively assess which conditions are better at providing mixing (Zalc et al., 2002).

Statistical analysis of the stretching field also reveals relevant information about the mixing process (Muzzio et al., 1991). Local values of stretching span over orders of magnitude. Probability distribution function of the stretching field helps to better understand how dense the chaotic zones are compared to the regular zones of the flow domain are. Self-similar probability distribution functions of the stretching over time that shifts from low values to high values of stretching as time progresses are obtained for periodic chaotic flows. This is a characteristic property of these types of flows and it is named asymptotic directionality (Muzzio et al., 2000).

3. Power analysis

3.1. Introduction

In this chapter it is first aimed to characterise the rheology of the non-Newtonian mixture of interest: glycerol and a gel made of polyethylene glycol and carbomer, which is relevant to the manufacturing of non-aqueous toothpastes, and to derive a constitutive equation for its rheology. Then, it is aimed to implement the rheological model in CFD to describe the flow behaviour of different mixtures of these two fluids in a simple mixing tank. The CFD model is validated against accurate experimental results of power consumption obtained in a simple stirred vessel with a frictionless air bearing and a load cell. The work here aims to validate the numerical approach that uses as an input the measured rheology of the mixture. For this reason, a standard Rushton turbine is used, where results on power consumption with Newtonian fluids can also be validated against literature data. Once validated, the numerical model will be used in the next chapter in a more complex stirred tank that is similar to the industrial system.

This chapter is structured as follows. In Section 3.2, the rheological study of the non-Newtonian mixture is first presented followed by the details of the experimental setup and then by implementation of the CFD model. In Section 3.3, both computational and experimental results of power consumption are compared and analysed. Finally, in Section 3.4, the main conclusions are summarised, and directions to progress towards the study of the mixing system of interest are presented.

3.2. Methodology

3.2.1. Fluids

The fluids of interest in this research are glycerol and a carbomer gel made of polyethylene glycol (96%) and carbomer (4%). The rheological properties of glycerol are available in the literature (Green, 2008), but the rheology of the carbomer gel has not been studied before. The aim of this subsection is to derive a constitutive equation that relates the fluid viscosity with the gel mass fraction, temperature and shear rate:

$$\eta = f(x_{gel}, T, \dot{\gamma}) \qquad \text{(Eq. 3.1)}$$

The boundaries of the design space need to cover the range of the real mixing process. Moreover, a finite but sufficiently large number of rheological measurements need to be made to obtain accurate parameters to describe the constitutive equation, regardless of the shape of the constitutive equation. The first of the three variables, the gel mass fraction, has two physical boundaries: 0 and 100 %. The whole range needs to be explored for the equation to be valid during the mixing process. The whole range of gel mass fraction was divided in intervals of 10%, leading to 11 mixtures including the two pure compounds.

In the pilot plant scale mixer, the mixing process takes place at approximately 60 ºC. However, previous thermal measurements indicated that the temperature varied from 35 ºC to 85 ºC in different points of the vessel. Since temperatures were only measured in a finite number of points, one can assume that temperatures might be as low as the room temperature (25 ºC). Hence, each mixture was studied at thirteen equally-spaced temperatures, between 25 ºC and 85 ºC.

For each gel mass fraction and temperature considered, the viscosity of the mixture was evaluated at fifteen equidistant points in a logarithmic scale of shear rate in the range of 1-250 s^{-1}. This range is similar to that in other studies (Ramsay et al., 2016, Sossa-Echeverria and Taghipour, 2014, Pakzad et al., 2013c), and is the recommended one for laboratory-scale mixing processes (Schramm, 1994).

The measurements were carried out in an Anton Paar Physica MCR 301 rheometer with parallel plate geometry (Figure 3. 1).

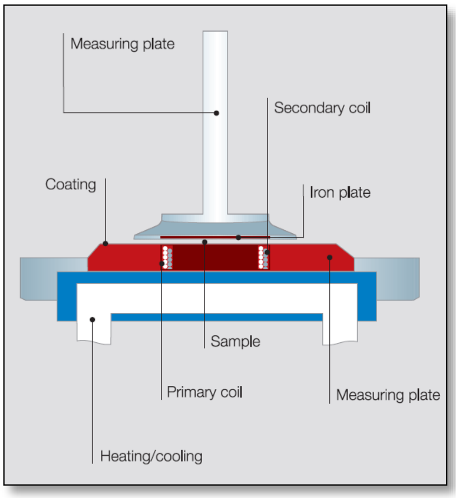

Figure 3. 1. Representation of the rheometer (Anton-Paar, 2009)

In this configuration, the stress applied to the fluid is not constant in the radial direction, and the viscosity is evaluated at the rim of the plate. At this location, the magnitude of the shear rate is maximum, and is defined as:

$$\dot{\gamma}_R = \frac{\Omega R}{h} \quad \text{(Eq. 3.2)}$$

where Ω is the rotational speed of the upper plate, R is the radius of the upper plate, and h is the gap size, or the distance between the two plates. The corresponding stress for any generalised Newtonian fluid is (Macosko, 1994):

$$\tau_R = \frac{M}{2\pi R^3}\left[3 + \frac{\mathrm{d}\ln(M)}{\mathrm{d}\ln(\dot{\gamma}_R)}\right] \qquad \text{(Eq. 3.3)}$$

where M is the torque applied to the upper plate. These equations are used by default by the software of the rheometer, so no special treatment is needed. For detailed information on how to obtain Eq. 3.3, the reader is referred to Appendix I.

For this study, a cone and plate geometry would have also been desirable, but this latter configuration is not recommended for temperature sweeps due to thermal expansion of the materials (Schramm, 1994).

The main source of error of the rheological experiments comes from the heterogeneity in the samples. The rheological experiments were repeated at least twice, and the average standard deviation of all rheology data is 4.55%. Within the shear rate range considered, the error associated with the accuracy of the instrument is negligible.

3.2.1.1. Protocol of rheological measurements

The gel was prepared following the GSK protocols, which cannot be disclosed here. Then, it was used to create the eleven glycerol mixtures described above, and they were stored in glass containers (30 ml). The procedure to study the viscosity was as follows:

(1) Introduce one sample in the rheometer at room temperature.

(2) Set the temperature at 25 ºC.

(3) Set the shear rate at 1 s^{-1}.

(4) Record the viscosity after the value is stabilised.

(5) Set the shear rate according to the next value, and go to (4). If all shear rate values have been evaluated, then, go to (6).

(6) Increase the temperature by 5 ºC, and go to (3). If 85 ºC has been evaluated, then, go to (7).

(7) Increase the gel mass by 10 %, and then go to (1). If all values of gel mass fraction have been evaluated, the experiment is finished.

The procedure needs to be repeated twice to eliminate experimental errors. Then, the resulting viscosity needs to be averaged, and the averaged values will be used to determine the constitutive expression presented in Eq. 3.1.

3.2.1.2. Rheological results

Indicative results are shown in Figure 3. 2, which correspond to low and high values of gel mass fraction in the mixture (40% and 80%) and to low and high values of temperature (40ºC and 60ºC).

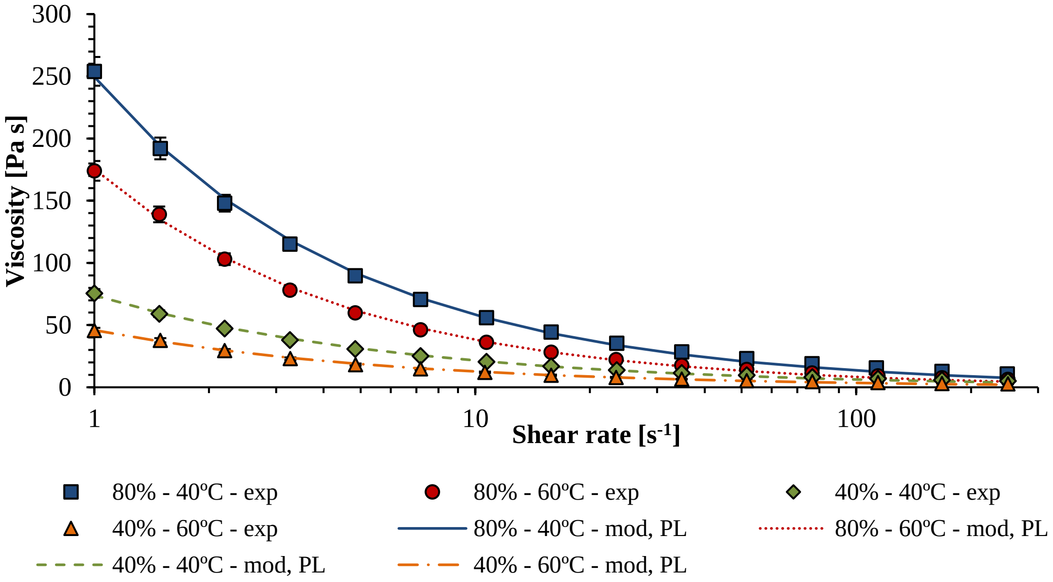

Figure 3. 2. Viscosity profile of samples at different gel mass fractions and temperatures, power law fitting

The rheological data obtained were used to fit the parameters K and n of the power law model. In this optimisation problem, the least-squares method was used, where the objective function to minimise is the cumulative relative error between the experimental and the modelled viscosity. For the four cases shown in Figure 3. 2, the values of these parameters are presented in Table 3. 1. This same approach was followed for all conditions studied, and a total of 143 values for each coefficient, K and n, were determined, which correspond to the 11 gel mass fractions and 13 temperatures considered (Appendix II). The coefficients can be calculated at any value of gel mass fraction from 0 to 1 and temperatures from 25 to 85 ºC through linear interpolation. The mean fitting errors for each set of data were calculated using Eq. 3.4 and are also presented in Table 3. 1.

$$\text{Mean error } [\%] = \frac{1}{N}\left[\sum_{i=1}^{N}\frac{|y_{i,\text{exp}} - y_{i,\text{m}}|}{y_{i,exp}}\right] 100 \qquad \text{(Eq. 3.4)}$$

here, $y_{i,\text{exp}}$ and $y_{i,\text{m}}$ are the experimental and modelled values for each set of data, i denotes the number of discrete values and N is equal to 15, which corresponds to the number of shear rate values included in the study for each gel mass fraction and temperature. The mean percentage errors in the estimation of the K and n coefficients for the remaining cases can be found in Appendix II.

Table 3. 1. Coefficients of the power law model for different gel mass fractions and temperatures

Gel mass fraction	**Temperature [ºC]**	**K [kg s$^{(n-2)}$ m^{-1}]**	**n [ ]**	**Mean error [%]**
80%	40	249.55	0.3670	8.36
80%	60	175.28	0.3390	7.42
40%	40	73.88	0.4630	5.66
40%	60	45.91	0.4410	6.51

Additionally, the rheological results presented in Figure 3. 2 were used to fit the Herschel-Bulkley model (Eq. 2.9). The same approach as that described above was followed to obtain the constants of the constitutive equation. Very good agreement was found with the experimental data presented in Figure 3. 3.

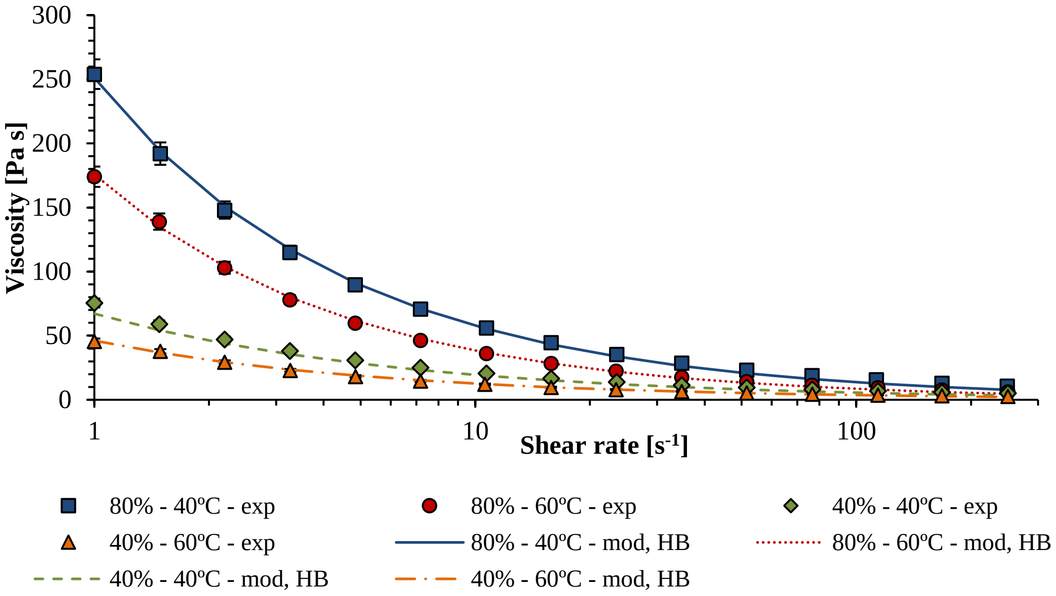

Figure 3. 3. Viscosity profile of samples at different gel mass fractions and temperatures, Herschel-Bulkley fitting

From Figure 3. 2 and Figure 3. 3 it is possible to see that both the power law and the Herschel-Bulkley are adequate models to describe the viscosity of these mixtures in the range of shear rates and temperatures explored. Hence, it is possible to conclude that any of the two rheological models can be used indistinctively for this particular piece of work. The coefficients of the Herschel-Bulkley model are presented in Appendix III.

3.2.1.3. Viscoelasticity

Carbomers are high molecular weight synthetic polymers of acrylic acid that are widely used in the pharmaceuticals and consumer healthcare industries as thickening agents (Barry and Meyer, 1979). A wide number of carbomer formulations are available. Carbomer gels are usually prepared as dispersions of carbomer molecules in water, albeit other water-miscible solvents are also used instead (Bonacucina et al., 2004). The rheological properties of carbomer gels dramatically depend on the combination of carbomer molecule and solvent, pH, and temperature. Viscoelasticity is associated to carbomer gels (Coussot et al., 2009, Bonacucina et al., 2004, Barry and Meyer, 1979). When sufficiently high shear stresses are present, the viscous component dominates over the elastic component, and a number of studies have been presented to derive constitutive expressions to relate the viscosity of carbomer gels with the shear rate; investigators modelled carbomer gels as very highly viscous shear thinning fluids and as Bingham pseudoplastic materials, often with the Herschel-Bulkley model (Islam et al., 2004, Kim et al., 2003, Amanullah et al., 1997, Barry and Meyer, 1979).

Oscillatory rheological measurements were taken to evaluate the viscoelastic response of different mixtures of carbomer gel in glycerol. The results obtained for the 20% gel mixture are presented as an example, as this is the composition of the industrial product. For this test, the same parallel plate geometry was used, and amplitude sweep tests was conducted at constant frequency of 1 Hz for the same temperatures as the rotational rheological studies. The storage G' and the loss G'' moduli and the phase angle δ were evaluated at 40 equidistant points in a logarithmic scale for controlled strains between 0.01 $[\frac{m}{m}]$ to 500 $[\frac{m}{m}]$.The results obtained for the case of 20% gel mixture at 40 ºC are shown in Figure 3. 4. Similar curves were obtained for the same gel mass fraction at the other temperatures, and hence, they are not presented here. Figure 3. 4 reveals that, for this specific case, the viscous response dominates over the elastic one, as the phase angle (δ) between the applied strain and the stress response is above 45º, over the entire curve (Schramm, 1994).

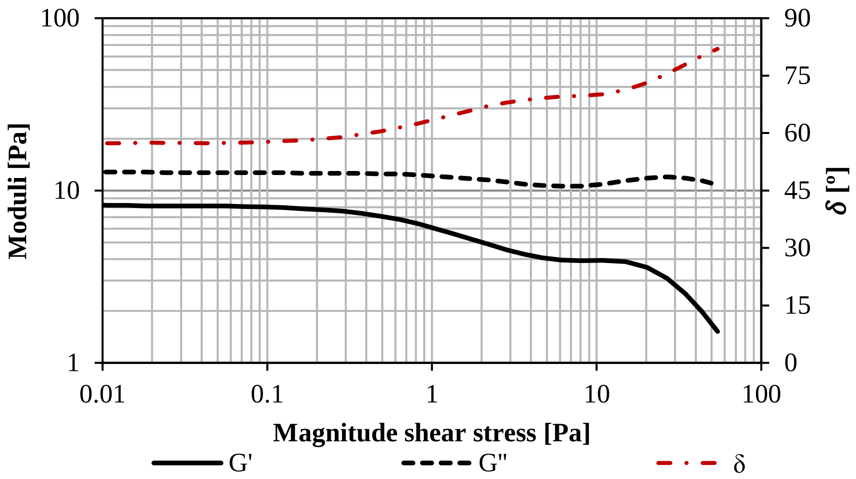

Figure 3. 4. Storage (G') and loss (G'') moduli, and phase angle (*δ*) against the oscillatory shear stress for the 20% gel mixture at 50 ºC

At higher gel mass fractions, the storage modulus is greater than the loss modulus at low values of the shear stress magnitude, and this is reversed when the magnitude of the shear stress is increased; an example for the 100% gel mixture at 50ºC is shown in Figure 3. 5. This indicates that the viscous behaviour is more relevant than the elastic one above a certain value of the magnitude of the shear stress, where the value of *δ* is equal to 45º.

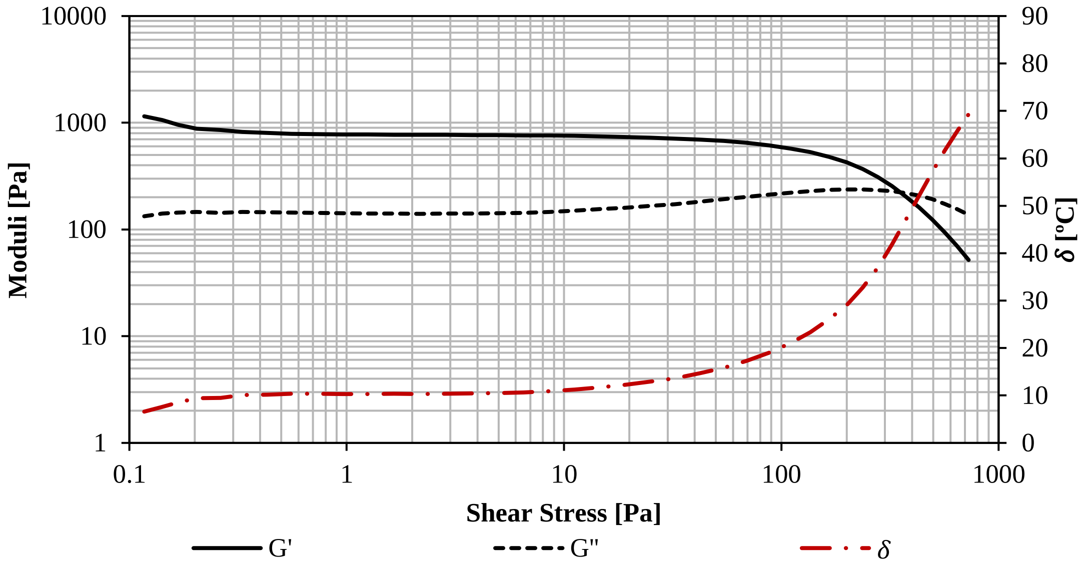

Figure 3. 5. Storage (G') and loss (G'') moduli, and phase angle (*δ*) against the oscillatory shear stress for the 100% gel mixture at 50 ºC

From the oscillatory results and the constitutive equations of the viscosity, one can find the shear rate value that corresponds to the transition from the elastic-dominant behaviour to the viscous-dominant behaviour. These are evaluated for all cases presented in this thesis, and they are presented in Table 3. 2.

Table 3. 2. Magnitudes of shear stress and shear rate at which the phase angle is 45 º

Gel mass fraction [%]	T [ºC]	Transition shear stress [Pa]	Transition shear rate [s^{-1}]
100	40	557	7
100	60	354	7
80	40	505	7
80	60	335	7
60	40	327	4.9
60	60	215	5
40	40	75.7	1
40	60	58	1.5
20	40	---	---
20	60	---	---

As it will be proved later on in Section 3.3.2.3, the value of the transition shear rate is smaller than the average shear rate calculated using the Metzner-Otto approach (Eq. 2.34) (Metzner and Otto, 1957). As this setup is used to evaluate the power consumption of the impeller using the working fluids presented in Table 3. 1, and this is computed on the surface of the impeller, it is possible to conclude that for this study, it is possible to approximate the fluids to have a dominant viscous response. This is especially important given the fact that most CFD packages, as ANSYS Fluent, are not capable of incorporating viscoelastic fluid models.

3.2.2. Experimental setup

3.2.2.1. Design

As indicated in the introductory subsection of this chapter, the aim of this chapter is to evaluate the potential applicability of CFD to predict the fluid dynamics in mixing tanks using the particular fluids of interest. The power required to agitate fluids in mixing tanks is directly related to the flow dynamics induced by the impeller, which at the same time depend on the rheological properties of the fluids. Hence, the correct computational prediction of power requirement of mixing tanks is an indication that the flow dynamics are well captured by the CFD model, and that the rheological function is representative of the fluids used.

To minimise errors associated to modelling complex geometries, it is best to use a simple geometry, and ideally, one that has been extensively studied in the past, so bibliographical information can also be used to validate the experimental and CFD results. Hence, the 6-blade Rushton turbine was the best candidate for the case study.

The standard dimensions of a mixing tank fitted with a Rushton turbine are presented in Figure 3. 6. The typical values for J, H, D_a, E, W and L expressed as ratios of D_t are presented in Table 3. 3. By fixing only one dimension from those above, the others are automatically set. D_a was chosen as the design parameter, and it was set at 6 cm for convenience. The rest of the dimensions were automatically fixed, and they are shown in centimetres in Table 3. 4. Due to limitations in the available standard diameters of pipes (which form the main body of the tank), a final 18.8 cm internal tank diameter was chosen. The thickness of the blades and the baffles are expressed as T_b and T_f in Table 3. 4 respectively.

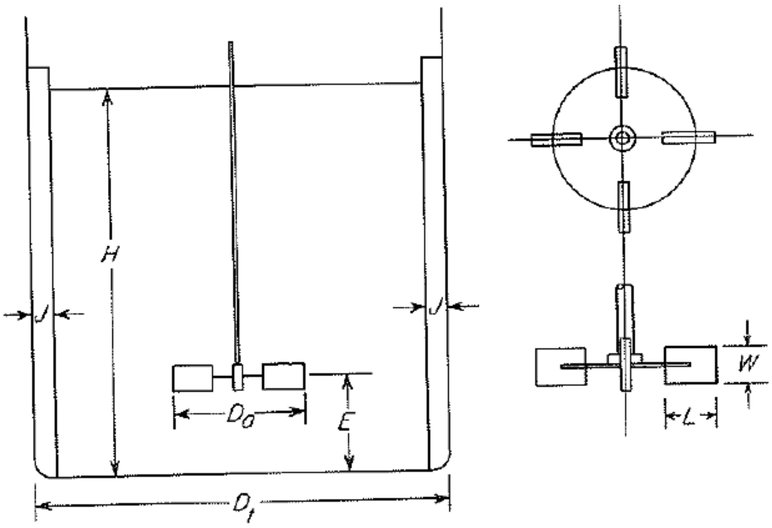

Figure 3. 6. Standard ratios of a baffled tank and Rushton turbine (Rushton et al., 1950)

Table 3. 3. Typical values for ratios of the dimensions of a baffled tank and a Rushton turbine (Rushton et al., 1950)

$\frac{D_a}{D_t}=\frac{1}{3}$	$\frac{H}{D_t}=1$	$\frac{J}{D_t}=\frac{1}{12}$
$\frac{E}{D_t}=\frac{1}{3}$	$\frac{W}{D_a}=\frac{1}{5}$	$\frac{L}{D_a}=\frac{1}{4}$

Table 3. 4. Dimensions of the tank and Rushton turbine to use in the experiments in centimetres

$D_t = 18.8$	$H = 18.8$	$J = 1.5$	$T_b = 0.25$
$E = 6$	$W = 1.2$	$L = 1.5$	$T_f = 0.5$

As reviewed in Section 2.4.1.1, different experimental techniques can be used to measure power consumption. The decision of using a combination of an air bearing together with a load cell was made for two main reasons: the higher accuracy of this combination of equipment compared to torquemeters, and the availability of an air bearing. The air bearing and the mixing tank and the impeller are shown in Figure 3.

7. Because of the high viscosity of the fluids, the baffles shown in Figure 3. 7 were not needed to maintain a flat interface.

Figure 3. 7. Mixing tank, air bearing, and Rushton turbine

In the experiments, the height of the fluid, H, was set equal to the tank diameter. The impeller was located at the centre of the tank, 5.4 cm from the bottom, and it was driven by a variable-speed motor that could operate in the range of 50 – 2000 rpm (IKA Eurostar 20).

The force required to stop the rotational plate from rotating was measured with a load cell (Omega LCM601-1) and recorded via a data acquisition system and visualised with the specific software from Omega IN-USBH. Both the load cell and the data acquisition system are shown in Figure 3. 8. To measure the force, an arm attached to the rotational plate is brought to rest on the load cell.

Figure 3. 8. Load cell and data acquisition system

The assembled setup is shown in Figure 3. 9.

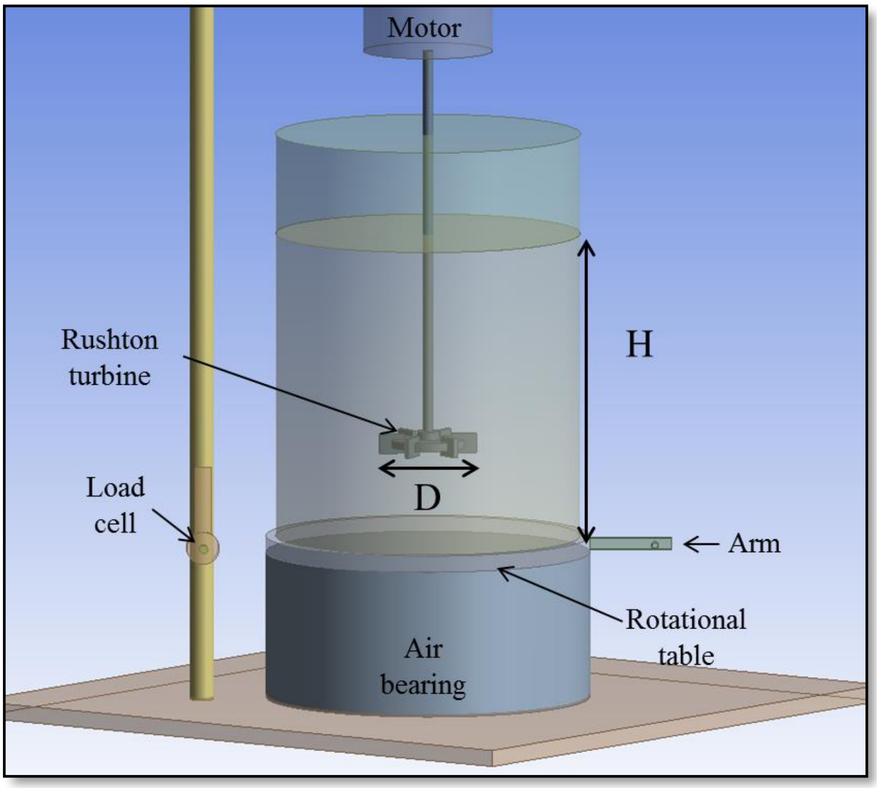

Figure 3. 9. Experimental setup

3.2.2.2. Experimental protocol

To validate the CFD simulations and provide a baseline for the non-Newtonian case, a Newtonian fluid system was initially studied. For these experiments glycerol at 20 ºC was used and stirring was carried out at five impeller speeds (between 1 rpm and 250 rpm) within the laminar flow regime. The power measurements with the non-Newtonian mixtures were carried out for two temperatures, 40 ºC and 60 ºC, gel mass fractions of 100% to 20% in intervals of 20% and a minimum of five impeller speeds.

To ensure thermal homogeneity of the system, the tank containing the sample was put in an oven with temperature control, and was left overnight to let the sample reach the required temperature. The experiments at high temperature were conducted the following day. Prior to the experiments, the temperature was measured at different points in the tank (a minimum of five), and in all cases, the maximum temperature difference in space was lower than 5 ºC.

Once an experiment at high temperature was finished, the sample was let to cool down at room temperature until it reached the required lower temperature (40 ºC). The sample was agitated with the Rushton turbine during the cooling process. When the temperature reached the required value, it was measured again at five different locations and the maximum temperature difference was also about 5 ºC.

In all measurements the tank was filled with the fluid, glycerol or gel/glycerol mixture, up to height H, the pressurised air was introduced in the air bearing and for each impeller speed the force required to stop the rotation of the rotating plate of the air bearing was measured with the load cell.

3.2.3. CFD Solution

3.2.3.1. CFD approach

In all the experiments, the free surface of the fluid remained flat, even though there were no baffles present. Therefore, to avoid using multiphase models, only the region occupied by the fluid (so, the computational domain only included this region) was simulated. This extends from the bottom of the tank up to a height equal to H (Figure 3. 9). At the top boundary, where the liquid-gas interface is, the three components of the viscous stress force referring to the unit vector normal to the interface were set equal to zero. Additionally, on all the solid surfaces bounding the computational domain, the no-slip boundary condition was applied.

The two main approaches for modelling stirred tanks are the Reference Frame (RF) and the Sliding Mesh (SM). The RF convergences fast, but it is suitable only for steady-state flows. In a stationary frame of reference (stationary relative to the laboratory) the flow in the stirred tank is unsteady. However, the flow is steady relative to a reference frame integral with the impeller, which therefore rotates with a rotational velocity – $\boldsymbol{\omega}$ relative to the stationary frame. This is a non-inertial frame, but the flow is stationary with respect to it.

In contrast, SM is suitable also for unsteady flows, for which it provides a time dependent solution, but at the expense of significant computational effort and time. In the SM approach, the geometry should have at least two connected non-deforming sections that slide with respect to each other. All the moving parts (in this case, the impeller) need to be part of the moving zone. For the present studies, I employed as moving zone a cylinder concentric with the impeller, with 10 cm diameter, bottom at 3 cm below the impeller and top at the liquid surface. The elements outside this cylinder formed the stationary zone. In this case it is not necessary to introduce a non-inertial reference frame; instead, the rotational speed ($-\boldsymbol{\omega}$) can be assigned directly to the moving objects.

RF is the preferred approach when its predictions are the same as those given by the SM approach. To decide what approach to adopt, I tested both of them in two case studies where glycerol at 27 ºC and gel at 85 ºC were stirred at 100 and 1000 rpm impeller speeds respectively. At these conditions the flow is laminar in both cases. The results of the test are presented in Section 3.2.3.3.

3.2.3.2. Rheology implementation

3.2.3.2.1. Power law model

The rheology model was implemented via a user defined function to be able to account for the errors presented in Table 3. 1. The coefficients *K* and *n* of the power law expression for the fluid viscosity were determined from the experimental rheology curves. Equations 2.5, 2.6, and 2.7 were included in the user defined function, and the rate of strain tensor was computed using the partial derivatives of the components of the velocity vector field:

$$\dot{\boldsymbol{\gamma}} = \begin{bmatrix} 2\dfrac{\partial v_x}{\partial x} & \left(\dfrac{\partial v_x}{\partial y} + \dfrac{\partial v_y}{\partial x}\right) & \left(\dfrac{\partial v_x}{\partial z} + \dfrac{\partial v_z}{\partial x}\right) \\ \left(\dfrac{\partial v_x}{\partial y} + \dfrac{\partial v_y}{\partial x}\right) & 2\dfrac{\partial v_y}{\partial y} & \left(\dfrac{\partial v_z}{\partial y} + \dfrac{\partial v_y}{\partial z}\right) \\ \left(\dfrac{\partial v_x}{\partial z} + \dfrac{\partial v_z}{\partial x}\right) & \left(\dfrac{\partial v_z}{\partial y} + \dfrac{\partial v_y}{\partial z}\right) & 2\dfrac{\partial v_z}{\partial z} \end{bmatrix} \qquad \text{(Eq. 3.5)}$$

For incompressible fluids, the trace of this tensor vanishes, so that the stress tensor $\boldsymbol{\tau}$ is deviatoric, as previously pointed out.

3.2.3.2.2. Herschel-Bulkley model

Some simulations were repeated with the Herschel-Bulkley model to check any differences between the two rheological models. For these cases, the model embedded in ANSYS Fluent in its default formulation was used. As it will be shown in Section 3.3.2.1, the power consumption predicted by the CFD model using the power law and the Herschel-Bulkley models are very similar, and therefore it was decided not to repeat all the simulations with the latter.

3.2.3.3. Grid independence

The computational solution depends not only on the modelling approach but also on the grid used in the simulation. Very fine grids give more accurate solutions but are computationally demanding. It was aimed therefore to find an optimum grid size that provides a reliable and grid-independent solution at a reasonable time for all the fluids considered in this study. To determine the optimal grid size for the geometry described in Figure 3. 9, the agitation of glycerol (Newtonian case) at 27 ºC at 100 rpm impeller speed (this results in laminar flow; the Reynolds number is approximately equal to 9.5) was simulated. Moreover, to ensure that the mesh is also optimum for the non-Newtonian case, simulations were also run for the fluid with the highest shear thinning behaviour (that of the pure gel at 85 ºC), at an impeller speed of 1000 rpm, whose corresponding Reynolds number is approximately equal to 5. The mesh quality that provided accurate solutions for both extremes was used. Grid independence was checked for both the Reference Frame and the Sliding Mesh modelling approaches (Table 3. 5 and Table 3. 6).

The SM approach with the highest mesh quality provides the most accurate torque results. Therefore, the difference from this value of the torque computed on the surface of the impeller (shown as Error with respect to high quality SM) for each case (Eq. 3.6) is also reported in Table 3. 5 and Table 3. 6.

$$\text{Error w.r.t. high quality SM [\%]} = \frac{\left|M_{impeller,SM,hq} - M_{impeller}\right|}{M_{impeller,SM,hq}} \cdot 100 \qquad \text{(Eq. 3.6)}$$

For the SM simulations, a time step equivalent to 1 degree per step was used (an entire revolution is reached after 360 steps). This allows capturing the transient behaviour of the torque, which is periodic from an inertial frame of reference. The simulation was run until a periodic solution was reached, after four complete revolutions. The results presented in Table 3. 5 and Table 3. 6 were obtained by averaging the torque on the impeller during the fifth revolution.

Table 3. 5. Comparison among the three mesh qualities studied for the different modelling approaches using the geometry in Figure 3. 9, with glycerol at 27 ºC as working fluid and an impeller speed of 100 rpm

Mesh quality [#cells]	Approach	Torque impeller [N m]	Time	Error with respect to SM high quality [%]
36,608	RF	$2.91\ 10^{-3}$	80 s	18%
54,067	RF	$2.84\ 10^{-3}$	150 s	20%
156,546	RF	$3.08\ 10^{-3}$	600 s	13%
360,371	RF	$3.49\ 10^{-3}$	25 min	1%
462,558	RF	$3.49\ 10^{-3}$	40 min	1%
31,233	SM	$3.01\ 10^{-3} \pm 5\ 10^{-6}$	100 min	15%
55,442	SM	$3.01\ 10^{-3} \pm 5\ 10^{-6}$	5 h	15%
151,164	SM	$3.16\ 10^{-3} \pm 3\ 10^{-6}$	9 h	11%
361,466	SM	$3.54\ 10^{-3} \pm 3\ 10^{-7}$	24 h	0%
527,832	SM	$3.54\ 10^{-3} \pm 3\ 10^{-7}$	36 h	0%

Table 3. 6. Comparison among the three mesh qualities studied for the different modelling approaches using the geometry in Figure 3. 9, with pure gel at 85 ºC as working fluid and an impeller speed of 1000 rpm

Mesh quality [#cells]	Approach	Torque impeller (N m)	Time	Error with respect to SM high quality [%]
36,608	RF	0.114	80 s	4%
54,067	RF	0.116	150 s	3%
156,546	RF	0.115	600 s	3%
360,371	RF	0.117	25 min	2%
462,558	RF	0.117	40 min	2%
31,233	SM	$0.119 \pm 1.4\ 10^{-4}$	100 min	0%
55,442	SM	$0.129 \pm 1.7\ 10^{-4}$	5 h	8%
151,164	SM	$0.121 \pm 2.1\ 10^{-4}$	9 h	1%
361,466	SM	$0.119 \pm 5.5\ 10^{-5}$	24 h	0%
527,832	SM	$0.119 \pm 2.8\ 10^{-5}$	36 h	0%

The results in Table 3. 5 and Table 3. 6 indicate that the RF model provides an accurate solution, particularly when the mesh quality is high for the Newtonian case (fourth and fifth rows of Table 3. 5) and in all mesh qualities studied for the non-Newtonian case (power law model). Moreover, the time required to solve this model is significantly lower compared to the SM approach (e.g. 25 min compared to 24 h for mesh quality about 360k cells). An additional way to evaluate the two approaches is to compare the torque on the surface of the impeller ($M_{impeller}$) against that on the walls of the tank (M_{walls}); at steady state the two values of the torque must be the same. Similarly, one would expect the power consumption of the impeller obtained experimentally by a torquemeter and by a combination of an air bearing with a load cell to be exactly the same. Table 3. 7 and

Table 3. 8 present the torque computed on the surface of the impeller (Eq. 2.38) and the torque difference (as in Eq. 3.7) for the different grid sizes and modelling approaches studied.

$$\text{Torque difference [\%]} = \frac{|M_{impeller} - M_{walls}|}{M_{impeller}} \cdot 100 \qquad \text{(Eq. 3.7)}$$

The torque on the walls (M_{walls}) is calculated as the axial component of $\boldsymbol{M}$ in equation 3.8:

$$\boldsymbol{M} = \int_{A_W} \mathbf{r} \times (\boldsymbol{\pi} \cdot \mathbf{n}) dA \qquad \text{(Eq. 3.8)}$$

where A_W is the surface of the tank walls including the tank bottom.

Table 3. 7. Comparison between the torques computed on the surface of the impeller and on the walls of the tank for the RF calculations using the geometry in Figure 3. 9, with glycerol at 27 ºC as working fluid and an impeller speed of 100 rpm

Quality [#cells]	Torque Impeller [N m]	Difference in torques [%]
36,608	$2.91\ 10^{-3}$	26%
54,067	$2.84\ 10^{-3}$	36%
156,546	$3.08\ 10^{-3}$	25%
360,371	$3.49\ 10^{-3}$	13%
462,558	$3.49\ 10^{-3}$	3%

Table 3. 8. Comparison between the torques computed on the surface of the impeller and on the walls of the tank for the RF calculations using the geometry in Figure 3. 9, with pure gel at 85 ºC as working fluid and an impeller speed of 1000 rpm

Quality [#cells]	Torque impeller (N m)	Error torques
36,608	0.114	4%
54,067	0.116	4%
156,546	0.115	4%
360,371	0.117	4%
462,558	0.117	4%

As it is possible to see, the difference in the torque is significant in the first four rows of Table 3. 7, and it is only with the highest quality mesh that a good agreement is obtained. In the case of the non-Newtonian fluid, this error does not depend on the mesh quality, and it is comparable to that of the highest quality mesh for the Newtonian case. It is possible to conclude that the optimal mesh quality for this particular model corresponds to the fifth row of Table 3. 7. The mesh is presented in Figure 3. 10.

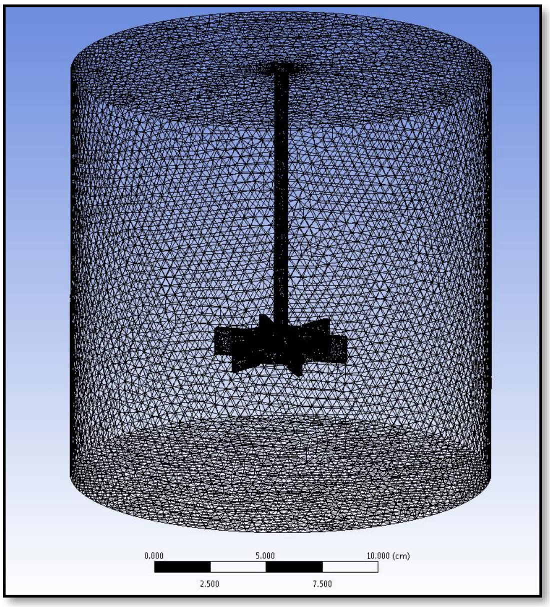

Figure 3. 10. Mesh used in the numerical simulations

The computations were carried out using a 3.50 GHz Intel® Xeon® CPU E5-1650 v2 with 16.0 GB RAM. The tank and impeller were drawn with AutoCAD. The different meshes were created with ANSYS Workbench. Unstructured meshes were preferred because of the shape of the impeller and the non-unidirectionality of the flow. The fluid dynamics were modelled using ANSYS Fluent 16.1. The solution method was set as follows: for pressure and velocity coupling, the Coupled strategy was used; in terms of spatial discretization the least squares scheme was used for evaluating the spatial derivatives, the second order interpolation scheme for the pressure, and the second order upwind scheme for the momentum. For the steady-state simulations, I let the solver run until a plateau was observed on the scaled residuals of the continuity equation, and of the x-, y- and z- velocities. The absolute scaled residuals were recorded and then used as a convergence criterion for the transient simulations.

3.3. Results and Discussion

3.3.1. Newtonian case

As discussed before, a number of experiments and CFD simulations were carried out with a Newtonian fluid to provide a baseline for the non-Newtonian study. The power number obtained experimentally for the stirring of pure glycerol at 20 ºC is plotted against the Reynolds number in Figure 3. 11.

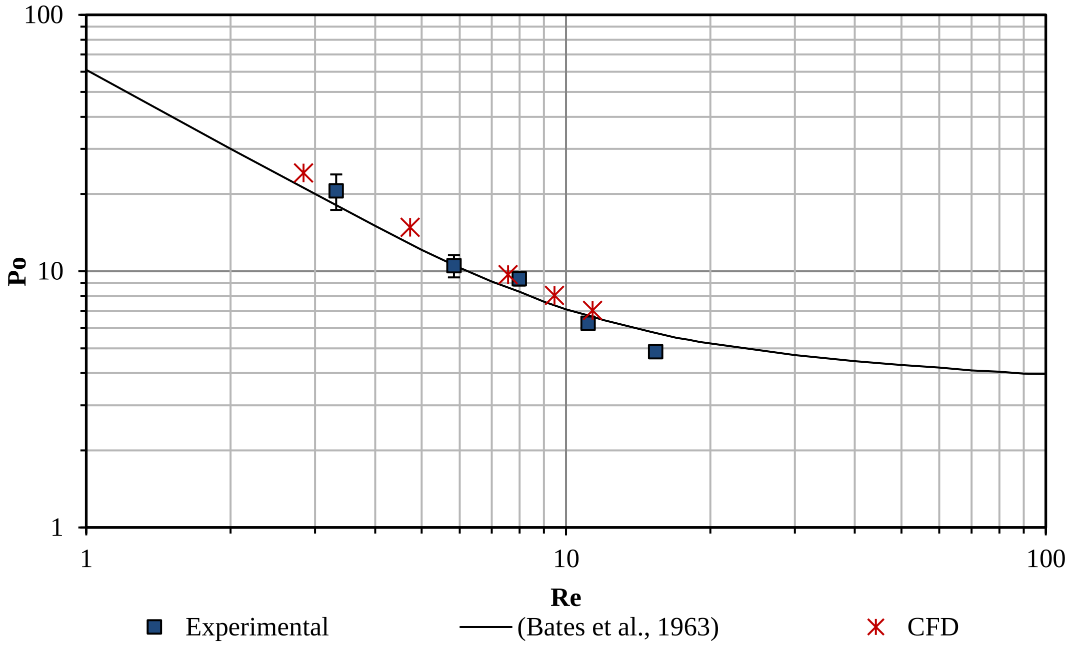

Figure 3. 11. Experimental, computational, and bibliographical power curves for Newtonian fluids agitated in an unbaffled tank equipped with a Rushton turbine for geometrically similar systems

In Figure 3. 11, the error bars account for the measurement error of the load cell, which is 0.03 % of the maximum value it can read (9.8 N). The results are in good agreement with the power curve suggested in the literature for mixing in geometrically similar systems equipped with a Rushton turbine (the error is less than 10 %).

In the same figure, the power numbers computed with CFD using pure glycerol at 20 ºC as working fluid rotating at different impeller speeds from 30 to 120 rpm, RF as modelling approach and highest mesh quality (Table 3. 5) are also shown. As it is possible to see, there is very good agreement between the experimental, computational and bibliographical sets of data.

3.3.2. Non-Newtonian case

As discussed in Section 3.2.2.2, the torque and power consumption were measured for the mixing of five non-Newtonian glycerol/gel mixtures at a minimum of five impeller speeds and at two different temperatures. As will be shown later in Section 3.3.2.1, the torque predictions using the Herschel-Bulkley model are very similar to those using the power law model. For this reason, detailed analysis was conducted only with the power law model, and this is described in the following paragraphs.

3.3.2.1. Torque predictions

In Figure 3. 12 and Figure 3. 13, the experimental torque values are plotted against the impeller speed for two different cases: 80% gel mass fraction at 60 ºC and 40% gel mass fraction at 40 ºC. These are two representative examples showing the results for a high gel mass fraction with high temperature and for a low gel mass fraction with a low temperature. Similar curves were obtained for all the other cases investigated. The errors in these experiments owing to the measuring error of the load cell (0.03% of the maximum value) are negligible, and are not shown. In the same figures, the CFD predictions using the power law (PL) and the Herschel-Bulkley (HB) models are also included.

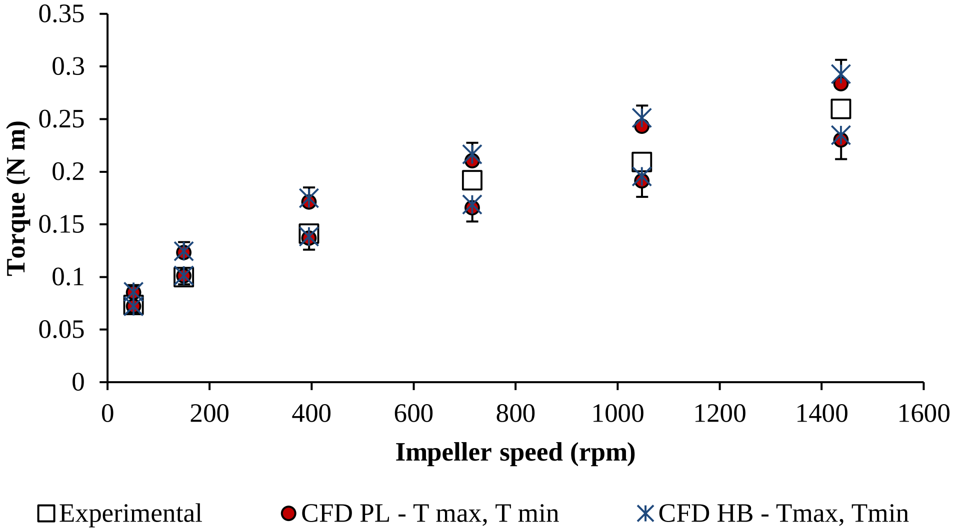

Figure 3. 12. Torque vs impeller speed for 80% gel at 60 °C

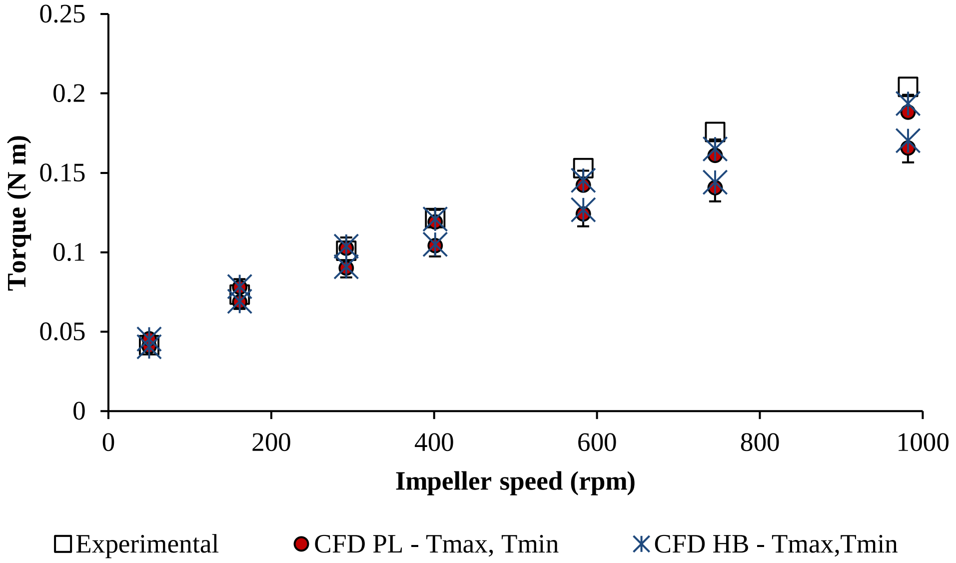

Figure 3. 13. Torque vs Impeller speed for 40% gel at 40 °C

The stirred vessel was not insulated and there were small variations in the temperature of the mixture during the experiments, both in space and time. To account for this, the temperature was measured at different points inside the mixing tank before and after the torque readings and the overall maximum and minimum temperature values recorded for the CFD simulations using both rheological models were used. Hence, two computational results for each experimental measurement are presented, which correspond to the highest and the lowest temperatures recorded.

The computational results are also subject to uncertainty that arises from the fitting of the rheological curves when determining the coefficients of the constitutive equation at the different concentrations and temperatures. Because of the similarity of the torque prediction using both rheological models, the error bars were only calculated for the power law case. These errors were presented in Table 3. 1, and they were included in the viscosity function and implemented in CFD (Eq. 3.9) to determine the size of the error bars of the computational results.

$$\eta = \left(1 \pm \frac{\text{Error}}{100}\right) K\dot{\gamma}^{n-1} \qquad \text{(Eq. 3.9)}$$

At higher temperatures the value of the viscosity is smaller, and consequently the torque is smaller as well. To calculate the lowest values of the torque expected as a result of the fitting error in the simulations with the maximum fluid temperature, the negative sign was used in Eq. 3.9. Similarly, the lowest temperature would give the highest torque values. In this case, to calculate the highest torque values expected, the positive sign in Eq. 3.9 was used. These two extreme cases were used to determine the computational error bars, which increase the torque values at the low temperature simulations and decrease them at the high temperature simulations. It is expected that the experimental torque should fall between the computational results.

In Figure 3. 12, all the experimental results fall between the two computational curves. The same happens in Figure 3. 13 for impeller speeds below 400 rpm. However, at higher impeller speeds the experimental torque values are closer to the upper CFD curve, which corresponds to the minimum experimental temperature. This difference may be caused by the actual temperature distribution inside the tank. The temperature was only measured at a few discrete points at the beginning and at the end of the experiment, and the complete temperature distribution in space and time was not available. It is possible that most of the fluid in the tank was at low temperature, and for this reason the simulated torque values for low temperatures are closer to the experimental ones.

3.3.2.2. Power curves

The power curves of the above systems are shown in Figure 3. 14 and Figure 3. 15, where the Power and Reynolds numbers were calculated from Eq. 2.32 and Eq. 2.36, respectively. The experimental error bars are negligible and have been omitted, while the error bars for the CFD simulations are shown, but are very small. As can be seen, the agreement between the computational and experimental data is very good, which indicates that the CFD model can be used to predict the torque applied by a Rushton turbine using the experimental rheology model. In addition, the slope of the experimental and computational results is very close to -1, which confirms that the flow regime is laminar in all cases. Similar results are found for the other cases considered, and they are presented in Appendix IV.

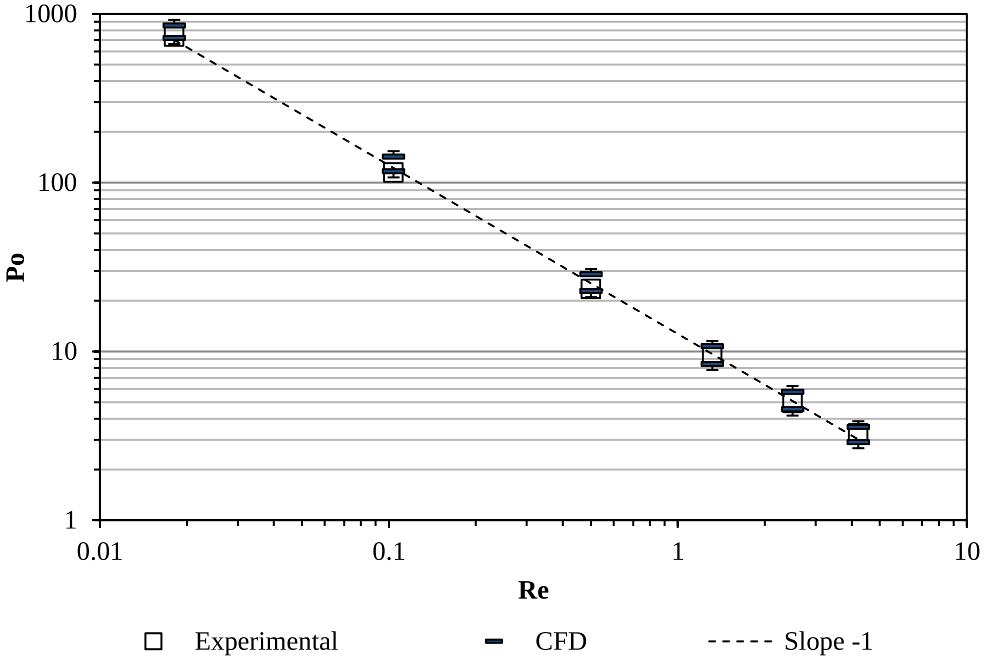

Figure 3. 14. Power curve for 80% gel mass fraction and 60 ºC

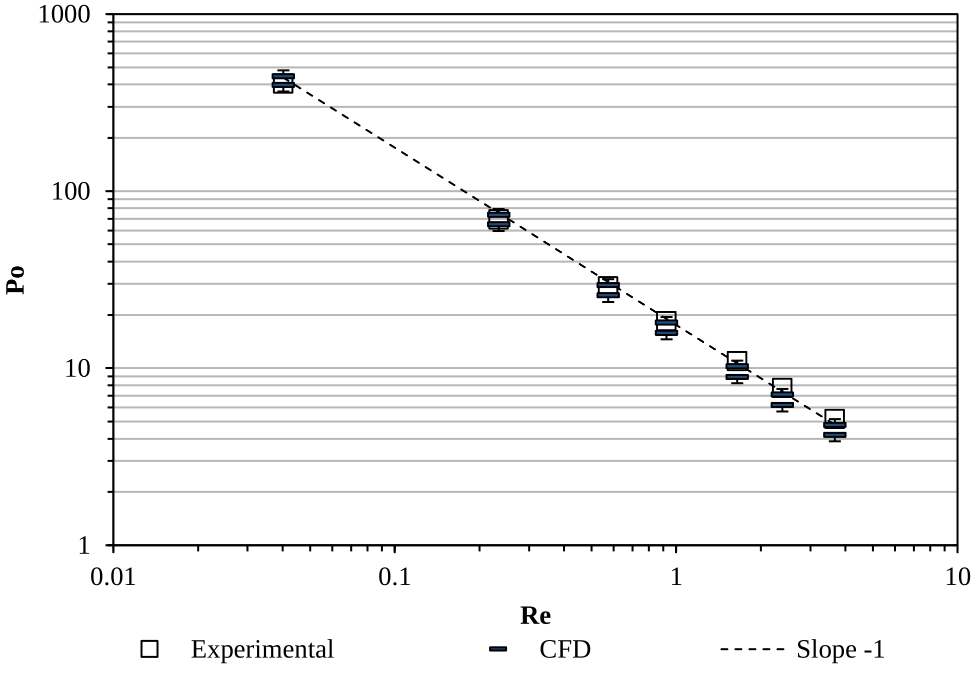

Figure 3. 15. Power curve for 40% gel mass fraction and 40 ºC

3.3.2.3. Constant of the impeller

In Eq. 2.36, the impeller constant (K_s) is needed. This value was obtained following the Metzner-Otto approach (Metzner and Otto, 1957). The impeller constant is determined as the value that makes the power curves of the Newtonian and non-Newtonian fluids overlap. The value of this constant was determined for all the cases studied, and they are shown in Table 3. 9. The final value for this coefficient is 9.65$\pm$1.01 which is in good agreement with the literature (Torrez and Andre, 1999).

In addition, the impeller constant can be used to calculate the minimum and maximum averaged shear rates on the impeller (as defined by Metzner and Otto (1957): $\dot{\gamma}_{avg} = K_s\, N$ (Eq. 2.34 bis)). As it is possible to see from Eq. 2.34, this only depends on the impeller constant and on the impeller speed. For the cases presented in Table 3. 9, the minimum and maximum average shear rate values are 8.05 and 241.36 respectively. They are both within the range of shear rates evaluated in the rheological experiments. This is of particular importance, because the power consumption of the impeller is precisely measured by the torque applied on the impeller surface.

Table 3. 9. K_s values for all the non-Newtonian power curves

Gel mass fraction [%]	T (ºC)	K_s
100	60	11.72
100	40	8.42
80	60	10.66
80	40	10.41
60	60	9.20
60	40	9.20
40	60	8.65
40	40	10.29
20	60	9.35
20	40	8.65

3.3.2.4. Viscosity and velocity profiles

The viscosity profiles and velocity vectors of the three different fluids presented above: pure glycerol at 20 ºC, gel 80% at 60 ºC, and gel 40% at 40 ºC agitated at 100 rpm (Figure 3. 16) and at 500 rpm (Figure 3. 17) on the plane that corresponds to the middle of the impeller are presented. It is possible to see that the tangential velocity next to the impeller is identical for all fluids on each figure, but the velocity vectors decay very fast in both non-Newtonian fluids compared to the Newtonian case. It can also be observed that the viscosity profiles in the non-Newtonian fluids are heterogeneous: there is an increase of viscosity in the radial direction from the impeller. These two observations are not independent, as these two facts are consequence of the shear thinning behaviour of the non-Newtonian fluids. Near the impeller, the shearing is high, which leads to a low viscosity similar to the Newtonian case and high velocity gradients exponentially magnified by the flow index behaviour (n). As the velocities are reduced fast away from the impeller, the subsequent velocity gradients can only be smaller than that immediately next to the impeller, and this reduction causes the shear rate to also be smaller than the first, leading to rapid increase of the viscosity dictated in this case by the shear thinning constitutive equation. In contrast, the sudden reduction of the viscosity near the walls is probably a numerical artefact due to the velocity gradients generated near the walls of the tank forced by the non-slip condition in the walls of the tank. It is expected that a refinement of the grid would significantly reduce the black area near the walls.

When Figure 3. 16 and Figure 3. 17 are compared, it is possible to see that in the latter the magnitude of the velocity vectors is larger, while the low viscosity area for the non-Newtonian fluids becomes greater because of the increased impeller speed.

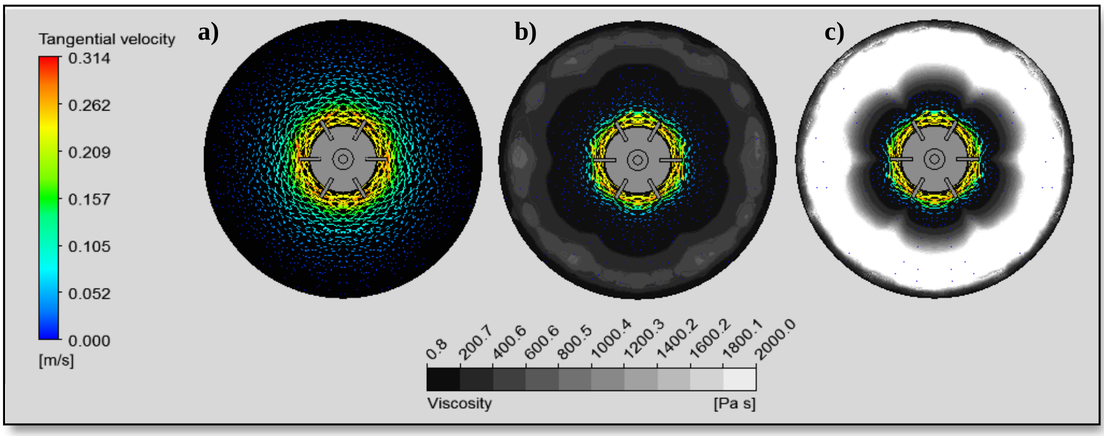

Figure 3. 16. Viscosity contours and velocity vectors for a) glycerol at 20 ºC, b) 80% gel at 60ºC, and c) 40% gel at 40ºC at 100 rpm

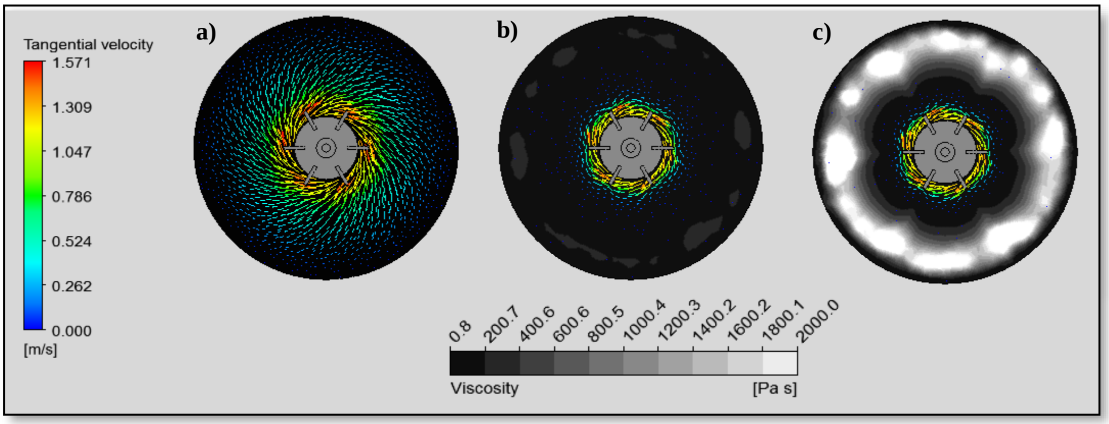

Figure 3. 17. Viscosity contours and velocity vectors for a) glycerol at 20 ºC, b) 80% gel at 60ºC, and c) 40% gel at 40ºC at 500 rpm

3.4. Conclusions

In this chapter, I evaluated the rheological properties of different mixtures of glycerol and a gel made of polyethylene glycol and carbomer, which are used in the manufacturing of non-aqueous toothpastes. The constitutive equation that relates the viscosity to the fluid temperature, gel mass fraction and shear rate was well characterised by a power law model. I then developed a CFD model of a simple stirred tank where the constitutive equation of the viscosity was implemented. The model was validated using a sophisticated experimental setup able to accurately measure the power consumption of the impeller, which involves the use of an air bearing and a load cell instead of torque meters. This preliminary study sets the ground for the modelling of the real system for the manufacturing of non-aqueous toothpastes.

4. Flow dynamics in mixing tanks

4.1. Introduction

In Chapter 3, it was shown that CFD is an adequate tool for the study of mixing tanks for the agitation of the carbomer gel and glycerol. In Chapter 4, I aim to develop a simplified scaled down version of the pilot plant mixer and implement the CFD model to study the fluid dynamics created by the mixer. Detailed validation of the CFD model is paramount to later on investigate the transient mixing of the two fluids: the carbomer gel and the glycerol. For this reason, the Particle Image Velocimetry (PIV) technique was used to validate the CFD model.

This chapter is structured as follows. In Section 4.2, the scaled-down geometry is presented first, followed by the rheological study of the non-Newtonian mixtures studied in the subsequent experiments. Additionally, the setup of the PIV experiments is presented, and the experimental protocol is detailed. In Section 4.3, the details of the CFD model are presented. In Section 4.4, various considerations for the comparison of the experimental with the numerical results are discussed. In Section 4.5, both experimental and computational velocity fields are presented and analysed, and the flow dynamics created by the agitator are studied and discussed. Finally, in Section 4.6, the conclusions are presented.

4.2. Methodology

4.2.1. Scaled-down version of the mixing system

The pilot plant scale mixer used to manufacture non-aqueous toothpastes is a coaxial impeller that consists of a central impeller and an external one (or scraper). A graphical representation can be found in Figure 4. 1.

Figure 4. 1. Representation of the pilot plant scale mixer

The mixer presented in Figure 4. 1 is rather complex, the volume of the mixing tank is close to 0.6 m^3, and it is made of stainless steel. This mixing tank cannot be used for validation purposes. Hence, I designed a laboratory scale mixer that mimics the main features of that shown in Figure 4. 1, such as long flat blades with holes on them. Complete geometrical similarity was desired, but simplifications in the laboratory-scale model were mandatory to reduce sources of uncertainty that could severely affect the validation of the CFD model.

The conical shape on the lower part of the tank was removed, as it overcomplicates the ensemble and the design of the equipment, makes the setup less robust, and it is a source of uncertainty. As this model is not intended to be a perfect small-scale version of the pilot-scale tank, it was decided not to keep constant the ratio of the area of the holes of the blades to the solid area of the impeller, mainly because of limitations imposed by the Workshop where the tank was built. In the model, the diameter of the holes was 5mm, and the ratio of the area of the holes to the solid area of the blade is 0.04.

The external impeller was substituted by two baffles. The upper and lower blades should be parallel to maintain geometric similarity, but as the baffles cannot move, the blades were offset by 90º as an attempt to account for the relative velocity between the central agitator and the scraper of the pilot-scale mixer. The ratio of the diameter of the agitator over the diameter of the tank, and the ratio of the diameter of the scraper and the diameter of the tank were maintained in the new mixer.

Additional considerations in the design were the materials; in order to be able to use PIV, optical transparency is required. Since the working fluids are glycerol and the carbomer gel (measured refractive indexes at 25 ºC of 1.4675 and 1.4645, respectively), the chosen material for the stirred tank was acrylic (1.4945). The mixing tank was enclosed in a square box. This box has two purposes: the first is to avoid optical distortions on the surface of the cylindrical vessel. To this end, the box needs to be filled with glycerol. The second purpose is to keep the temperature of the inner vessel constant. For that, I designed a recirculation system. A schematic representation of this new mixing tank with all the relevant dimensions is shown in Figure 4. 2.

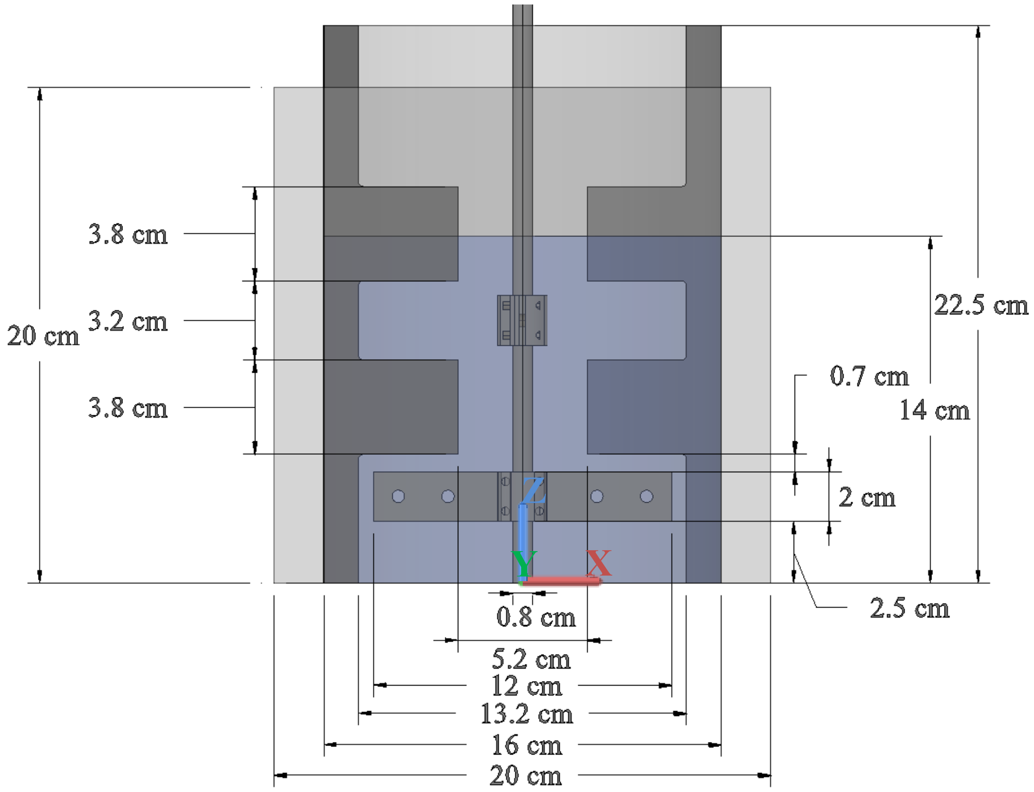

Figure 4. 2. Schematic and dimensions of the tank, impeller, baffles, and liquid height

4.2.2. Rheology characterization

The test fluids used are glycerol and a gel made of polyethylene glycol (96%) and carbomer (4%). The working fluids considered in this study are mixtures of low gel mass fractions (5% and 20% gel in glycerol by weight) at temperatures ranging from 40 ºC to 60 ºC.

In Chapter 3, both the power law and the Herschel-Bulkley models were used to characterise the viscosity of the fluids in the range of 1 – 250 s^{-1}. Nevertheless, preliminary CFD simulations indicated that the shear rate range in this case expands beyond the limits explored in Chapter 3. Hence, I decided to measure the rheological properties of these two mixtures expanding the range of measurements from 0.1 s^{-1} to 1000 s^{-1}.

For each set of conditions, the viscosity was measured at 20 equidistant points in a logarithmic scale (indicative results are shown in Figure 4. 3 and Figure 4. 4).

Within the shear rate range investigated, the error associated with the accuracy of the instrument is negligible. The measurements were carried out in an Anton Paar Physica MCR 301 rheometer with parallel plate geometry. In this configuration, the magnitude of the shear stress is evaluated at the rim of the upper plate, where both shear stress and shear rate have maximum values.

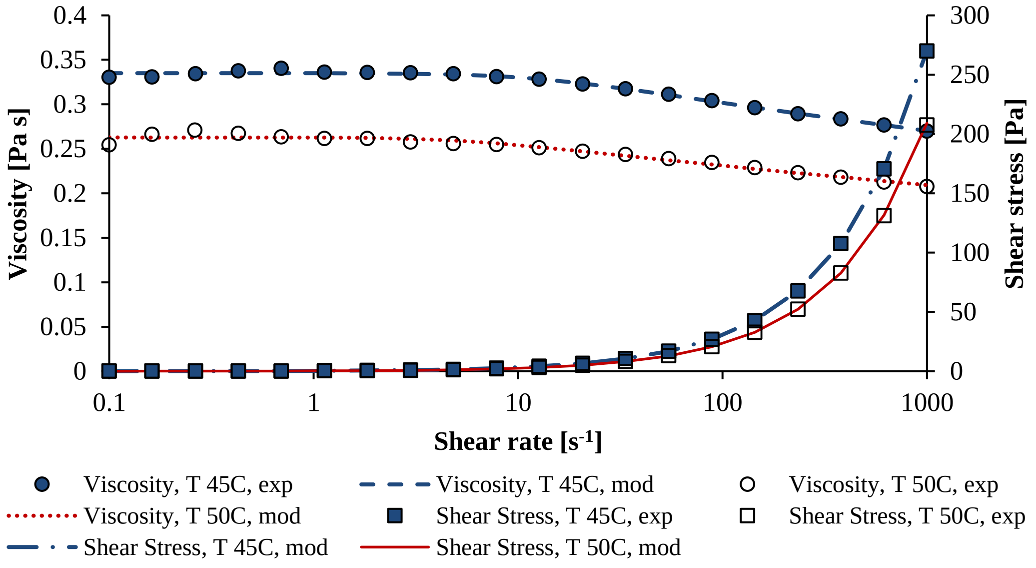

Figure 4. 3. Viscosity and shear stress as a function of the shear rate for the 5% gel mixture

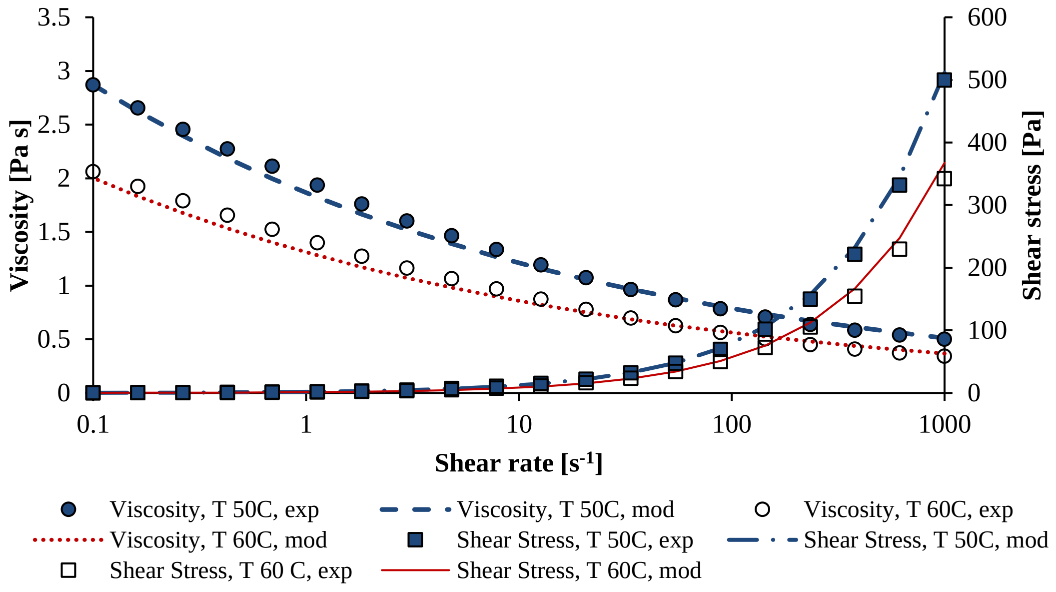

Figure 4. 4. Viscosity and shear stress as a function of the shear rate for the 20% gel mixture

One may notice that in this chapter, the working fluids are formulated with low gel mass fractions. The carbomer gel is responsible for the non-Newtonian behaviour and for the viscoelastic response of the fluids. As shown in section 3.2.1.3, mixtures with gel mass fraction below 20% have predominantly viscous response throughout the entire deformation curve. Also, as shown in Appendix III, the yield stress vanishes for mixtures below 20% gel mass fraction.

For all these reasons, the viscosity of fluids used in this chapter would be best described with the power law model as opposed to the Herschel-Bulkey model; however, as it is possible to observe in Figures 4.3 and 4.4, the viscosity plateaus on the extremes of the shear rate. Hence, the Carreau model is the best option to fit the rheological data:

$$\eta = \mu_\infty + (\mu_0 - \mu_\infty)[1 + (\lambda\dot{\gamma})^2]^{\frac{n-1}{2}} \qquad \text{(Eq. 2.8 bis)}$$

The error was computed for each individual point, and the mean error for a given composition and temperature was computed with Eq. 3.4:

$$\text{Mean error [\%]} = \frac{1}{m}\left[\sum_{i=1}^{m}\frac{\left|x_{i,\exp} - x_{i,m}\right|}{x_{i,\exp}}\right]\cdot 100 \qquad \text{(Eq. 3.4 bis)}$$

The coefficients of the Carreau model together with the modelling error in the Carreau fitting for the experimental conditions studied can be found in Table 4. 1 and Table 4. 2.

Table 4. 1. Parameters of the Carreau model and average error in the fitting for the 5% gel mixture

T [ºC]	λ [s]	n [ ]	μ_0 [Pa s]	μ_∞ [Pa s]	Error [%]
40	0.6000	0.9552	0.4767	0.0	1.81%
45	0.0876	0.9520	0.3350	0.0	0.41%
50	0.1930	0.9567	0.2628	0.0	0.92%
55	0.4179	0.9593	0.2120	0.0	1.78%
60	0.3109	0.9552	0.1707	0.0	2.56%

Table 4. 2. Parameters of the Carreau model and average error in the fitting for the 20% gel mixture

T [ºC]	λ [s]	n [ ]	μ_0 [Pa s]	μ_∞ [Pa s]	Error [%]
40	100	0.8208	6.253	0.0001	2.86%
45	100	0.8147	5.304	0.0001	3.33%
50	100	0.8126	4.423	0.0001	3.83%
55	100	0.7987	4.239	0.0001	2.32%
60	100	0.8158	3.063	0.0001	6.47%

4.2.3. PIV setup

Velocity measurements were carried out using Particle Image Velocimetry. The PIV set-up includes a dual cavity Nd:Yag green laser (532 nm) (Litron Laser®, 15 Hz, 1200 mJ) and a straddling CCD camera with 2048 x 2048 pixels (TSI PowerView™ Plus) and a maximum frequency of 16 frames per second, equipped with an AF Nikkor 50mm f/1.8D prime lens (Nikon®).

A hall switch sensor was used to capture images at the same phase angle. Fluorescent polymer particles (melamine resin based) coated with rhodamine B (20-50 µm) were used as tracer, which absorb in the green laser light. They are neutrally buoyant in the fluids considered, and, at the experimental conditions explored, their relaxation time is negligible compared to the convection time (St<<1). To ensure that only the emitted light from the particles (maximum emission at 590 nm) was recorded by the camera, an orange filter with a cut-on wavelength at 570 nm was used.

The laser and the camera were synchronized by means of a Laser Pulse Synchroniser (Model 610035 TSI) and they were controlled via the Insight 4G (TSI) software. The laser beam was passed through a collimator (Model 610026 TSI) and two cylindrical lenses (25 mm, and 15 mm) to transform it into a narrow plane of 1 mm thickness. The generated laser plane was reflected on a 45º silver coated mirror and entered the stirred vessel from the bottom.

To maximize the visualization area, I captured the velocity profiles on a vertical central plane of the tank, when the top blades of the impeller were parallel to that plane. A sketch of the setup is shown in Figure 4. 5.

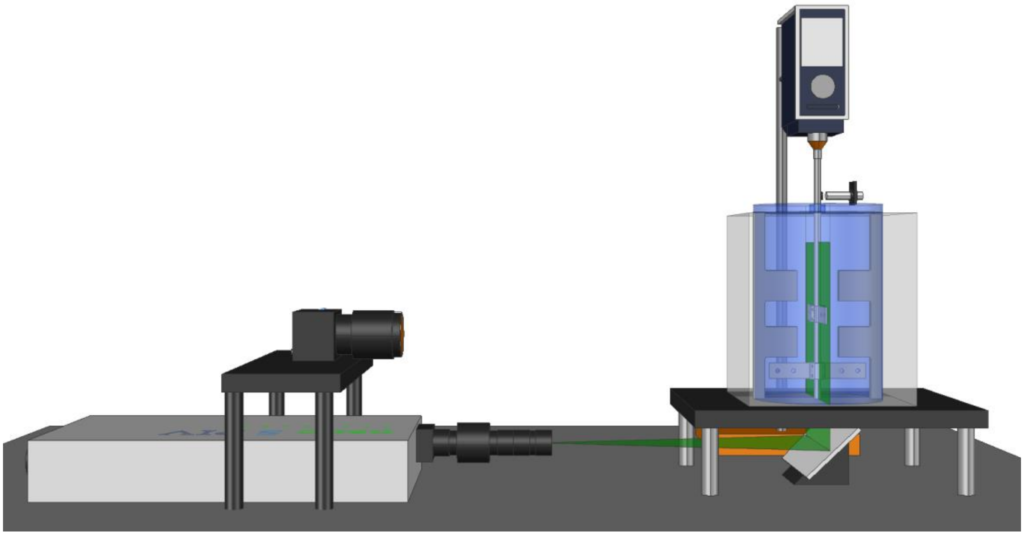

Figure 4. 5. Sketch of the main components of the experimental set-up for the PIV measurements

In a typical experiment, I first filled the outer acrylic box with glycerol at the required temperature. The test mixture at the required concentration was pre-heated at the same temperature as the glycerol present in the outer box and then loaded in the stirred vessel. Subsequently, I started the impeller at 100 rpm and added the Rhodamine particles. I recorded ten images, to ensure that the tracer concentration was sufficient (about 4 to 6 particles per PIV correlation box). I then set the impeller at the required speed for the given experiment and captured the PIV images. The averaged velocity profile converged after 100 image pairs and for the results shown here I averaged about 200 image pairs to minimize statistical errors.

Raw images needed to be treated before obtaining the velocity profiles. Images were processed in a greyscale, where zero is the equivalent of black, while the maximum value of the scale (in this case 255) corresponds to white. First, the impeller was masked, and then the images were cropped at the edges of the tank and at the top of the fluid. The noise was reduced by setting a threshold below which the values of the pixels are set to zero (the colour is set to black). Then the intensity of the images was re-scaled to obtain sharper tracer images. The pre-processing was carried out in MATLAB. The images were then further processed with the freeware package JPIV. A 50% window overlap was used for a final resolution of 16x16 pixels, corresponding to an area of 1.6 x 1.6 mm^2. The spurious vectors were removed and an amplitude filter was applied to each cross-correlation box to eliminate the vectors that substantially deviate from the median value (smoothing) (Westerweel and Scarano, 2005). Then, on each cross-correlation box, I calculated the average and the standard deviation over the total number of images. For the case shown in Figure 4. 6, for a gel concentration of 5%, the total uncertainty in calculating the velocity vector was 0.0006 m/s, which is the equivalent of 1.5% for high velocity regions.

The PIV errors were estimated using the bias limit formula (Moffat, 1988). After considering all the potential sources of error: (i) tracer dynamics, (ii) image mapping, (iii) resolution, (iv) vector placement, (v) interrogation, and (vi) sampling error (Adrian and Westerweel, 2011), it was concluded that both the sampling and the interrogation errors were relevant to the PIV study. Figure 4. 6 shows the average PIV velocities and estimated error in all the cross-correlation boxes across the Z direction at a given Y position.

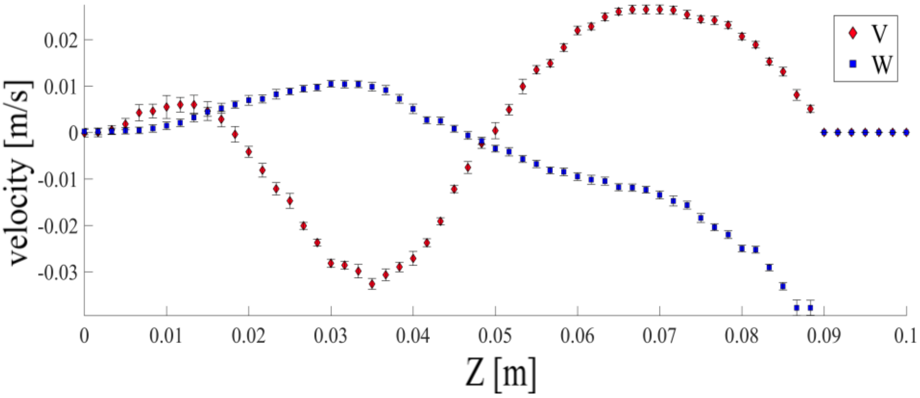

Figure 4. 6. Experimental profiles of the y- and z- velocity components (V and W respectively) with error bars along the Z-direction for Y = -0.053 m, and X = 0 m, for 5% gel and 40 rpm

4.3. CFD modelling strategy

As shown in Figure 4. 2, the height of the fluid in the vessel was set at 14 cm. This is 2.3 cm above the highest blade. Because of the baffles, the interface remained flat in all the experiments. To avoid using multiphase models, only the region occupied by the fluid was simulated, which extends from the bottom of the tank up to a height equal to 14 cm. At the top boundary, where the liquid-gas interface lies, the components of the viscous stress force referring to the unit vector normal to the interface were set equal to zero. Additionally, on all the solid surfaces bounding the computational domain, the no-slip boundary condition was applied.

Due to the small distance between the impeller and the walls of the tank and the baffles, the only appropriate modelling approach is the Sliding Mesh (SM). The Reference Frame approach can only be used to initialize the fluid motion. In the SM approach, the geometry should have at least two connected non-deforming zones that slide with respect to each other. All the moving parts (in this case, the impeller) need to be part of the moving zone. I employed as moving zone the union of three cylinders, one enclosing the shaft of the impeller and two enclosing the blades. These three cylinders are merged as a single rotating zone. The cylinder enclosing the shaft has a diameter of 2 cm. The boundaries of the cylinders surrounding the top and bottom blades were defined at the midpoint between the tip of the blades and the edge of the baffles. The elements outside these cylinders formed the stationary zone. A graphical representation of this can be seen in Figure 4. 7, where the yellow and the blue correspond to the moving and to the stationary zones respectively.

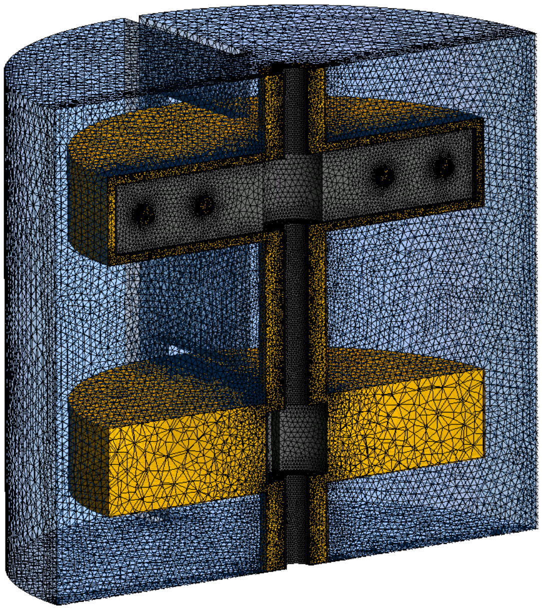

Figure 4. 7. Schematics of the moving (yellow) and stationary (blue) zones. The final grid can also be seen.

The computations were carried out in ten parallel processors using a 3.10 GHz Intel® Xeon® CPU E5-2687W v3 with 192.0 GB RAM. The tank and impeller were drawn with AutoCAD. The different meshes were created with ANSYS Workbench. Unstructured meshes were preferred because of the shape of the impeller. The fluid dynamic model was solved using ANSYS Fluent 16.1. Different numerical schemes were tested and those that provided the fastest convergence of the simulations were selected. The solution methodology was set as follows: for pressure and velocity coupling, the Coupled strategy was used; for spatial discretization I used the least squares scheme to evaluate the spatial derivatives, the second order interpolation scheme for the pressure, and the second order upwind scheme for the momentum. For the steady-state simulations (initialization only), I let the solver run until a plateau was observed on the scaled residuals of the continuity equation and of the three velocity components. For transient simulations, I set 1° of impeller rotation per time step; the time step depends on the rotational speed assigned to the impeller, so that 360 time steps were equivalent to a revolution in all cases. The simulation has converged when the values of the residuals reach a plateau, as in the steady-state simulations.

4.3.1. Grid independence

The computational solution depends on the grid used in the simulation, if the grid is not fine enough; very fine grids, however, are computationally more demanding than coarser ones. So, before running the simulations, I attempted to determine a grid size that provides an acceptable trade-off between grid independence and computational cost. Simulations were carried out using four different grid sizes for a mixture with 5% gel at 49 ºC and 40 rpm impeller speed. The solutions for the four different mesh qualities were compared by plotting the velocity profiles along the positive part of the y axis at different heights in the tank (z_1 = 3 cm and z_2 = 8 cm) on the central plane (x = 0 cm) where the top impeller blades are parallel to the plane (and consequently, perpendicular to the baffles and the lower blades). The details of the simulations are summarised in Table 4. 3.

Table 4. 3. Summary of the meshes studied, number of cells and simulation time per mesh size

Mesh	# cells	Simulation time [days]
Bad quality (BQ)	36,000	<1
Low quality (LQ)	750,000	1.5
Medium quality (MQ)	1,600,000	3
High quality (HQ)	2,900,000	6

As can be seen in Figure 4. 8, the BQ and LQ meshes are not fine enough. The MQ and HQ provide almost identical results in all profiles presented in Figure 4. 8; this indicates that the solution has become nearly grid-independent. The MQ mesh was chosen because of the more time efficient performance. Simulations with the same four grids were repeated using the 20% gel mixture rotating at 140 rpm, and the same conclusions were drawn.

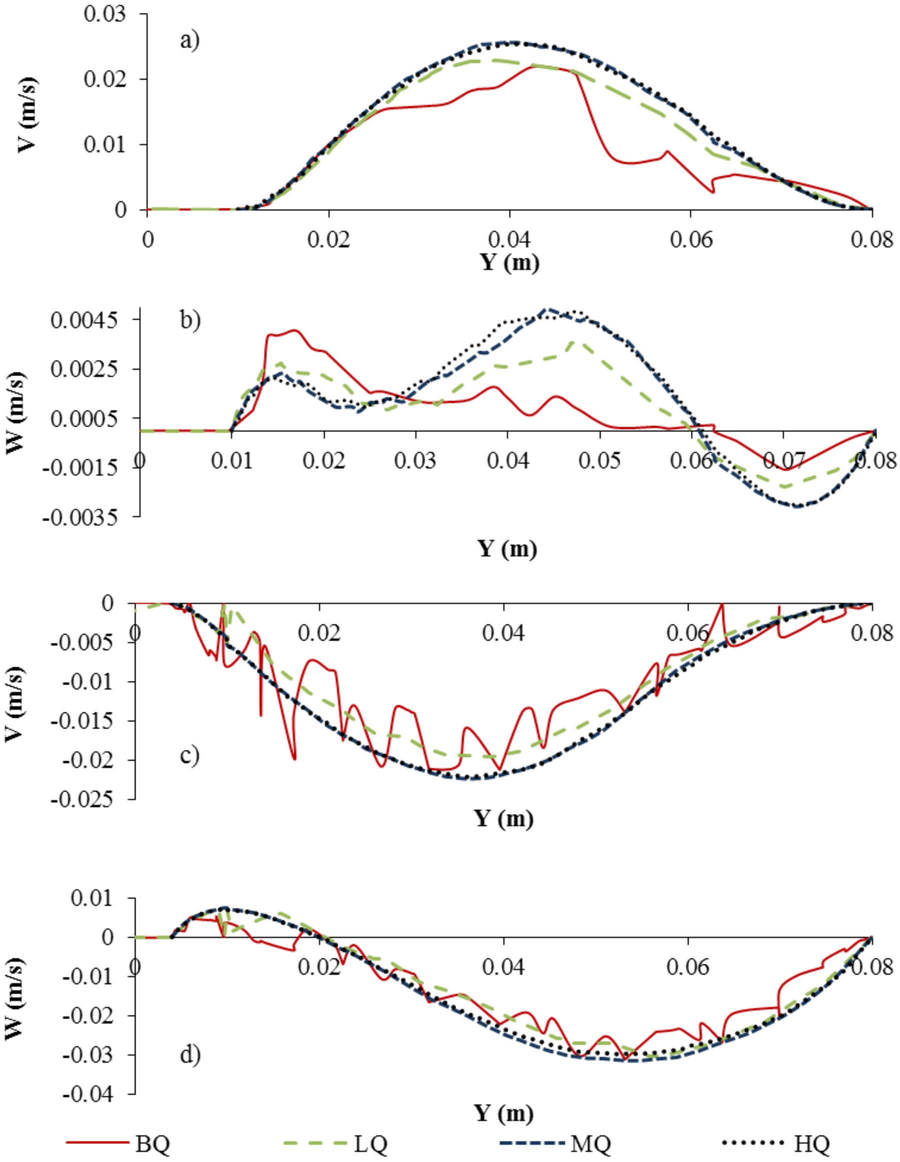

Figure 4. 8. Profiles of the y- and z- velocity components (V and W respectively) along the positive Y direction at X = 0 at two different heights: a) and b) Z = 3cm, and c) and d) Z = 8 cm

4.3.2. Post-processing

The mesh used in the CFD model is unstructured. In contrast, the PIV results are obtained in a structured grid defined by the cross-correlation box size. Consequently, the number and position of the CFD cells along the central plane of the vessel are different to those of the cross-correlation boxes of the PIV. To enable direct comparison, the PIV grid was adopted. The CFD results were modified by averaging the velocity values in the CFD cells occupying the space of a single PIV cross-correlation box. The procedure was carried out in MATLAB using the functions “meshgrid” and “griddata” with the “natural” interpolation scheme. An example is shown in Figure 4. 9 and Figure 4. 10 for the case of gel 5% at 49 ºC rotating at 40 rpm.

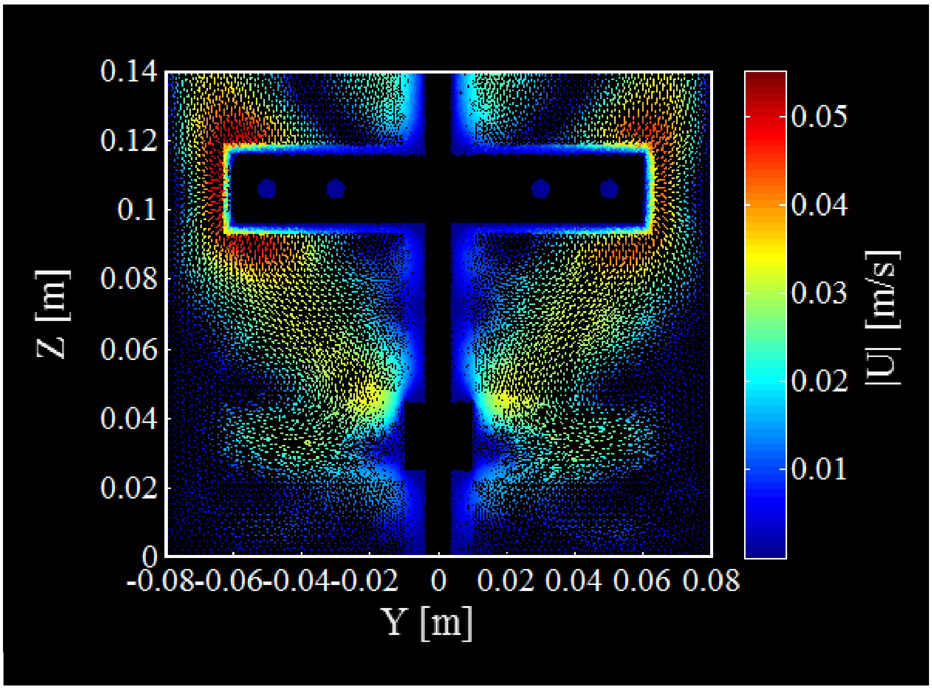

Figure 4. 9. Transformation of velocity results from the CFD to the PIV grid - Velocities from the CFD simulations

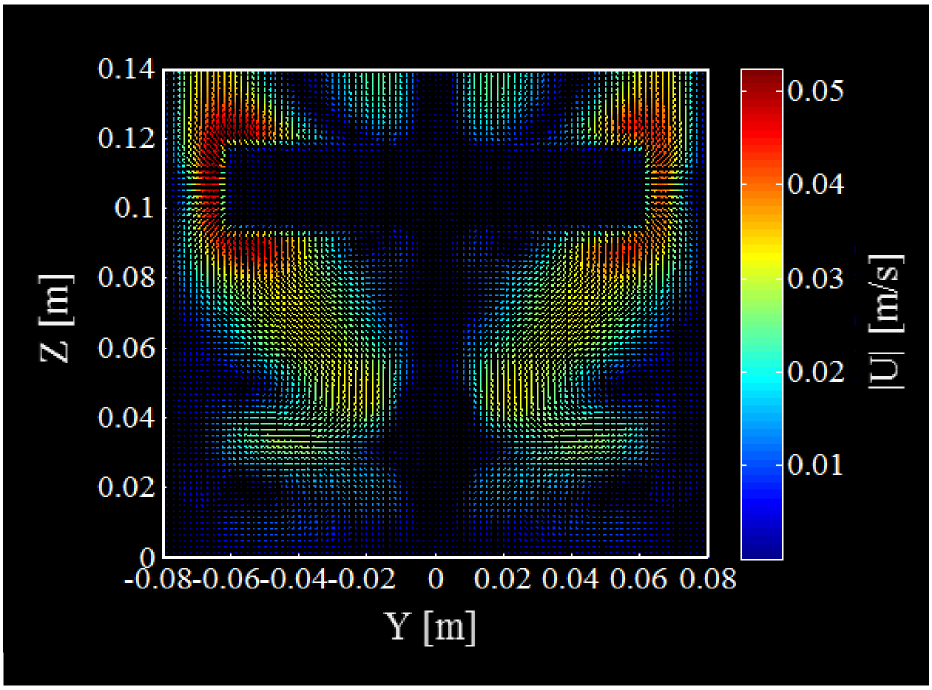

Figure 4. 10. Transformation of velocity results from the CFD to the PIV grid - Velocities translated into the PIV grid

4.4. Quantification of uncertainty between simulations and experiments

A number of considerations should be taken into account when comparing the CFD simulations and the experimental data from the PIV measurements. These are discussed below.

(i) Plane of measurement

With CFD it is possible to extract velocity data at any plane in the stirred vessel. However, in the PIV measurements, velocity is calculated from the displacement of particles over a certain (very short) time interval. Over this time interval, the impeller blades move. Consequently, to compare velocities between CFD and PIV, one needs to average the data from CFD over the region corresponding to the small displacement of the impeller during the PIV measurements. For example, for the velocities in the central vertical plane of the vessel that is parallel to the top blades and perpendicular to the lower blades and the baffles (coordinates: $x = 0$, $y = [-0.08, 0.08]$ m, $z = [0, 0.14]$ m), the PIV image pairs are over two planes, one just in front and one just behind the blade (see Figure 4. 11). The velocities from the CFD simulations need to be averaged over the region bounded by these two planes.

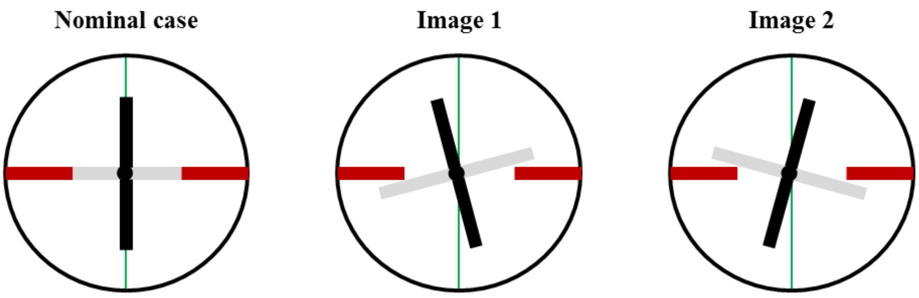

Figure 4. 11. Nominal case and position of impeller on PIV images (clockwise impeller rotation)

(ii) **Plane misalignment**

The laser was aligned by drawing two marks at two diametrically opposite points at the top of the tank, where the light should pass through (points A and B in Figure 4. 12). These are thin marks with 5 mm thickness; so, the uncertainty in the position of the laser plane is ±2.5 mm on both extremes. An exaggerated representation of this is shown in Figure 4. 12 P2 and P3. Also, the ideal plane alignment is shown in Figure 4. 12 P1. In Figure 4. 12, the mixing tank is shown from above, the laser plane is plotted in green, the baffles are plotted in red, the top impeller is plotted in black, and the lower impeller is plotted in grey**.** The CFD results are extracted on the three planes, the velocity profile on P1 corresponds to the nominal case, and P2 and P3 are used to obtain a range of uncertainty for the CFD results. The PIV results are expected to fall within this range of uncertainty.

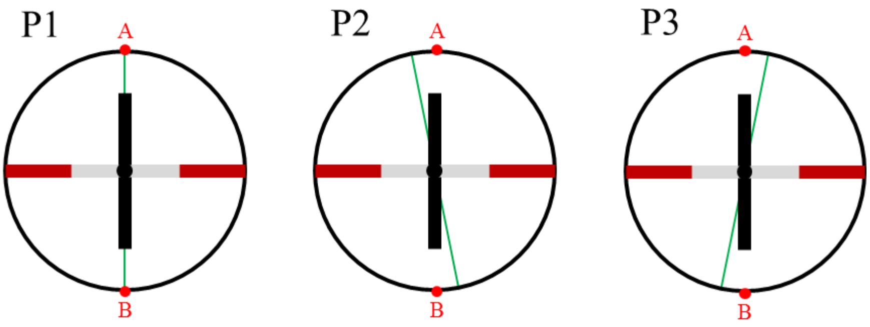

Figure 4. 12. Top view of the mixing tank and the effect of uncertainty in laser alignment

(iii) **Synchronization of the switch hall sensor**

A switch hall sensor was used to synchronize the laser pulses with the impeller rotation in the vessel and acquire images always at the same phase angle. I attached a magnet to the impeller, which triggers the laser and the camera when it is close enough to the sensor. Knowing the rotational speed of the impeller, and the Δt between the laser pulses, it is possible to calculate the phase angle difference between the two PIV images in a pair. For the case of 5% gel at 49 ºC and an impeller rotating speed of 40 rpm, the Δt was 15 ms, which translates into a phase angle difference of 3º. The ideal scenario was presented in Figure 4. 11. Mispositioning the magnet changes the phase angle at which the images are captured. Exaggerated scenarios with prompt and delayed image acquisition are presented in Figure 4. 13. Based on our PIV results, the images acquired had a slight delay. The maximum delay observed in the images corresponds to that of the first image capturing the impeller on the centre of the plane (this is pictured in Image 1 in the “Delayed images scenario” presented in Figure 4. 13). In other words, the delay in the images is half of the phase angle difference between the PIV images. Consequently, the CFD results were not only extracted for the nominal case, but also for the impeller positions corresponding to the delayed images, and they were included in the uncertainty on the CFD results.

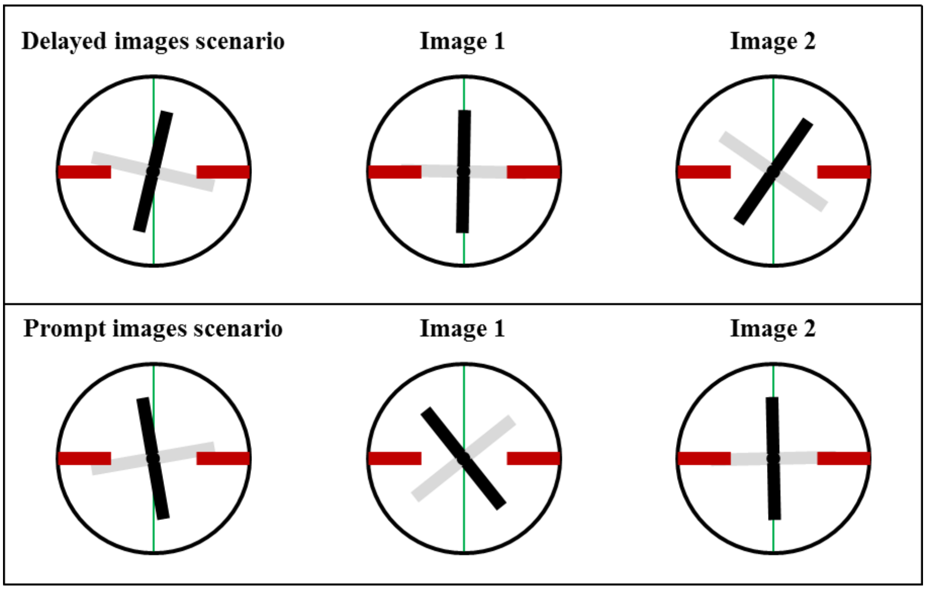

Figure 4. 13. Scenarios of mispositioning the sensor with clockwise impeller rotation

(iv) **Temperature**

There were small variations of the temperature within the stirred vessel. For each set of conditions, I measured the temperature with a thermocouple throughout the experiment, and in the simulations I used both the highest and the lowest temperatures.

The above uncertainties do not appear in isolation. Although they are experimental uncertainties, they cannot be accounted for as experimental error bars. I present the CFD results that correspond to the nominal PIV case as if the experiment was ideal, and I ascribe a range of uncertainty to the CFD results that corresponds to the maximum and minimum velocity values calculated considering all the sources of experimental uncertainty. In total, there are eighteen possible combinations of uncertainties accounting for the plane of measurement, plane misalignment, synchronization of the switch hall sensor, and temperature (excluding the nominal case) per experiment. For each experiment, I obtained the CFD results for all these combinations, and I translated the results into the PIV grid as explained in Section 4.3.2. Finally, I kept the maximum and minimum velocities of all the combinations in each position of the PIV grid. These denote the uncertainty in the CFD results owing to the imperfection in the experimental conditions. I consider that there is good agreement between simulations and experiments when the experimental velocities fall within the range of the uncertainty considered for the CFD simulations.

4.5. Results and discussion

4.5.1. Comparison of computational and experimental results

I studied the fluid dynamics in the stirred vessel for two different mixtures, gel 5%/glycerol 95% and gel 20%/glycerol 80%, for the impeller speeds reported in Table 4. 4. The second mixture has a stronger non-Newtonian behaviour than the first, as shown in Section 4.2.2. Table 4. 4 also reports the initial and final experimental temperatures (Ti and Te, respectively) as well as the time difference between the two PIV frames, the speed of the tip of the blades and the value of the Reynolds number defined in Eq. 4.1 and calculated by means of the Metzner and Otto approach (Metzner and Otto, 1957) (calculated constant of the impeller k = 15).

$$\mathrm{Re} = \frac{\rho D^2 N}{\mu_\infty + (\mu_0 - \mu_\infty)[1 + (\lambda k N)^2]^{\frac{n-1}{2}}} \qquad \text{(Eq. 4.1)}$$

Table 4. 4. List of experimental conditions

Gel mas fraction [%]	N [rpm]	Ti [ºC]	Te [ºC]	T avg [ºC]	Δt [ms]	Tip speed [m/s]	Re [ ]
5	40	50	48	49	15	0.25	38
5	120	48	46	47	6	0.75	120
20	80	60	58	59	12	0.50	23
20	140	52	51	51.5	6	0.88	44

In Figure 4. 14, the velocity profiles obtained experimentally and computationally on the YZ plane for the first case in Table 4. 4 were compared. The left-hand side corresponds to the experimental results, and the right-hand side to the computational results corresponding to the nominal case presented in Figure 4. 12 P1.

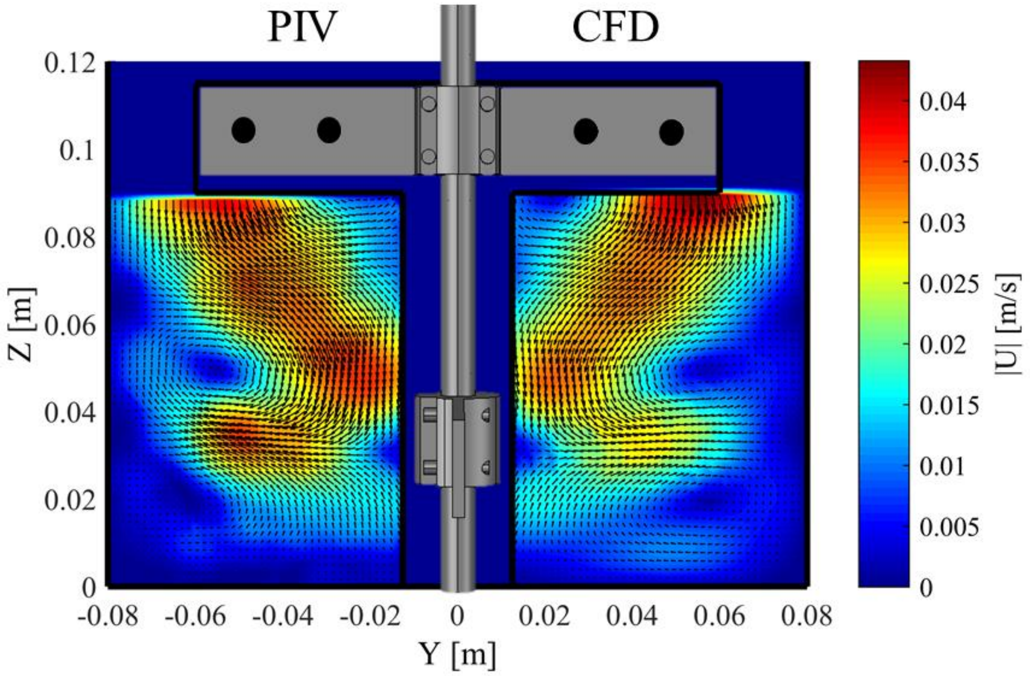

Figure 4. 14. PIV vs CFD velocity profiles on the plane X = 0 using the y- and z-velocity components for 5% gel and 40rpm

As can be seen, the CFD is able to capture the main features of the flow; these include high axial downward velocities below the top blade and above the lower blade, and dominant radial velocities at the level of the lower blade. The CFD also predicts the location and magnitude of the vortex formed between the heights of 0.04 and 0.06 m, and the location of the quasi-stagnant zones near the lateral walls and the bottom of the tank.

For a more detailed comparison, I selected two different Y positions in the tank (for X = 0), and I plotted the y and z velocity components (denoted as V and W) from both experiments and simulations along the Z direction in Figure 4. 15. In addition, the estimated error bars for the PIV results were included, and I accounted for the uncertainties in the comparison between experimental and computational results as explained in Section 4.4.

It can be seen in Figure 4. 15 that the computational and experimental values have similar trends. Some experimental points fall outside the CFD range, even when all the uncertainties are accounted for. However, in most cases, the deviation is small. It is important to notice that, in most of the profile, the uncertainties introduced by experimental imperfections, represented by black crosses, are small, and it is mainly near the blades (from 8 cm to 9 cm and from 2.5 to 4.5 cm) that these are significantly magnified. One could expect this, since the fluid is highly viscous.

The highest velocities and the sharpest velocity gradients are localized near the moving objects; hence, small variations in the position of the blades and the recording plane have a significant impact on the local velocity vectors (as can be seen in Figure 4. 15 a) to d)). In both cases presented in Figure 4. 15, the uncertainty of the z velocity component is largest near the top blade. It is also in these regions that the CFD under-predicts the values of the velocity components. The greatest experimental error bars relative to the velocity are found in zones with low velocity; this is near the walls and bottom of the tank. This is probably caused by the difficulty in capturing these velocity vectors due to loss of correlation of the PIV images (when the displacement of the tracer particles is smaller than 0.1 pixels in a pair of PIV images). This is particularly evident in Figure 4. 15 c), where one should trust the CFD predictions more than the experimental results near the bottom of the tank.

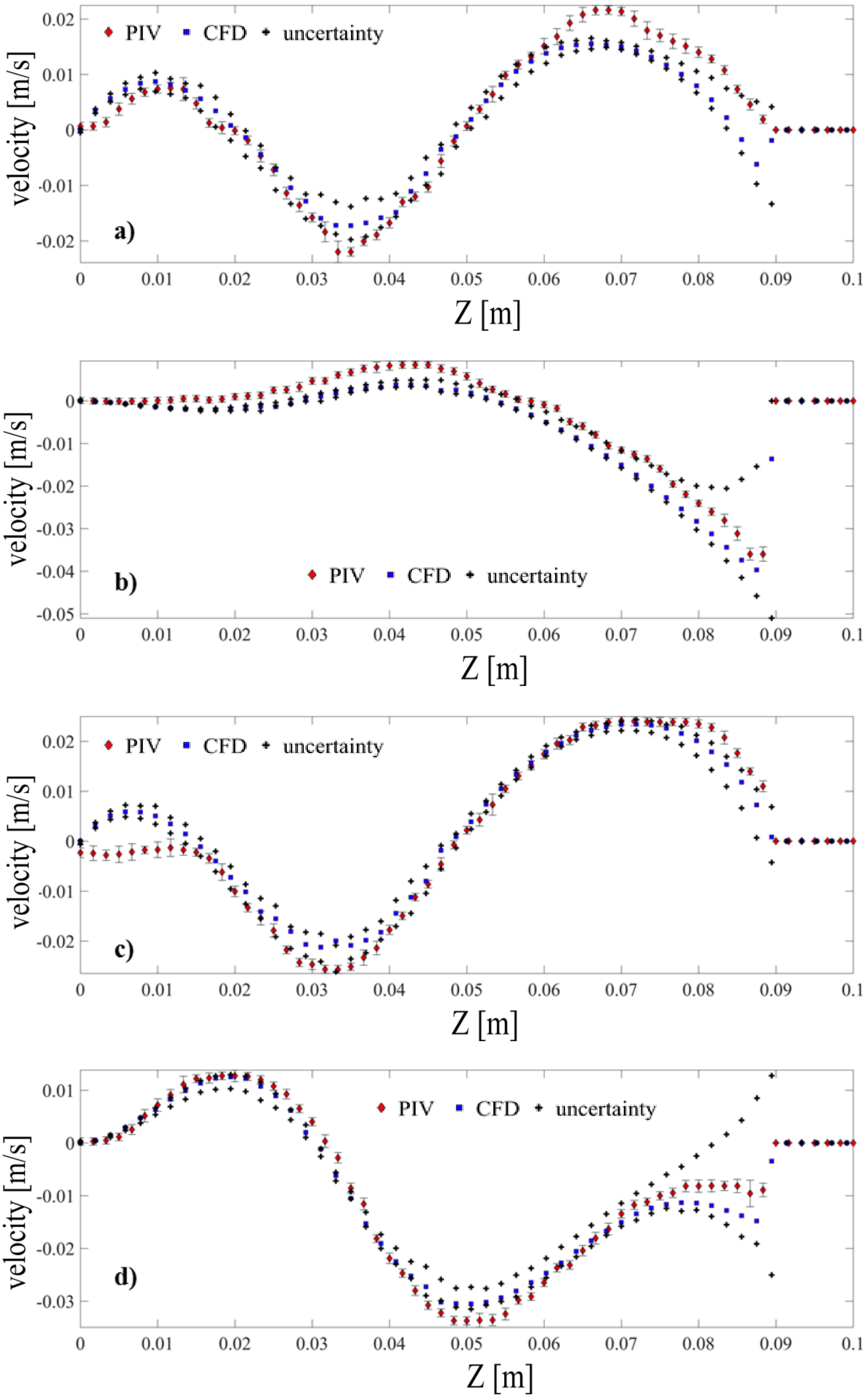

Figure 4. 15. Velocity profiles of V [a) and c)] and W [b) and d)] at two different Y positions [6 cm in a) and b), and 3 cm in c) and d)] for 5% gel and 40rpm

The same comparisons are also done for the 20% gel mixture for impeller speed 140 rpm, which has a similar value of the Reynolds number. The velocity profiles from both PIV and CFD are shown in Figure 4. 16, while the V and W velocities along Z are shown in Figure 4. 17 for two Y positions.

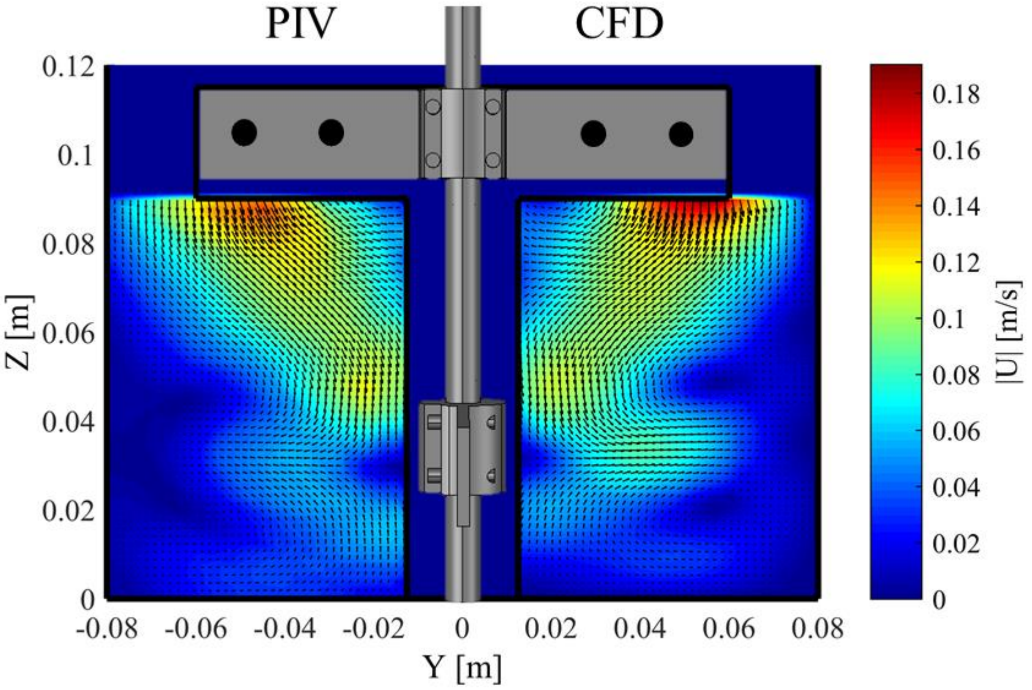

Figure 4. 16. PIV vs CFD velocity profiles on the plane X = 0 using the y- and z-velocity components for 20% gel and 140 rpm

From Figure 4. 16 one can see that there is overall good agreement between the experimental and numerical velocity profiles. The flow has similar characteristics to the previous case, with strong downward velocities near the top blades and above the lower blades, and high radial velocities near the lower blade. In this case, however, vortices between the heights of 0.04 and 0.06 m are not formed; instead, the low velocity zones are larger in this case, and they occupy that space.

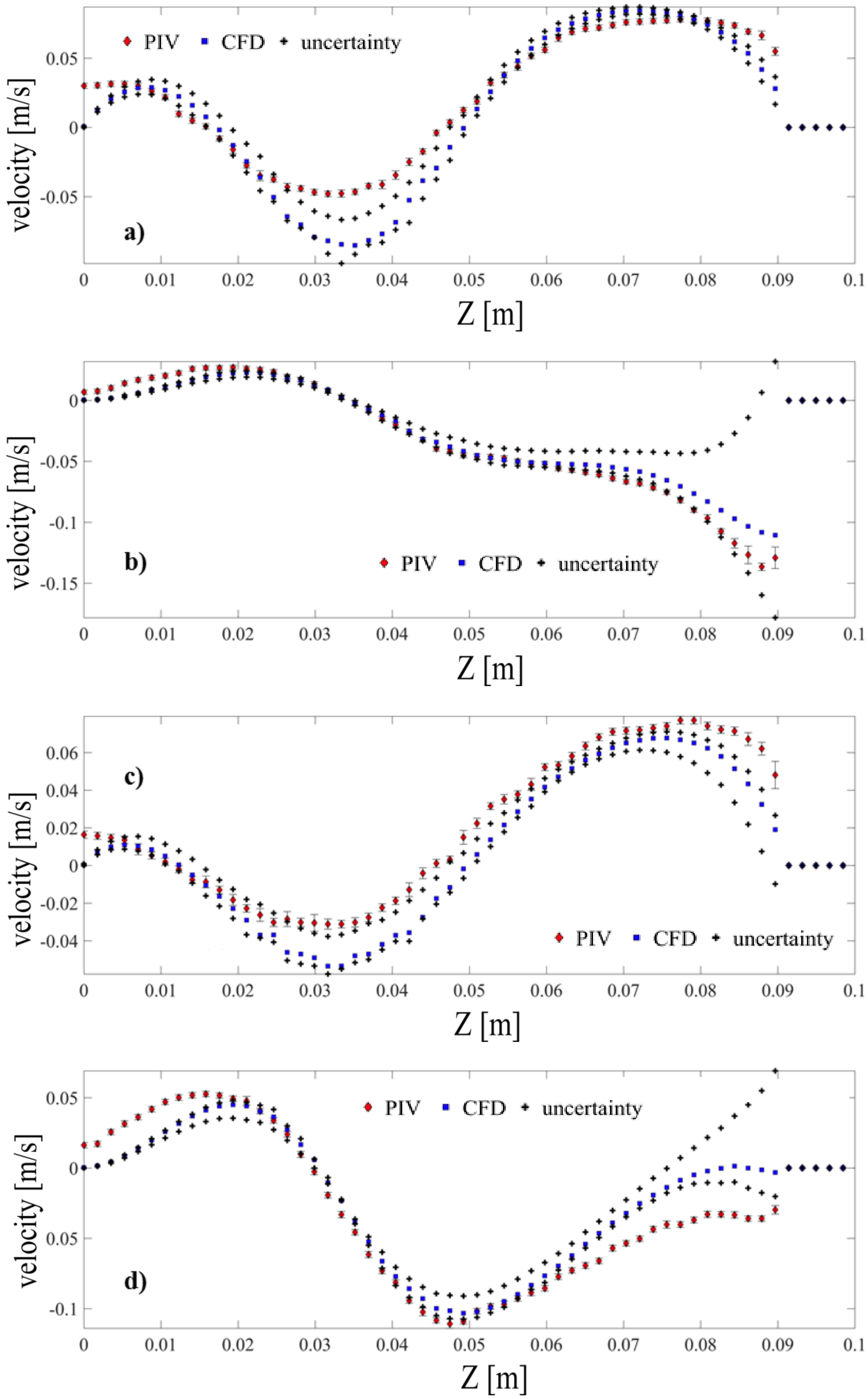

Figure 4. 17. Velocity profiles of V [a) and c)] and W [b) and d)] at two different Y positions [4.4 cm in a) and b), and 2.3 cm in c) and d)] for 20% gel and 140 rpm

Focusing on Figure 4. 17, one can see that also in this case the CFD is able to capture accurately the experimental velocity profiles. The uncertainties in the CFD simulations are small for most of the profiles, although near the blades these are magnified. The greatest uncertainties for W are found near the top blades, while for V near the lower blades (heights of 0.025 – 0.045 m). Similarly to the previous case, the velocity vectors near the walls of the tank, and in particular those near the bottom, are subject to the greatest experimental (relative) error.

The overall velocity profiles of the two remaining cases are presented in Figure 4. 18 and Figure 4. 19, and very similar conclusions can be drawn.

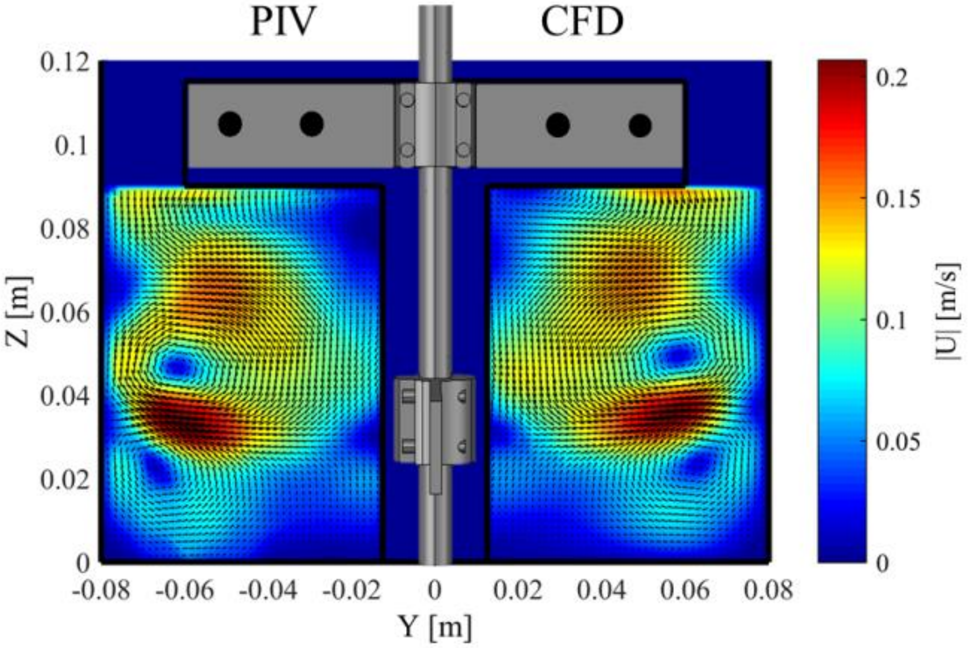

Figure 4. 18. PIV vs CFD velocity profiles on the plane X = 0 using the y- and z-velocity components for 5% gel and 120rpm

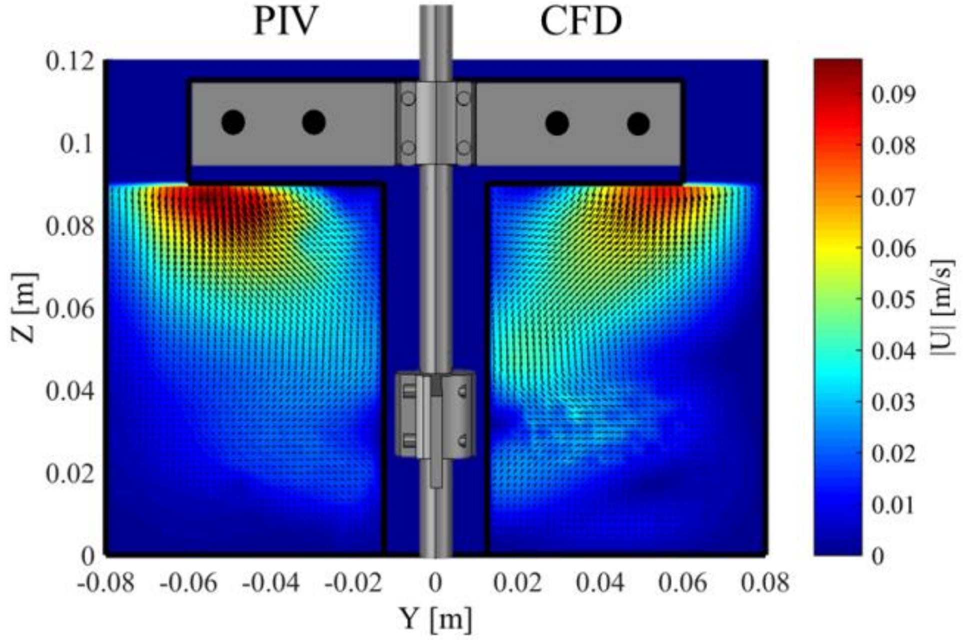

Figure 4. 19. PIV vs CFD velocity profiles on the plane X = 0 using the y- and z-velocity components for 20% gel and 80 rpm

4.5.2. Flow in the vessel

One can use the validated CFD model to study the characteristics of the flow in the whole vessel. The previous results revealed that the velocities in the y and z directions, and consequently their magnitude too, are significantly smaller than the tip speed (about 10% of the tip speed near the top blade). This indicates that this type of impeller provides little radial and axial flow motion compared to the angular flow motion. This can be shown by plotting the three-dimensional streamlines at the same impeller position used in the PIV experiments for the case of 5% gel mixture and 40 rpm impeller speed (Figure 4. 20).

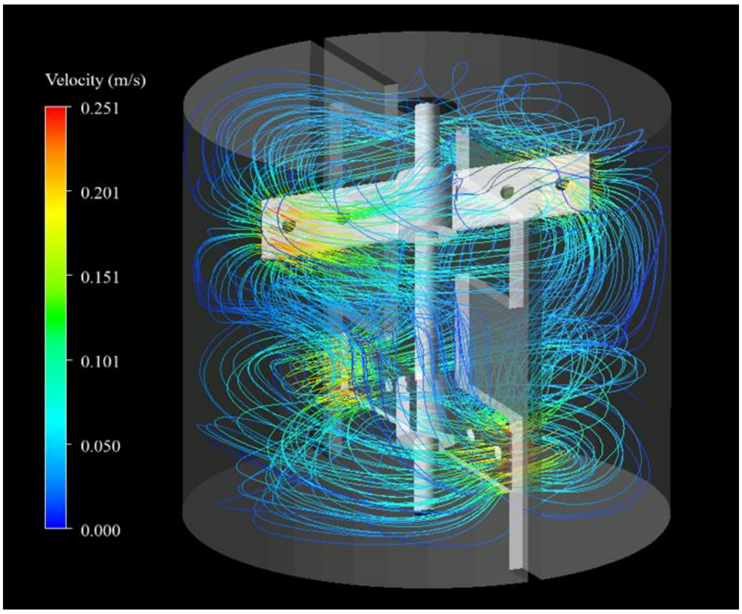

Figure 4. 20. Velocity streamlines for 5% gel and 40 rpm

As can be seen in Figure 4. 20, the highest velocities are found adjacent to the tip of the blades, and the velocity decays rapidly away from the impeller because of the high viscosity of the fluids; nevertheless, the streamlines reveal that there is circulation of the fluid in the entire tank, and they do not show evident stagnant zones (those with zero velocity) in the vessel. The streamlines also reveal that there is top to bottom recirculation, but the velocity magnitude is significantly smaller compared to the tip speed. As mentioned before, the dominant motion is in the angular direction.

The streamlines for the 20% gel mixture stirred at 140 rpm (Figure 4. 21) reveal similar patterns: strong angular velocity compared to the radial and axial ones, and velocity decay away from the impeller. In this case, however, the velocity decays even faster with distance from the impeller, as the fluid has stronger shear thinning behavior (smaller *n*) and higher viscosity compared to the 5% gel case. This creates a pseudo-cavern around the impeller, which is surrounded by quasi-stagnant fluid.

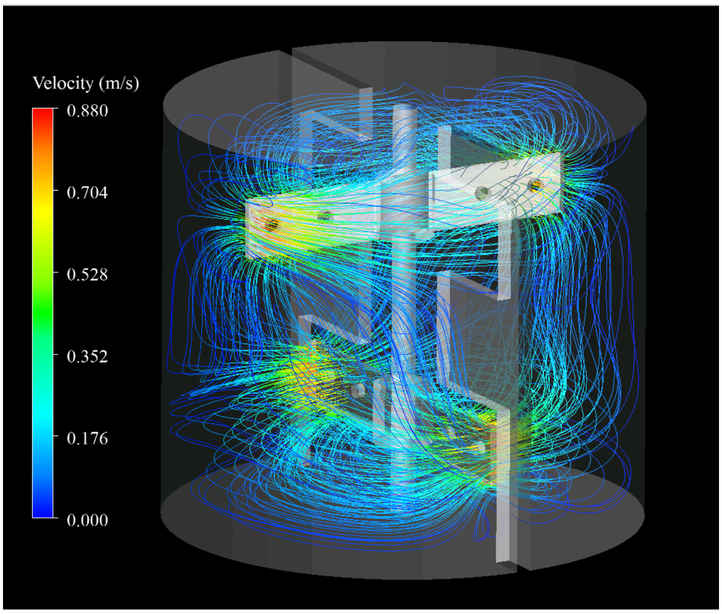

Figure 4. 21. Velocity streamlines for 20% gel and 140 rpm

Intuitively, for shear thinning fluids, desirable mixer design criteria involve good propagation of the fluid motion to the greatest part of the vessel. This can be assessed by setting different velocity thresholds (fractions of the tip speed), and determining the percentage of the fluid volume that moves at higher velocity than the thresholds. It is shown in Figure 4. 22 the isosurfaces of velocities equal to 10%, 30%, 50% and 70% of the tip speed for a 5% gel and 40 rpm impeller speed.

As can be seen, the velocity decays very rapidly away from the impeller. The highest velocities, those above 70% of the tip speed, are only found in close proximity of the tip of the blades (Figure 4. 22 (d)). Fluid with velocities above 50% of the tip speed is only found along the blades and in a small region behind the tip of the blades (Figure 4. 22 (c)). The impeller, however, is able to prevent the formation of stagnant zones (where the velocity completely vanishes) under the conditions studied (Figure 4. 22 (a)). The narrow gap between the blades and the baffles increases locally the shear rate, thus reducing the fluid viscosity; as a result, the fluid velocity between the low blades and the baffles is comparatively larger (Figure 4. 22 (b)).

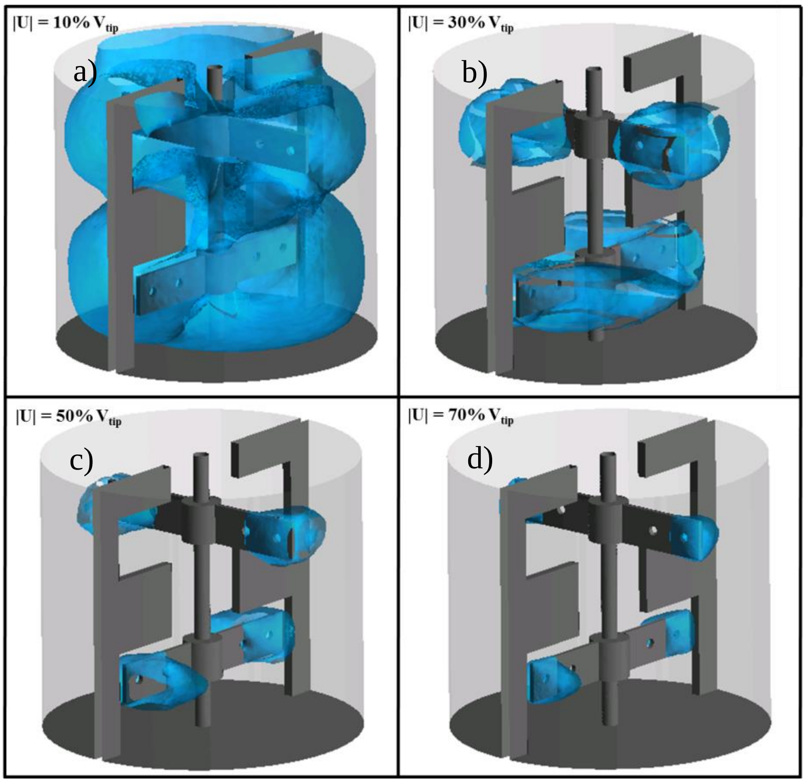

Figure 4. 22. Isosurfaces of velocities as fractions of the tip speed, a) 10%, b) 30%, c) 50%, and d) 70%

Quantitative information can also be obtained by extracting the fluid velocity magnitude in each computational cell, and plotting a histogram of the volume fraction of the fluid that has certain velocity relative to the tip speed (Figure 4. 23). The cumulative volume fraction of the histograms for all cases studied is also presented in Figure 4. 23. The profiles do not change significantly with the phase angle of the impeller. In all cases, low velocities relative to the tip speed are dominant. The cumulative plot is particularly helpful to identify the configurations that provide more efficient propagation of motion from the impeller to the fluid; these are denoted by a slow increase of the cumulative volume fractions against the relative velocity.

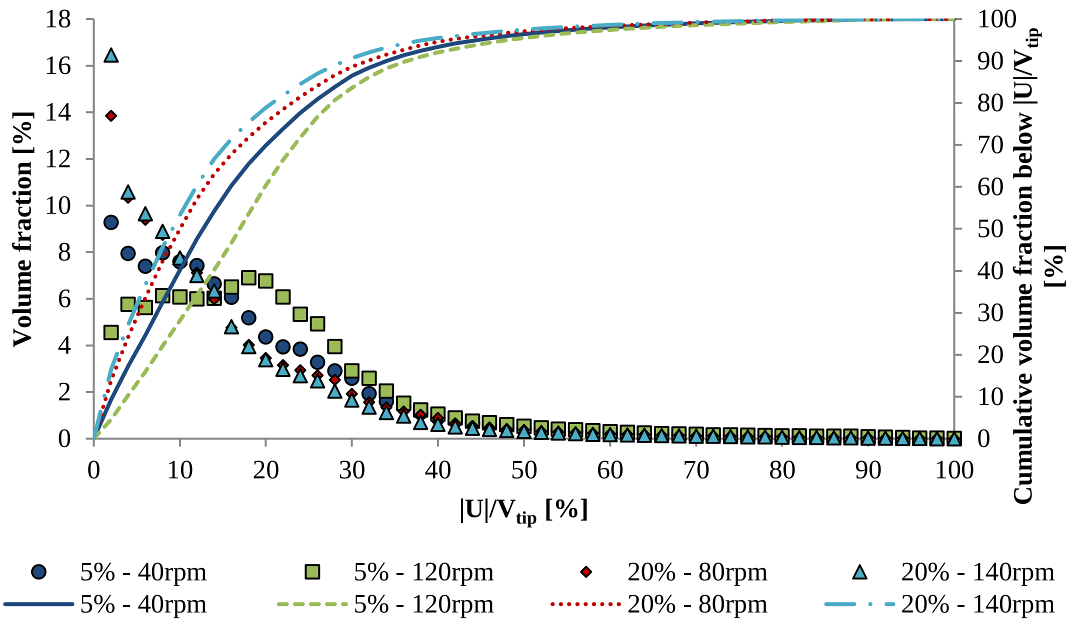

Figure 4. 23. Volume fraction of total fluid moving at different fractions of relative tip speed and cumulative volume fraction of fluid moving at velocities below $|U|/V_{tip}$. The phase angle of the impeller is the same as in Figure 4.22

Comparing the two cases of the 5% gel, one observes that the cumulative curve increases faster at 40 rpm compared to 120 rpm, which means that more fluid in the vessel has a low velocity relative to the tip of the blades at 40 rpm compared to 120 rpm. The two cases studied with 20% gel reveal similar curves in Figure 4. 23; so, there is no noticeable improvement in velocity distribution when rotational speed is increased from 80 to 120 rpm. Overall, the performance of the mixer is better for the lower gel mass fraction, regardless of the impeller speed. From Figure 4. 23 it is possible to conclude that this impeller and baffles designs are not particularly efficient at transmitting the velocity to the bulk fluid.

4.5.3. Effect of the holes

Holes on impellers are unique design features for some mixers treating highly viscous non-Newtonian fluids. Their purpose is related to a mechanical standpoint: they enhance stability of large impellers, and reduce the pressure on the blades, thereby reducing power consumption (STC Engineering, Personal communication). However, to the best of my knowledge, their effect on the fluid flow has not been studied. To do so, I plot the shear rate profiles (profiles of the magnitude of twice the rate of deformation tensor) on the front of the top blade and the viscosity contours for the cases of 5% gel and 40 rpm and 20% gel and 140 rpm in Figure 4. 24 a) and Figure 4. 24 b), respectively. Similar results are found for the remaining configurations.

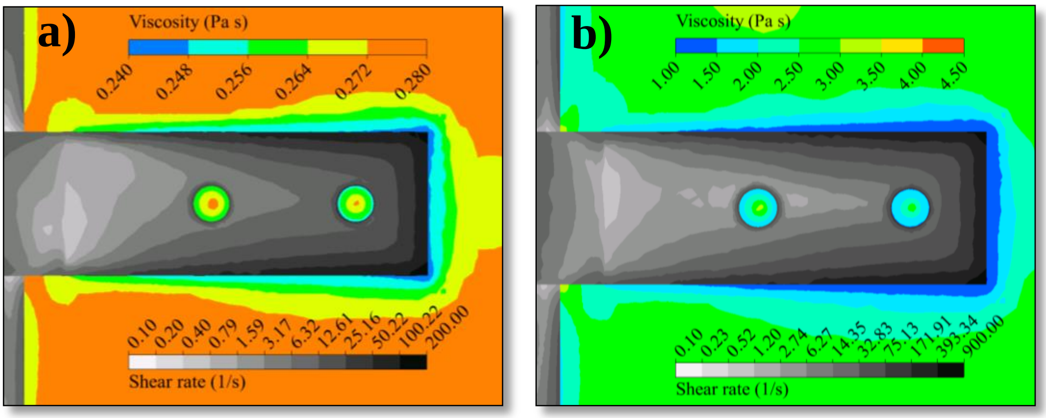

Figure 4. 24. a) Shear rate profiles on the top right blade a) 5% gel and 40 rpm, b) 20% gel and 140 rpm

As can be seen, the highest shear rates are found along the edges of the impeller blade, and particularly at the tip. The shear rate on the front face of the blade is lower than that on the edges, and it increases from the centre to the tip of the blade. The presence of the holes reduces the surface of the blade and increases its perimeter, thus increasing the total length of the edges of the impeller, and therefore the local shear rate (Figure 4. 24). For shear thinning fluids, increasing the shear rate locally is beneficial to enhance flow, since the viscosity of the fluid is reduced locally, and consequently the local velocity is increased.

Overall, the shear rate ranges from 0.1 s^{-1} to 200 s^{-1} for the 5% gel and 40 rpm case (Figure 4. 25 a)) and from 0.1 s^{-1} to 900 s^{-1} for the 20% gel and 120 rpm case (Figure

4. 25 b)). This proves that the shear rate range investigated in Section 4.2.2 is adequate for the simulations. The shear rate profile on both the bottom and top blades is practically identical. However, the shear rate profile on the baffles changes with the relative position of the impeller. In the case shown in Figure 4. 25 a) and Figure 4. 25 b), the bottom blades are passing through the baffles, and the shear rate on the baffles increases locally near the bottom blade. This can be linked to Figure 4. 22 b), where the fraction of fluid that has a velocity above 30% of the tip speed is greater around the lower blade compared to the top blade.

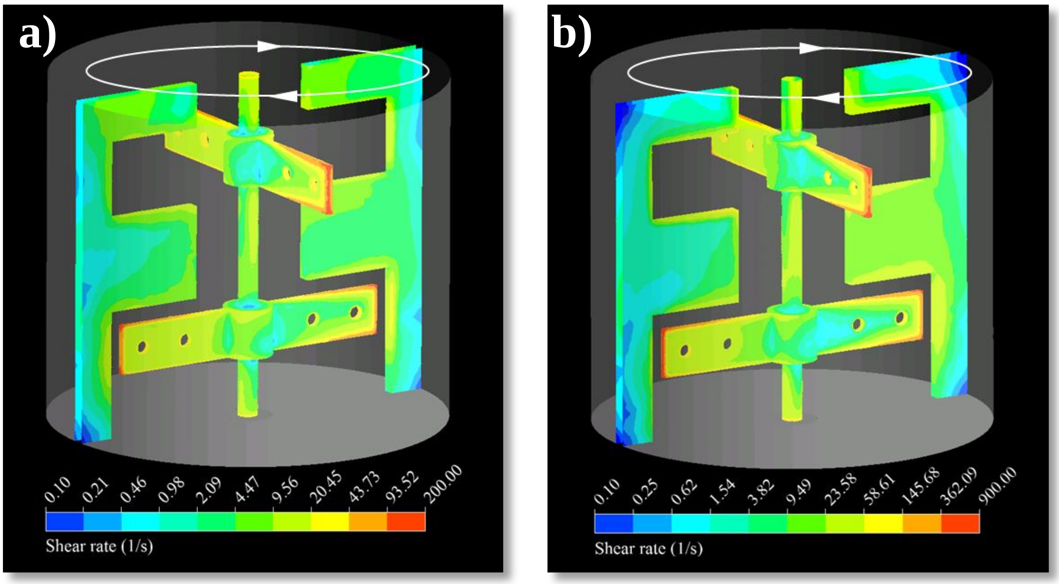

Figure 4. 25. Shear rate profiles in the impeller and the baffles a) 5% gel and 40 rpm, b) 20% gel and 140 rpm

4.5.4. Power consumption

To better characterize the impeller behaviour, the power required to mix both Newtonian and non-Newtonian fluids at different operating conditions was calculated. Since the PIV validation of the CFD model has given a positive outcome, it is possible to trust in the accuracy of the model and therefore to now use it to predict power consumption. To do so, the torque on the impeller surface at each impeller position over an entire revolution was computed, and it was averaged to calculate the power consumption of the impeller. The details of how to calculate the power consumption of the impeller from the computed torque can be found elsewhere (Cortada-Garcia et al., 2017). The results are presented in Figure 4. 26. To construct the power curves, the Metzner and Otto approach (Metzner and Otto, 1957) was followed, and Eq. 4.1 was used to compute the value of the Reynolds number. As previously mentioned, the constant of this impeller is 15.

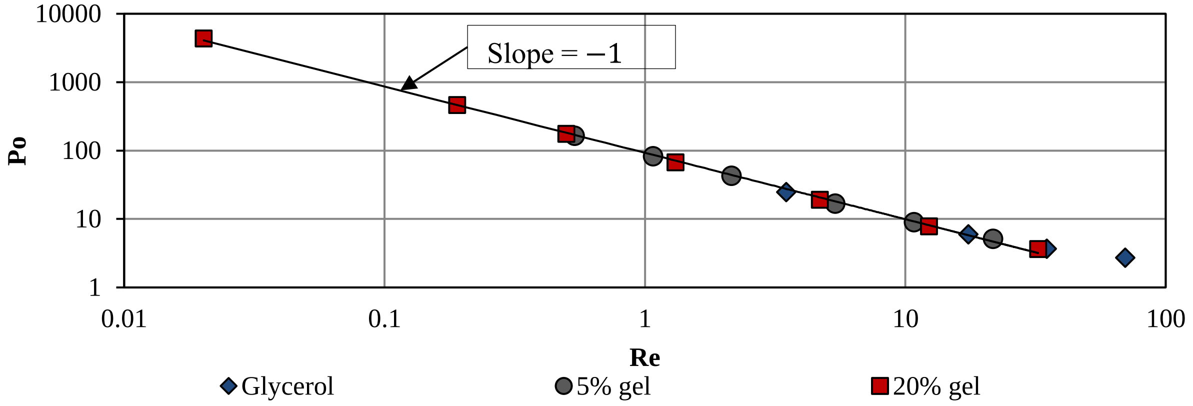

Figure 4. 26. Power curves of the mixing system with the two mixtures (20% and 5%wt gel) and with glycerol

As can be seen in Figure 4. 26, the laminar regime, where the power curve has a slope of -1 in a double logarithmic plot of the Power number against the Reynolds number, extends up to Re approximately equal to 50. This experiments also include the early transition regime as shown in Section 4.5.1, and the CFD simulations predict adequately the flow behaviour in both flow regimes.

The Metzner and Otto constant can be used to compare the efficiency of the impeller with that of other impellers used to mix non-Newtonian fluids. The lower the value of this constant, the less the power required by the impeller to agitate the fluid at a given

Reynolds number. The impeller hereby studied has a similar performance to Maxblend ^{TM}, which is extensively used in industrial applications related to the mixing of highly viscous fluids. The Maxblend ^{TM} constant is in the range of 15 to 20 (Stobiac et al., 2014, Patel et al., 2011, Fradette et al., 2007). The Paravisc ^{TM} impeller is also used in industrial applications dealing with highly viscous fluids, and its constant is significantly higher; it is approximately 30 (Iranshahi et al., 2006). Other common configurations for mixing of highly viscous non-Newtonian fluids are two coaxial impellers, a central one, such as the Scaba impeller or the Rushton turbine, and an external one, such as an anchor impeller. The Scaba impeller and the Rushton turbine have similar constants: 10.5 (Pakzad et al., 2013b) and 9.6-11.5 (Cortada-Garcia et al., 2017, Patel et al., 2012), respectively. In contrast, anchor impellers have larger constants of around 23 (Pakzad et al., 2013a). Different methodologies have been proposed to obtain power curves for coaxial mixers (Thibault and Tanguy, 2002, Foucault et al., 2004, Farhat et al., 2008, Pakzad et al., 2013a), but direct comparison of power consumption between single and coaxial impellers has not been reported in the literature.

Although impellers with low constant are desirable, the design of the mixing tank cannot be based only on this coefficient. For instance, the agitation of highly viscous shear thinning fluids and yield stress fluids with impellers such as the Rushton turbine or the Scaba impeller leads to pseudo-cavern and cavern formation, respectively. In contrast, the impeller presented in this study has a higher constant, but, as shown in section 4.5.2, it minimises stagnant zones, so it is preferable in this case.

4.6. Conclusions

In this study, I characterized computationally the flow behaviour of shear thinning fluids (modelled with the Carreau law) in a scaled-down mixing tank used in the manufacturing of complex oral health products. The CFD model was validated against experimental velocity profiles in the stirred tank. The experimental errors were thoroughly assessed and presented in the form of error bars. The interrogation error was found to be the most significant in this case. The maximum uncertainty when comparing the computational and experimental results was also evaluated. Overall, experiments and simulations agree quite well. The impeller performance was assessed both qualitatively and quantitatively. I first reported velocity streamlines; these revealed that the impeller generates strong angular motion compared with the axial and radial components. Then, the regions in which the fluid is agitated more vigorously were identified (with higher velocity), and the percentage of the fluid that has speeds above given thresholds was quantified. This study revealed that the impeller is able to minimize stagnant zones, but most of the fluid has a velocity ten times smaller than that of the tip of the blade. This situation is worsened for fluids with higher viscosity and higher shear thinning behaviour (that of 20% gel). Then, the effect of the holes on the fluid flow was evaluated, and it was concluded that they increase the shear rate locally by increasing the perimeter of the edges of the impeller. This result is positive for shear thinning fluids, since the viscosity is reduced locally, but it can be counter-productive for shear thickening fluids. Finally, the power constant of this impeller was calculated, and it is comparable with other common geometries to agitate highly viscous non-Newtonian fluids. This Chapter intended to demonstrate the importance of performing careful studies when designing mixers to deal with complex fluids.

5. Mixing time study of highly viscous fluids in stirred tanks

5.1. Introduction

In this Chapter, the mixing of passive tracers in glycerol/carbomer gel solutions is investigated experimentally using the planar laser induced fluorescence (PLIF) technique.

CFD is used as a predictive tool to estimate mixing time using the transport of species model. The alternative method for estimating mixing times, the Lagrangian particle tracking technique, is also used. Other computational methods for evaluating mixing efficiencies, the Poincaré maps and the stretching fields, are also presented.

Chapter 5 is structured as follows. In Section 5.2, the geometrical configuration of the mixing tank setup is shown first, followed by a summary of the rheological properties of the fluids used and of the flow conditions evaluated. Additionally, the setup of the PLIF experiments and the procedure to calculate the mixing time are presented. In Section 5.3, the details of the CFD model with the species equation are presented. The alternative method to evaluate the mixing time computationally, the Lagrangian tracking of particles, is also detailed in Section 5.3. In Section 5.4, the experimental and computational mixing results are discussed. Additionally, the evaluation of the mixing performance through Poincaré maps and stretching fields is presented. Conclusions are summarised in Section 5.5.

5.2. Methodology

5.2.1. Apparatus

The mixing studies were carried out on the same mixing tank presented in Section 4.2.1. The main features of the setup are: the cylindrical acrylic tank is equipped with a stainless steel dual impeller with two flat blades on each position and with two holes on each blade. The tank has two baffles, and it is enclosed in a square tank, made of acrylic, which is filled with glycerol. The temperature can be regulated by recirculating fluid through the outer box. The acrylic material of the stirred tank has refractive index equal to 1.4945, which matches the refractive index of the processing fluids (1.4675 and 1.4645 for glycerol and gel at 25 ºC, respectively) to avoid optical distortions during the PLIF experiments. A schematic of the mixing tank can be seen in Figure 4. 2.

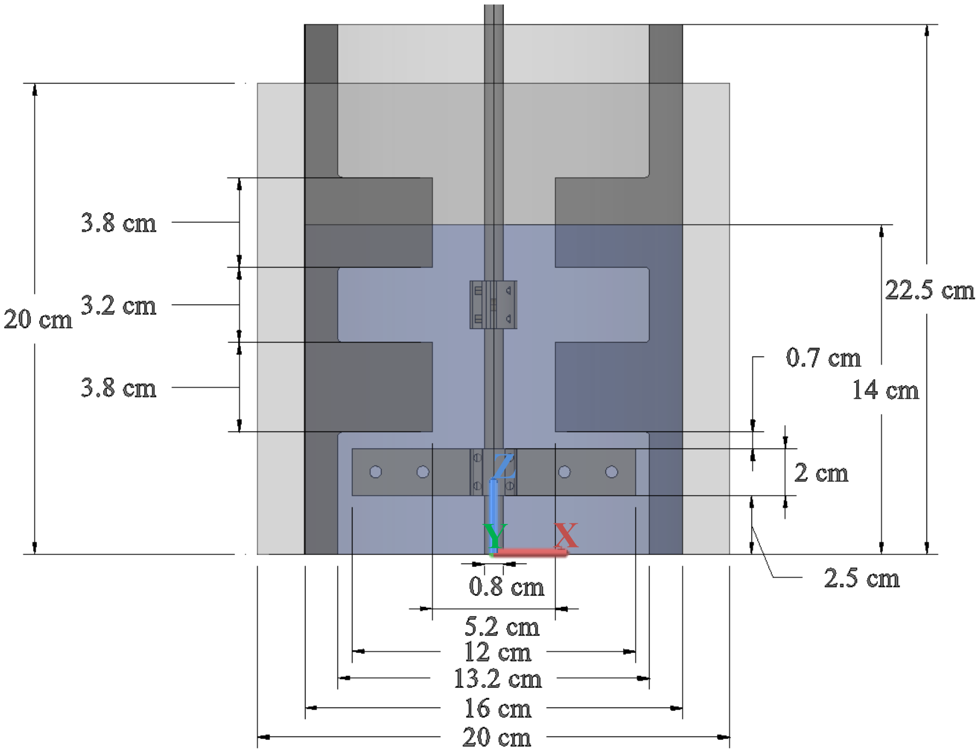

Figure 4.2 (bis). Schematic and dimensions of the tank, impeller, baffles, and liquid height

5.2.2. Fluids and flow conditions

The test fluids used in this study were glycerol and a mixture of a carbomer gel (20%wt) with glycerol (80%wt). As in the previous chapters, the rheological properties of these two fluids were measured and used in the simulations. The rheometer used is described in Section 4.2.2. In total, four cases were considered in this work, which are summarised in Table 5. 1.

Table 5. 1. Flow conditions and the corresponding properties of the fluids of the mixing studies

Case	Glycerol mass fraction [%]	N [rpm]	T [ºC]	λ [s]	n [-]	μ_0 [Pa s]	μ_∞ [Pa s]	Re [ ]
1	100	30	23	-	1	0.917	0.917	9.42
2	100	60	24	-	1	0.916	0.916	18.8
3	80	80	48	92.80	0.6827	17.251	0.683	9.94
4	80	140	52	111.69	0.6437	17.424	0.509	26.8

5.2.3. PLIF: setup and image acquisition

The PLIF set-up includes a dual cavity Nd:Yag green laser (532 nm) (Litron Laser®, 15 Hz, 1200 mJ) and a straddling CCD camera with 2048 x 2048 pixels (TSI PowerView™ Plus) with maximum frequency of 16 frames per second, equipped with an AF Nikkor 50mm f/1.8D prime lens (Nikon®). A hall switch sensor was used to capture images at the same phase angle.

The Rhodamine 6G dye diluted in the working fluid was used as tracer. In a typical experiment, a small proportion of the working fluid was separated from the main bulk, and the Rhodamine 6G was injected in it. A different mechanically stirred tank equipped with a propeller was used to homogenise the tracer. To ensure that only the light emitted from the Rhodamine 6G was recorded by the camera, an orange filter with a cut-on wavelength at 570 nm was used. The laser and the camera were synchronized by a Laser Pulse Synchroniser (Model 610035 TSI) and they were controlled via the Insight 4G (TSI) software. The laser beam was passed through a collimator (Model 610026 TSI) and two cylindrical lenses (25 mm, and 15 mm) to form a narrow plane of 1 mm thickness. The laser plane was reflected on a 45º silver coated mirror and entered the stirred vessel from the bottom. To maximize the visualization area, the concentration profiles were captured on a vertical central plane of the tank, when the top blades of the impeller were parallel to that plane. A sketch of the setup is shown in Figure 4. 5.

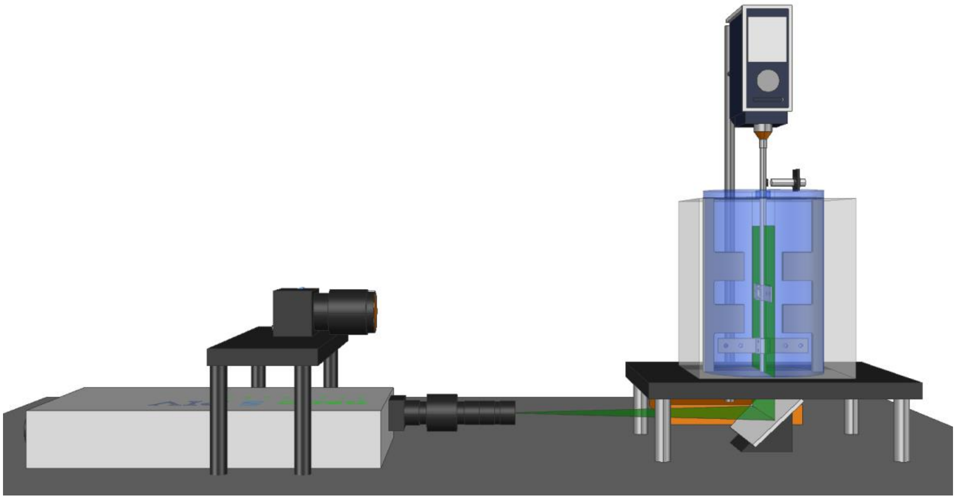

Figure 4. 5 (bis). Sketch of the main components of the experimental set-up for the PLIF measurements

5.2.4. Experimental mixing time calculations

In a typical experiment, two images were taken per impeller revolution during the mixing experiment. This was achieved by attaching two magnets (diametrically opposite) to the shaft of the impeller. After being digitalised, the images depict the instantaneous distribution of light intensity on a greyscale ($C(x, y, t)$) in the plane of measurement. Before starting the experiment, ten images were taken to obtain an averaged background image $C_B(x,y)$. Similarly, at the end of the experiment, 10 images were captured to obtain the averaged final image $C_\infty(x,y)$.

The PLIF images were analysed following the method proposed by Houcine et al. (1996) (see also (Hall et al., 2004, Coroneo et al., 2011)). The instantaneous, local, normalised concentration is computed as:

$$C_n(x,y,t) = \frac{C(x,y,t) - C_B(x,y)}{C_\infty(x,y) - C_B(x,y)} \qquad \text{(Eq. 5.1)}$$

This method can be used when the emitted fluorescent intensity depends linearly on the tracer concentration. The calibration curve that relates the pixel intensity to the tracer mass fraction in the liquid can be seen in Figure 5. 1. It is important to clarify that what is presented here as 100% tracer mass fraction is the process fluid, in this case glycerol, with a concentration of $2.09 \cdot 10^{-7} \frac{\text{mol of Rhodamine 6G}}{\text{L}}$. This means that it is possible to obtain a linear relation of the pixel intensity with concentrations of Rodamine 6G lower than $1.25 \cdot 10^{-7}$ mol/L (equivalent to 60% of the tracer mass fraction) for the exact setup configuration, including the distance between the camera and the mixing tank and the aperture position.

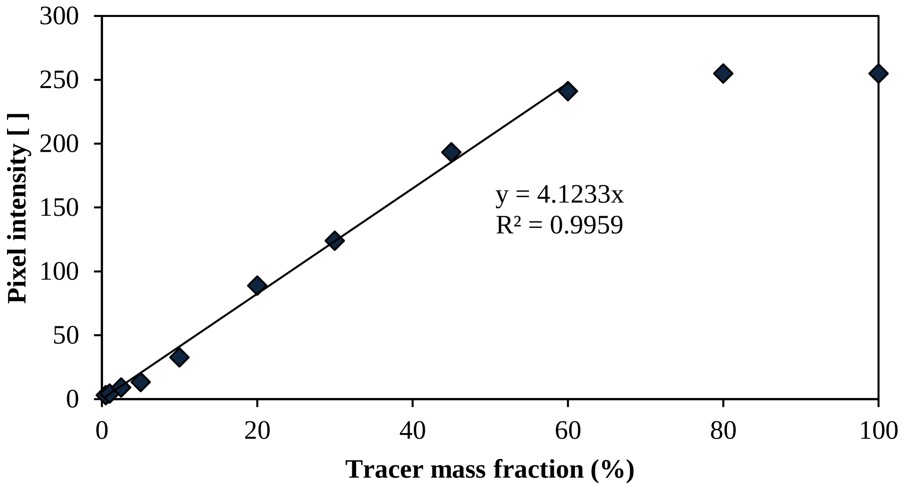

Figure 5. 1. Calibration curve

The standard deviation of the concentration was used to evaluate the spatial degree of homogeneity in each image:

$$\sigma(t) = \sqrt{\frac{1}{N_{pix}} \sum_{i=1}^{N_{pix}} \left(C_n(x, y, t) - \overline{C}_n(t) \right)^2} \qquad \text{(Eq. 5.2)}$$

where N_{pix} is the total number of pixels excluding the masked parts of the image, $C_n(x, y, t)$ is defined in Eq. 5.1, and $\overline{C}_n$ is the average concentration of the image at a given time (t) (although it is very close to the unity at all times).

The standard deviation was rescaled to take values from 0 to 1:

$$\sigma_N = \frac{\sigma - \sigma_{min}}{\sigma_{max} - \sigma_{min}} \qquad \text{(Eq. 5.3)}$$

5.3. Computational simulations

As previously mentioned in Section 2.4.3.3, CFD models have been used to predict the mixing time in stirred tanks. To the best of my knowledge, these models tend to be limited to single phase multicomponent flows where it is possible to obtain a steady state solution of the flow field. Once the flow field is obtained, the secondary component is placed in the system, and the convection-diffusion equation is solved along the mixing time. In mixing tanks, this is only in the absence of baffles, which is not the case of this study.

Models with high quality meshes are needed for accurate transient results of convective-diffusive transport of species; these are often impractical due to long simulation times. Often, lower mesh qualities suffer from numerical diffusion, which tend to decrease the mixing times. This is particularly pronounced in the case of three dimensional flows (Liu, 2011). An alternative method to model fluid mixing is the use of a Lagrangian scheme. In this case, fictitious massless particles are placed in the flow domain; these particles do not interact with the fluid, and they move at the instantaneous fluid velocity at their position corrected by a random walk. Challenges of this strategy are the correct estimation of the number of particles and the number and size of discrete elements where the particles are counted (averaging volumes). In this study, it was attempted to compare both computational strategies for predicting the mixing time in single phase multicomponent flows using a complex mixer geometry and highly viscous non-Newtonian fluids. The details of how mixing time is calculated with the Lagrangian scheme can be found in section 5.3.2.2.

5.3.1. CFD modelling strategy

The CFD model described in Section 4.3 was used as a starting point for the single phase multicomponent mixing simulations. The main boundary conditions can be summarised as follows: on all the solid surfaces bounding the computational domain, the no-slip boundary condition was applied. At the top boundary, where the liquid-gas interface lies, the components of the viscous stress force referring to the unit vector normal to the interface were set equal to zero. The flow domain was discretised into a moving zone, which encloses the impeller, and a stationary one for the rest of the domain (Figure 4.7). The computational grid and the solution methodology for the first two steps was identical to that presented in Section 4.3. The computations were carried out in six parallel processors using a 3.10 GHz Intel® Xeon ® CPU E5-2687W v3 with 192.0 GB RAM.

The strategy followed to solve the problem has three steps. The first is the initialisation of the flow. For this, a single component (one chemical species) was used, and the MRF method was used to provide an initial solution, which was used as initial condition for the second step.

In the second step, the model was switched from steady state to transient, and the SM model was implemented to obtain a periodic solution. Up to this point, the model only had one chemical component, and the periodic flow solution was ensured by the observation of a periodic torque report and periodic values of the residuals of the velocity components at the end of each time step.

Once the periodic flow solution was obtained, the model was modified to include the second chemical component which has the same physical properties as the first. The bulk fluid was assigned to a mass fraction of 1 of the primary component. The tracer was placed along the whole cross-sectional area of the tank in the space comprised by the top of the tank and one centimetre below it. The self-diffusion coefficient of glycerol is $1.4 \cdot 10^{-11}\ m^2 s^{-1}$(D'Errico et al., 2004). In the literature, glycerol has been used to study purely convective mixing because of its low value of self-diffusion (Alvarez et al., 2002), and it is expected that the diffusive mixing of the non-Newtonian mixtures should be even less significant. For this reason, the diffusivity of the mixtures of glycerol with the carbomer gel was not studied.

5.3.1.1. Mixing time

The distribution of the mass fraction of the tracer in the mixing tank was recorded every half revolution (every period). The grid used in this study is unstructured; hence, the resulting mass fraction profile cannot be used as it is to compute the standard deviation by using Eq. 5.2. Instead, the results need to be translated into a regular grid (different from the original CFD one) as in Section 4.3.2. The experimental concentrations are obtained per-pixel. It is therefore not practical to translate the computational results from the central plane of the original CFD grid to a regular grid that matches the resolution of the camera.

Since the CFD provides three dimensional results, the entire flow domain can also be used to estimate the mixing time. Ideally, using the information in the 3D grid would lead to an identical trend as in the 2D case, but the evolution of the normalised standard deviation against time would be significantly smoother for the 3D case. The best strategy to divide a cylinder in equal elements consists of using three variables: height, angular position, and radius. First, the cylinder is divided into m concentric sections of the same area using Eq. 5.4.

$$r(i) = R\sqrt{\frac{i}{m}} \qquad \text{(Eq. 5.4)}$$

where r is the radius of the section *i* and *R* is the radius of the outer cylinder, or radius of the vessel.

Then, the concentric cylinders are divided into l sections of equal height. Finally, the cylinder is divided into n intervals for the angular position equally spaced from 0 to 2π. The resulting number of elements given by this method is calculated as:

$$\#elements = m \cdot l \cdot n \qquad \text{(Eq. 5.5)}$$

Figure 5. 2 is a visual representation of six isovolumetric elements of a cylinder where $m = 3$, $l = 2$, and $n = 4$ (the whole cylinder has 24 elements in total).

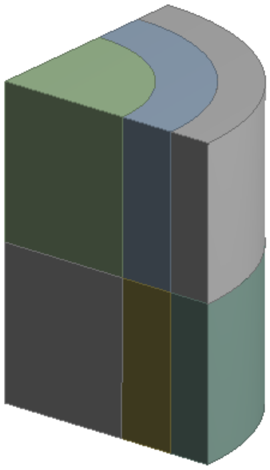

Figure 5. 2. Example of six isovolumetric elements of a cylinder

I selected 36 intervals for the angular position, 28 intervals of the heights, and 10 radial positions. This leads to 10,080 elements, which is convenient for the Lagrangian particle tracking simulations as it will be shown in Section 5.3.2. To evaluate the mixing time, the normalised standard deviation of the tracer mass fraction (as in Eq. 5.2) was computed over time using the new discretised grid with isovolumetric elements, and the normalised standard deviation was rescaled to take values from 0 to 1 (as in Eq. 5.3).

5.3.2. Particle tracking

In particle tracking, fictitious massless particles are placed in the flow domain; these particles do not interact with the fluid and move with the instantaneous fluid velocity at their position corrected by a random walk. Because the flow velocity is strongly affected by the relative position of the blades and the baffles, it is not possible to freeze the velocity profile at a single impeller position and track the particles using this unique velocity field. Instead, a transient velocity field is needed.

For the particle tracking simulations, the velocity fields in the CFD domain obtained after every one degree of impeller movement were used; only the velocities over half a revolution of the impellers are needed because the flow is periodic. These velocity fields were imported into Matlab to perform the particle tracking simulations. The velocity field was updated at each time step. At each time step, the code calculates the velocity of each particle from the velocities at the four closest nodes in the grid, as shown in Figure 5. 3.

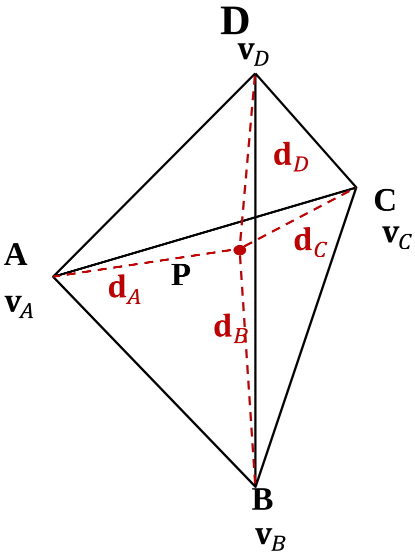

Figure 5. 3. Location of particle P, and the four closest nodes from the CFD grid (A, B, C, and D)

Diffusion in the motion of the particles can be incorporated via a random walk model. The equation that describes the movement of the particles at each time step is:

$$\mathbf{x}_{t+1} = \mathbf{x}_t + \mathbf{v}_P \Delta t + \sqrt{2\mathcal{D}\Delta t}\,\boldsymbol{\varepsilon} \qquad \text{(Eq. 5.6)}$$

where $\mathbf{x}_t$ is the position vector at time t. The velocity of the particle is given by the sum of the second and third terms on the right-hand side of Eq. 5.6 divided by Δt. The second term is the deterministic part, while the third term is the random part (which is related to diffusion). $\mathbf{v}_P$ is the deterministic velocity of the particle (which coincides with the fluid velocity at the particle location) calculated from the interpolation of the velocities in the four closest nodes of the CFD grid (Figure 5. 3) with the following equation:

$$\mathbf{v}_P = \left(\sum_{i=A}^{D} \frac{1}{\mathbf{d}_i}\right)^{-1} \sum_{i=A}^{D} \frac{\mathbf{v}_i}{\mathbf{d}_i} \qquad \text{(Eq. 5.7)}$$

In Eq. 5.6, $\mathcal{D}$ is the diffusion coefficient, which is of the order of 10^{-11} [m^2/s] for glycerol at 25 ºC (D'Errico et al., 2004), and $\boldsymbol{\varepsilon} = (\varepsilon_x, \varepsilon_y, \varepsilon_z)$ is a vector whose components are noncorrelated Gaussian random numbers: the mean is equal to zero and standard deviation is equal to one (Olivieri et al., 2015).

5.3.2.1. Additional particle tracking considerations

For different reasons, such as the random walk of the particles or the constant update of the impeller position, particles might end up leaving the mixing tank. To prevent this, a piece of code was written so that the particles that ended up being trapped inside the impeller or that left the space occupied by the fluid were immediately relocated at their former position.

5.3.2.2. Computational mixing time

To be able to calculate the standard deviation of the tracer mass fraction as in the CFD simulations (Eq. 5.2), two parameters are need to be selected: number of particles and size of the averaging volumes. To the best of my knowledge, there is no guide on how to select neither of the two, but it exists an obvious relationship, the more particles used in the simulation, the smaller the averaging volumes can be, and hence, the more accurate the results of the simulations should be. However, this also leads to an increased computational cost and time. Hence, a systematic methodology is needed to find the optimal values for these two parameters. Due to time constraints, I was only able to test one set of conditions, which is described next.

To match the experimental conditions, 100,800 homogeneously dispersed massless particles were placed in the volume comprised by the cross-sectional area of the tank in the space between the top of the tank and a centimetre below it. To simplify the calculation of the concentration of particles in the elements of the tank, the mixing tank was discretised in elements of the same volume as shown in Figure 5. 2. If this condition is met, at perfect mixing there should be the same number of particles in each element.

To have a first approximation of the ideal averaging volume size (and number), it was thought to use the information obtained experimentally with the PLIF technique. However, this experimental technique (in this case) was used to measure how far each pixel is from reaching its intensity at final time, and there is no available information about real concentration.

Taking into consideration simulation cost and time, it was decided that for this first approximation to the problem, at perfect mixing, the number of particles in each averaging volume would be ten. The reasoning behind this number is that, if there was no improvement in simulation time, it would be difficult to justify the switch from the standard Eulerian CFD methodology to this Lagrangian approach. A priori, it is not possible to determine if this number is high enough as to provide a continuous tracer mass fraction profile.

By setting that under perfect mixing conditions there should be ten particles per averaging volume, the total number of averaging volumes (or elements) is equal to 10,080. By choosing the same values as in Section 5.3.1.1 (36 intervals for the angular position, 28 intervals of the heights, and 10 radial positions) the volume equivalent of a particle is approximately 0.027 ml. To evaluate the mixing time, the number of particles on each element was computed, which was used to calculate the tracer mass fraction on each box. The normalised standard deviation of the tracer mass fraction (as in Eq 5.2) was computed over time, and it was rescaled to take values from 0 to 1 (as in Eq 5.3).

5.4. Results and Discussion

In this section, the experimental and computational results of the mixing time are presented first and then they are compared. After that, the two alternative methods to compare mixing efficiency are presented: the Poincaré maps, and the stretching fields.

5.4.1. Evaluation of mixing time

5.4.1.1. Experimental

The mixing time was evaluated experimentally for all four cases presented in Table 5. 1 using the procedure described in Section 5.2.4. Representative normalised concentration profiles for case 2 are presented in Figure 5. 4 for the first 40 seconds of the mixing experiment. For these experiments, the tracer was placed at the top of the tank.

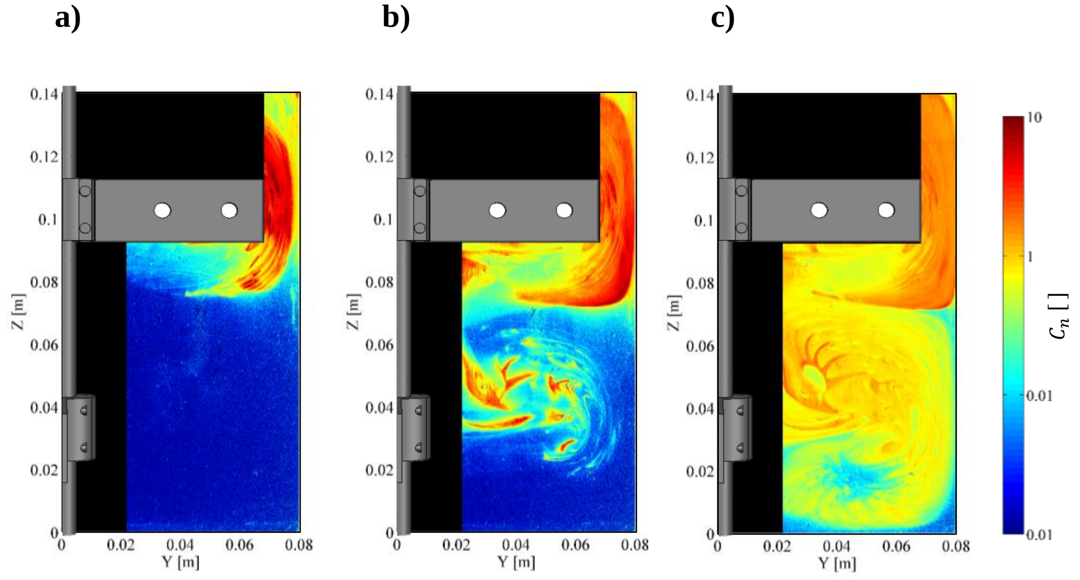

Figure 5. 4. Concentration profiles for case 2 shown in Table 5. 1 at a) 10, b) 25, and c) 40 seconds for the mixing experiments

Figure 5. 4 shows how the tracer is initially projected towards the walls of the tank on a periodic fashion. At each period (half a revolution) the tracer is stretched; this creates thinner and thinner filaments of the tracer, which cause the tracer to spread in the bulk fluid. Additionally, a portion of the tracer progresses further down to the second blade on the downward whirl near the shaft, and a second stretching loop is created near the lower blade. The same mechanism of periodic stretching is the main cause of the mixing. Hence, it is possible to conclude that this is primarily a convective mixing problem. At some point, the filaments are so thin that mixing by diffusion may start gaining importance, but this transition cannot be assessed just by observing the images. The resulting mixing time for all four cases presented in Table 5. 1 is presented in Section 5.4.1.4.

5.4.1.2. CFD

Transient CFD simulations are very demanding. Because of the long computational time, only the first 60 seconds of mixing for case 2 shown in Table 5. 1were simulated. This is equivalent to 60 revolutions, and it was achieved in approximately four months of simulations. Representative normalised concentration profiles are presented in Figure 5. 5.

In Figure 5. 5 it is possible to observe that overall, the mixing pattern is similar to that presented in Figure 5. 4, but the resolution of the CFD grid does not allow to capture the high detail of the filaments observed in the experiments. This indicates that the CFD grid, although it was fine enough to properly capture the flow mechanics in Chapter 4, it might need a higher resolution to model more accurately the transport of species. However, a much finer grid would have a direct impact on the simulation time and effort required to solve the problem.

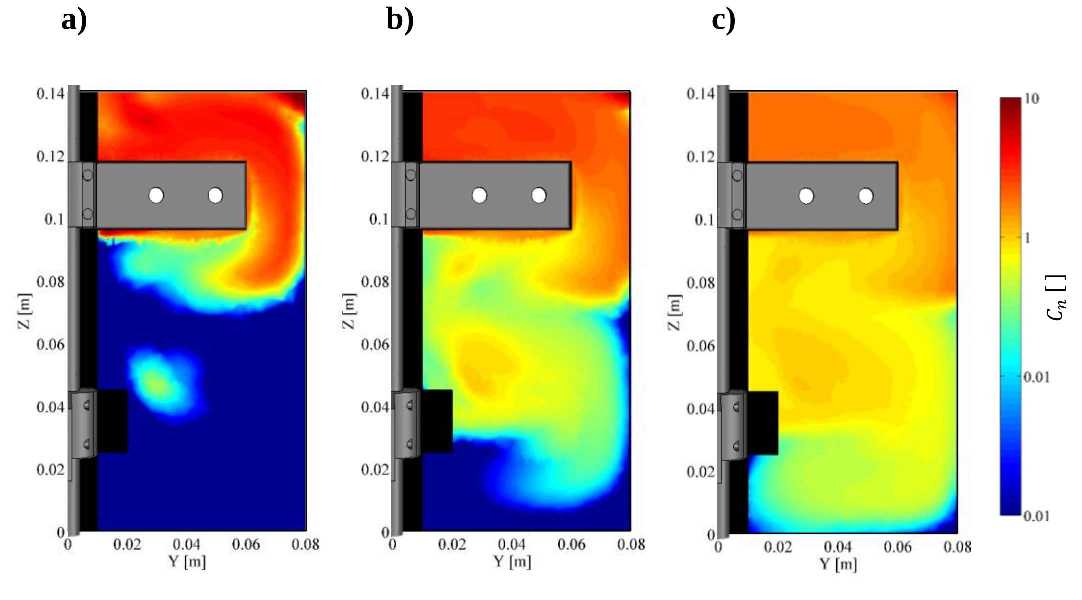

Figure 5. 5. Concentration profiles for case 2 shown in Table 5. 1 at a) 10, b) 25, and c) 40 seconds for the CFD simulations with the transport of species equation

5.4.1.3. Particle tracking

Modelling the mixing of the tracer with the bulk fluid using the particle tracking method is also very demanding. As mentioned in Section 5.3.2, the periodic velocity field is imported into Matlab at each time step, and the particles introduced in the flow move at their local velocity corrected with a diffusive term. In this case, the simulation time is significantly reduced because there is no need to solve the momentum-balance equation at each time step. In contrast, the computational efforts are devoted to finding the neighbouring nodes of the CFD grid for each particle to determine their velocity. Hence, the more particles introduced in the flow, the higher the computational time. Using 100,800 particles, the simulation time is approximately three times faster than that of the CFD. The mixing process of cases 2 and 4 presented in Table 5. 1 were simulated.

The normalised concentration profiles for the particle tracking method for case 2 shown in Table 5. 1 are presented in Figure 5. 6. As it can be seen, the overall mixing trend agrees with the experiments, but the details of the mixing structures are not well captured. This is caused by the size of the elements where the particles are counted, which is inversely proportional to the number of particles placed into the flow. Hence, for higher resolution a greater number of particles is needed.

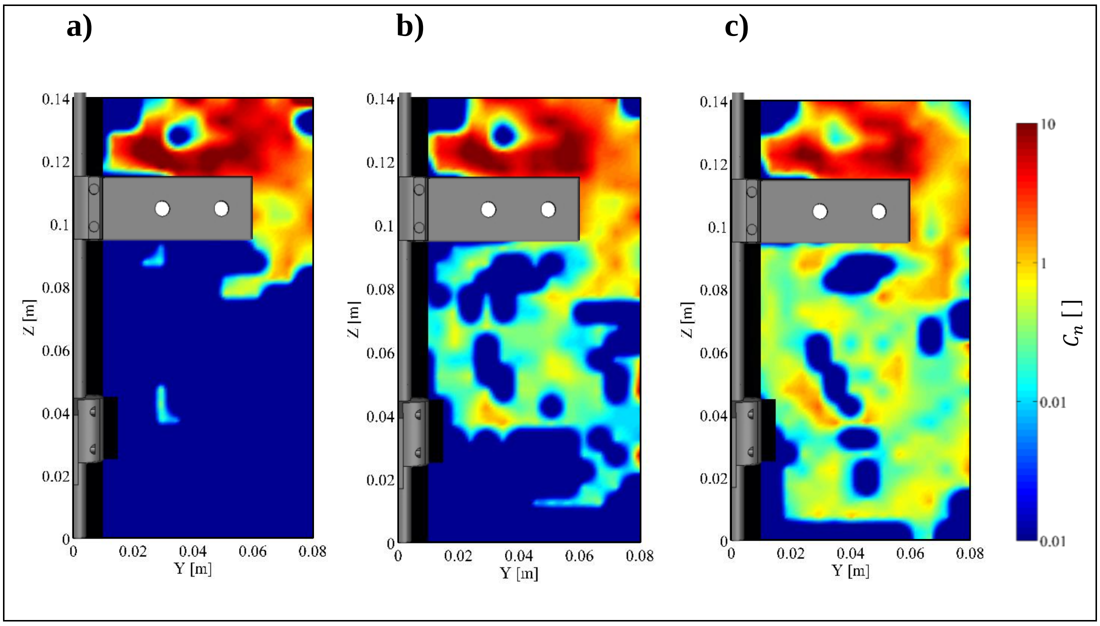

Figure 5. 6. Concentration profiles for case 2 shown in Table 5. 1 at a) 10, b) 25, and c) 40 seconds for the particle tracking approach

The low image resolution observed in Figure 5. 6 is the result of visualising 3D computational results in a 2D grid; here only the information on a very narrow plane which corresponds to approximately 1% of the volume of the tank is used, and consequently, 99% of the particles do not provide any information. For this reason, the three-dimensional discretisation is a much better approach to estimate the mixing time (as mentioned in Section 5.3.1.1), and Figure 5. 6 is only presented for completeness of the discussion.

To better understand the mixing using the Lagrangian scheme, it is useful to plot the evolution of the number of particles in the elements of the 3D discretised grid (Figure 5. 7). As it can be seen, initially, all particles are found in a small number of boxes (located at the top of the tank). As time progresses the particles spread within the mixing tank and progressively, more cells contain an increasing number of particles. A pseudo steady state is achieved at approximately 160 seconds. It is clear, however, that not all boxes have the same number of particles, but the number of boxes containing a certain number of particles is constant over time. This suggests that some particles travel as a cluster, meaning that diffusion (represented by the random walk term in equation 5.6) has a minor effect on this simulation, and mixing is dominated by convection.

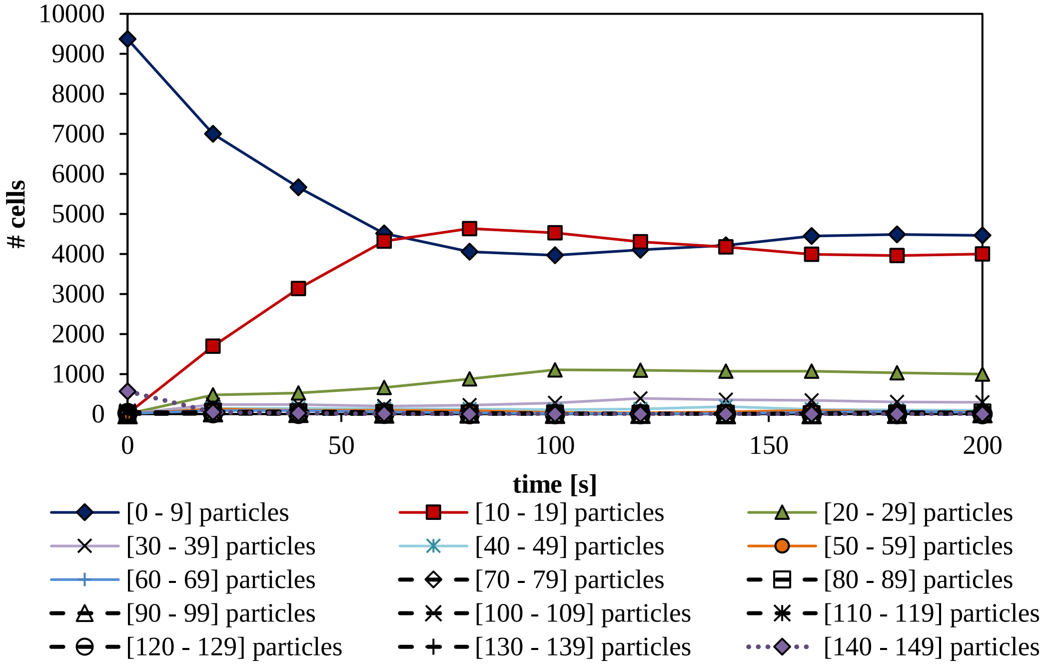

Figure 5. 7. Number of particles in the 3D discretised elements as a function of time for case 2 shown in Table 5. 1

5.4.1.4. Comparison of methodologies

The normalised standard deviation of the concentration profiles was calculated and plotted over time in Figure 5. 8 for all the experimental and numerical results obtained. Mixing is considered complete when the standard deviation reaches a plateau where $\sigma_N \rightarrow 0$. Because of the high variability of the experimental results, the data was filtered (with the sgolayfilt function in Matlab) to obtain a smooth curve, and both sets of data can be seen in Figure 5. 8. The resulting experimental mixing time and the computational one obtained using the particle tracking method are summarised in Table 5. 2. As it is possible to see in Figure 5. 8, there was not enough time to complete any entire CFD simulation.

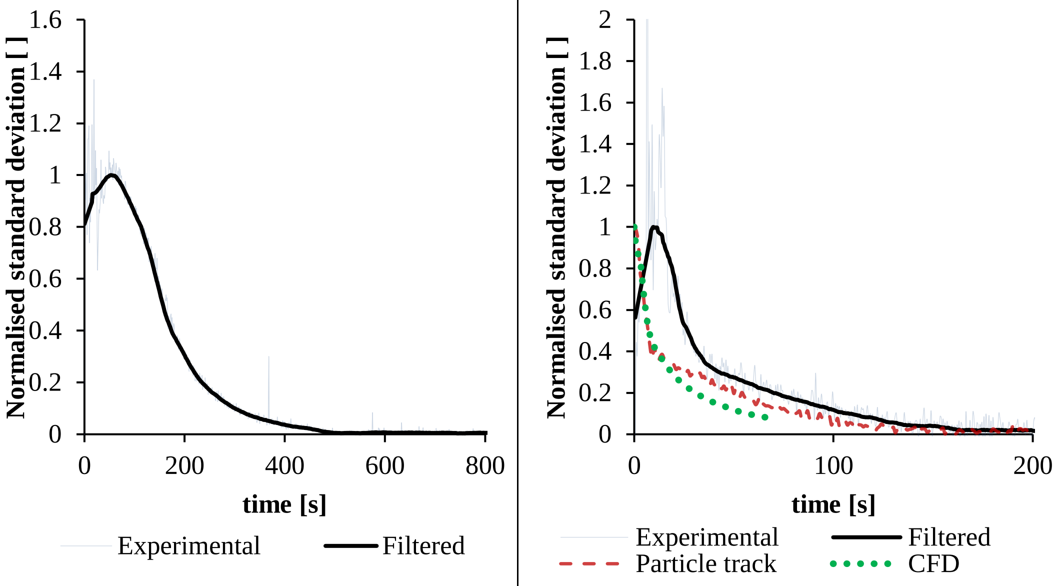

a) Case 1: Glycerol 30 rpm

b) Case 2: Glycerol 60 rpm

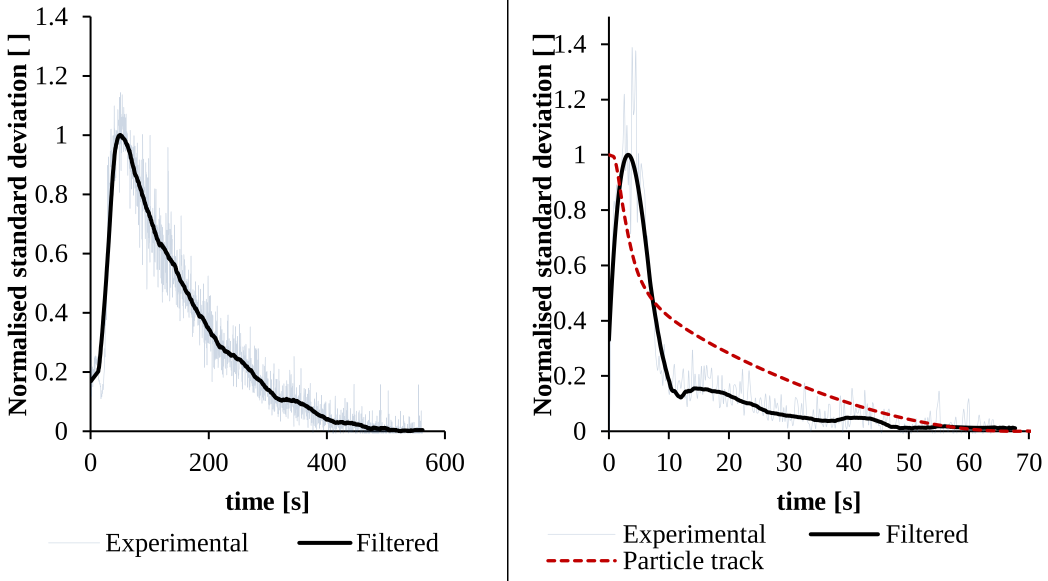

c) Case 3: Gel 20%wt 80 rpm

d) Case 4: Gel 20%wt 140 rpm

Figure 5. 8. Normalised standard deviation of the concentration profiles for all four cases presented in Table 5. 1

Table 5. 2. Experimental and computational mixing times

Case	Experimental mixing time [s]	Computational mixing time [s]	Difference [%]
1	500		
2	165	155	6%
3	450		
4	50	60	20%

For any mixing process, using the PLIF technique, the normalised standard deviation should start at a value equal to zero at time zero (prior to tracer injection), then, increase immediately because of the injection of the tracer to a maximum value of one (because of the normalisation), followed by a slow decrease as time progresses. However, in all experimental results presented in Figure 5. 8 the standard deviation increases progressively to its maximum value of one, and then decreases until the final plateau is reached. This happens because during the processing of the experimental results the upper part of the tank above the top blade of the impeller was masked. This part of the vessel initially contains most of the tracer. As mixing progresses the tracer moves away from the top of the tank to the un-masked section of the plane: hence, the standard deviation increases initially. Later on, as the concentration in the vessel becomes more homogeneous, the standard deviation starts to decrease.

The results obtained with the Lagrangian scheme, even though being preliminary are comparable with the experimental ones as shown in Table 5. 2. As expected, the non-Newtonian case (case 4) has a greater difference than the Newtonian one (case 2) when the computational results are compared with the experimental ones. Most likely, these discrepancies are consequence of not having used the adequate number of particles and the size of the averaging volumes.

5.4.2. Mixing efficiency

Laminar mixing might be as effective as turbulent mixing, although it is often significantly slower (Paul et al., 2004). Laminar mixing is currently best described from a dynamical systems perspective (Ottino, 1989), and it is achieved by a series of consecutive folding and stretching operations that increase the intermaterial contact area exponentially. Because of current computational limitations, simulating complete laminar mixing processes is often impractical, and alternative methods are commonly used to evaluate mixing efficiency; these are Poincaré maps and Stretching fields.

5.4.2.1. Poincaré maps

In a three-dimensional flow, a Poincaré map is a representation of the intersection of massless particles placed into the flow with a Poincaré section, which is a surface perpendicular to the main direction of the flow (Paul et al., 2004). Poincaré maps can be used to provide information on the performance of impellers, and help to identify compartmentalised zones, such as stagnant areas, in a stirred tank.

Theoretically, Poincaré maps should be constructed by positioning a single massless particle in the chaotic region of the domain (as presented in section 2.4.3.4, a location is considered chaotic if an infinitesimally small vector that is initially placed on it exponentially grows as time progresses). If the particle is injected at any point of a chaotic region that is bounded by stagnant zones, as time approaches infinity, the particle should have visited the entire chaotic region, and consequently, that of the subspace of interest: the Poincaré section.

In a Poincaré map, particle intersections with the Poincaré section are presented as black dots. Consequently, clouds of random black dots indicate the space comprised by the chaotic zone in a 2D space. In contrast, white areas of the map indicate presence of stagnant (or regular) zones.

Although Poincaré maps provide relevant qualitative information about the performance of the mixer, they also present severe limitations. If, for instance, the flow consists of multiple compartmentalised chaotic zones separated by stagnant zones, and a single particle is injected to construct the Poincaré map, at best, it will only reveal one of the chaotic regions, as the particle will not be able to move across the stagnant areas. Moreover, Poincaré maps do not give quantitative information about how good or bad a mixer is, or how long it takes to reach a desired degree of mixing; it can only be used to find the profile of the chaotic region.

In the current study, a total of 624 particles were placed near the blades of the tank in high velocity regions (corresponding to 13 equidistant vertical positions from 0.05 to 0.135 m, 12 angular positions, one aligned with the blade and two additional positions at ± 1º, for each blade, and 4 equidistant radial positions from 0.061 to 0.067 m), to create the Poincaré maps. Particles were tracked using the convective part of Eq. 5. 6 for 5000 impeller revolutions. The number of particles used is similar and smaller than in other studies (Zalc et al., 2002, Alvarez et al., 2002).

Every time a particle crossed the middle plane (XZ plane) of the vessel, its position was captured and recorded in the Poincaré plot. Poincaré maps were constructed for the four cases shown in Table 5. 1, and they are presented in Figure 5. 9. Particles that intersected the central plane (YZ) are indicated as black dots.

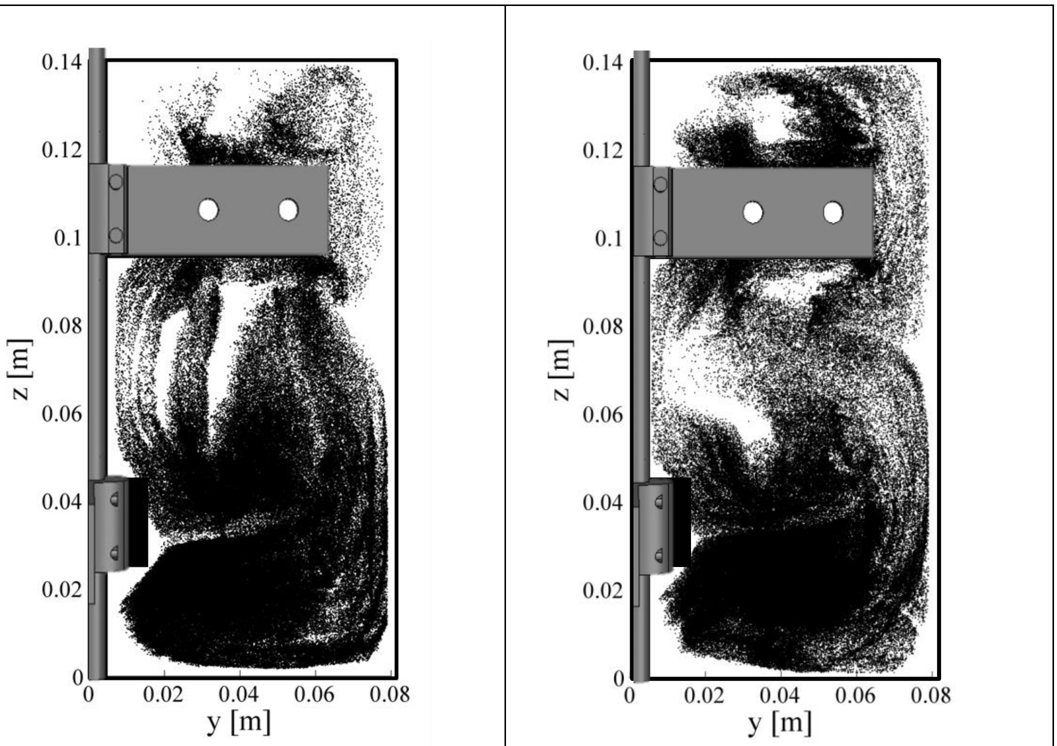

a) Case 1: Glycerol 30 rpm 24 ºC

b) Case 2: Glycerol 60 rpm 24 ºC

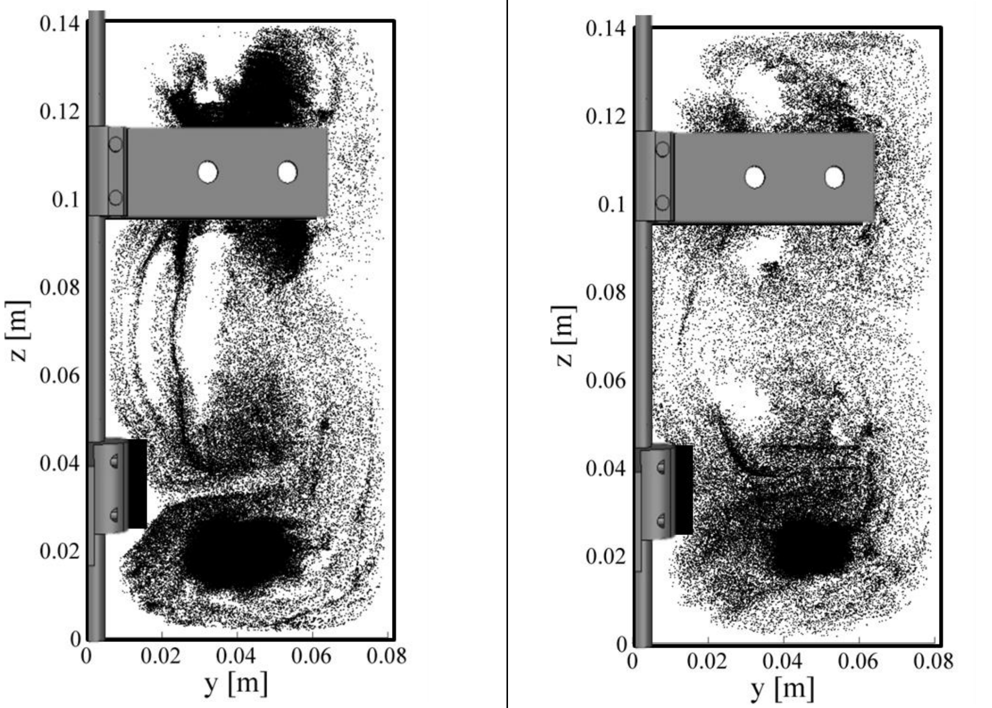

c) Case 3: Gel 20% 80 rpm 52 ºC

d) Case 4: Gel 20% 140 rpm 52 ºC

Figure 5. 9. Poincaré maps of the four cases shown in Table 5. 1

In all four cases shown in Figure 5. 9, there are combinations of segregated (or regular) regions (i.e., islands) that appear as empty regions, and areas of chaotic motion, which appear as a random cloud of points. In Figure 5.9, the chaotic mixing zones appear near the blades and in most of the space between the blades. In contrast, the regular zones are found near the bottom and the lateral walls of the tank, and near the free surface of the liquids. Other regular regions are found adjacent to the shaft of the impeller, above the top blade, and below the low blade.

As can be seen, the configuration of the Poincaré map is mostly affected by the Reynolds number (shown in Table 5. 1), and less by the rheological properties of the fluid; for instance, if Figure 5. 9 a) and c) are compared, it is possible to see that the chaotic and segregated zones of their respective Poincaré maps are very similar, both Reynolds number are similar as well, but the rheological properties of the fluids used are completely different. By increasing the Reynolds number, the striations formed in the space between the blades disappear into a single regular zone. Additionally, at high Reynolds numbers, the chaotic region expands closer to the walls of the tank.

Although the rheological properties do not seem to affect the general structure of the map, if Figure 5. 9 a) and c) are compared again, it is possible to see that in the Newtonian case, the black cloud of particles defining the chaotic zone is homogeneously distributed across the map, while in the non-Newtonian case, particles present preferential intersection locations with the Poincaré map (indicated by an intense black colour), mainly found just below the lower blade and above the top one.

From these Poincaré maps, it is possible to conclude that the impeller minimises the presence of stagnant zones, which is mainly affected by the Reynolds number regardless of the fluid. No information about how efficiently the mixer performs can be derived.

5.4.2.2. Stretching fields

The mixing efficiency can be related to the potential of the impeller to stretch the fluid. From a Eulerian perspective, a fluid filament can be represented as an infinitesimally small vector ($\mathbf{l}_0$) initially located at point $\mathbf{x}_0$. The time evolution of the vector **l** can be calculated as (Muzzio et al., 1991, Alvarez et al., 2002):

$$\frac{d\mathbf{l}}{dt} = (\nabla\mathbf{v})^T \cdot \mathbf{l}, \tag{Eq. 5.8}$$

where $\mathbf{v}$ is the velocity vector. The elongation of the fluid element is related to the magnitude of $\mathbf{l}$. The accumulated stretch of the fluid element (λ) is calculated as (Muzzio et al., 1991):

$$\lambda(t) = \frac{|\mathbf{l}(t)|}{|\mathbf{l}_0|} \tag{Eq. 5.9}$$

Equation 5.9 indicates that the accumulated stretch that a fluid element has experienced at time *t* is equal to the elongation that it has experienced over the same time divided by the initial length of the element.

High values of stretching indicate high elongation of the fluid element, and hence, high distance between the two extremes. This is aligned with the definition of deterministic chaos: rapid divergence from small difference in initial conditions. Hence, chaotic flows have positive stretching values. By placing these fluid elements intelligently on the flow, one can determine effective injection locations, or in other words, locations that provide fast mixing.

The elongation of the fluid element can also be calculated using a Lagrangian approach. In this case, the fluid element is seen as the straight line between two massless particles. Each massless particle moves at the local fluid velocity, and the elongation is computed as the distance that separates the pair of massless particles at different times. The standard method described by equations 5.8 and 5.9 was compareed with the Lagrangian tracking in a simple two-dimensional linear shear flow, and in a simple two-dimensional rotational shear flow (Appendix V), and it was found that they are equivalent.

Lagrangian tracking of massless particles was used to compute the stretching maps. 2,200 equally dispersed particles were introduced on the YZ plane of the tank. I will refer to them as central (massless) particles. For each central particle introduced into the flow, six additional particles were also placed; one for each positive and negative Cartesian coordinate. I will refer to these as peripheral (massless) particles. The total number of fluid elements (or pairs of particles) used is larger than in other studies (Iranshahi et al., 2006).

It is necessary that the initial length of the fluid element is infinitesimally small, so that the accumulated stretch it experiences increases exponentially as function of time. It is clear that the maximum stretch that a fluid element can experience at any given time is dictated by the size of the flow domain (in this case a cylinder of 14 cm height and 8 cm radius) and the initial length of the fluid element:

$$\lambda_{\max} = \frac{\sqrt{0.16^2 + 0.14^2}}{l_0^2} \qquad \text{(Eq. 5.10)}$$

In addition, the smaller the initial size of the fluid element is, the longer it will take for it to reach to the maximum stretch within the domain. This is key for the success of this methodology, as the final goal is to calculate the topological entropy, which is assessed at $t \rightarrow \infty$ (Paul et al., 2004).

In the simulations, all the peripheral particles were placed at a distance of 10^{-10} m from the central particle. In other studies, this distance was set at 10^{-6} [m] (Iranshahi et al., 2007), or it was not specified at all (Muzzio et al., 1991, Alvarez et al., 2002, Zalc et al., 2002). Greater initial distances between central and peripheral particles were also tested: 10^{-6} [m] and 10^{-8} [m], but in these two cases, the maximum stretch for most of the particles was reached after only 10 and 20 revolutions respectively.

The stretching maps for all four cases after 200 periods (or 100 revolutions) are shown in Figure 5. 10.

The stretching maps after 200 periods reveal predominant chaotic regions in the central plane of the tank indicated by high values of λ. At high Reynolds numbers, (cases b) and d)), the stretching values are significantly higher in the upper part of the tank ($z \geq 0.08$ m) compared to the rest of the tank. This is not observed at lower Reynolds numbers. In case a), the highest values of λ are located in the space between the upper and lower impeller blades, and in case c), λ is significantly more homogenous over the plane compared to the other three cases. In all cases, regions of regular flow (those with $\lambda \approx 1$) are found along the tank wall ($y \approx 0.08$ m), and they are significantly larger at heights corresponding to the height of blades, and at the bottom right corner of the map.

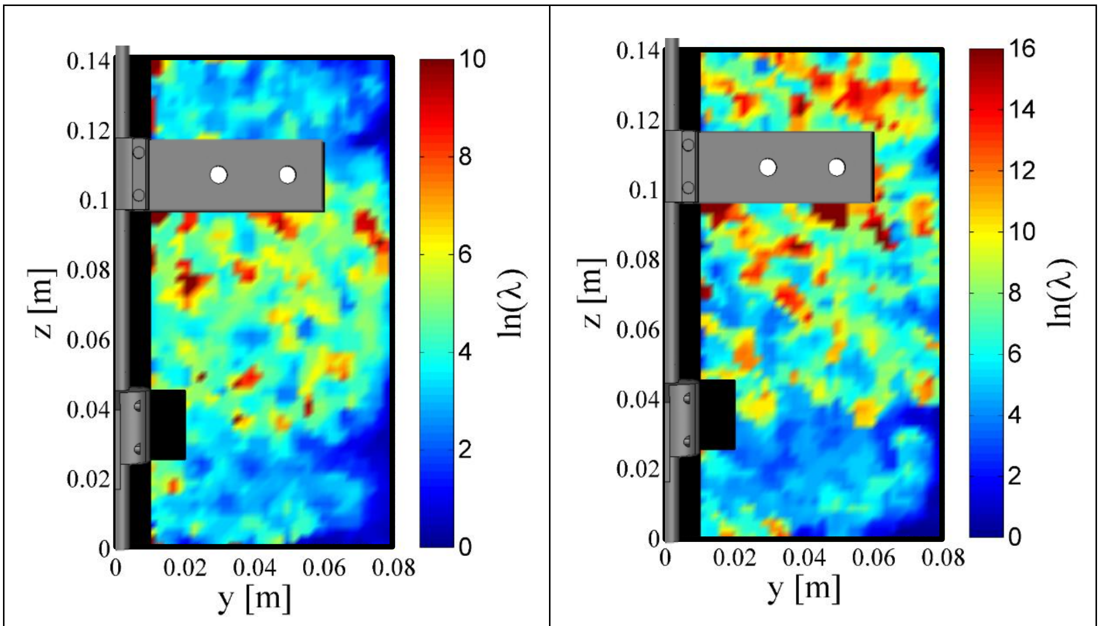

a) Glycerol 30 rpm **b) Glycerol 60 rpm**

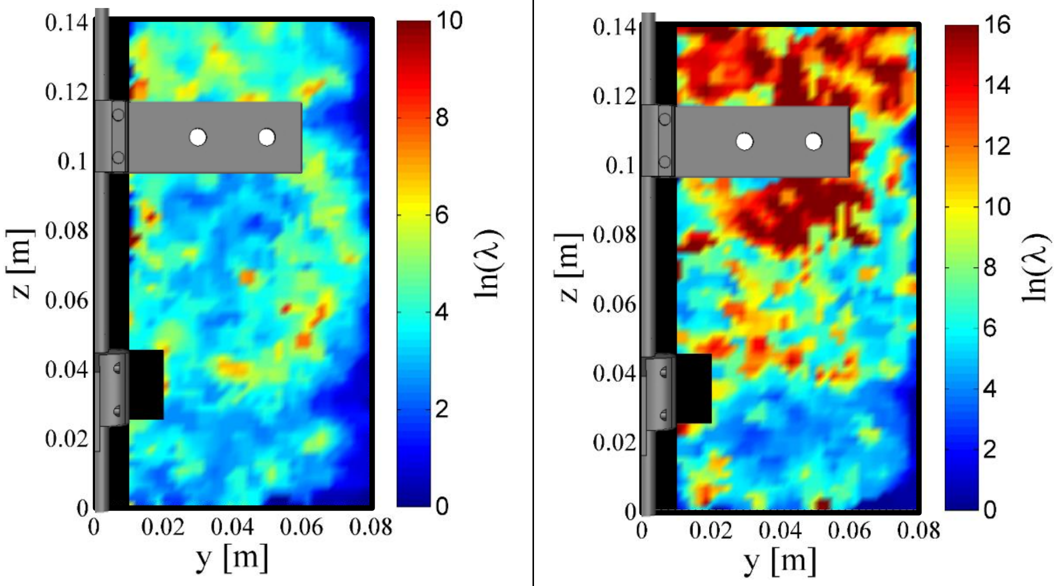

c) Gel 20% wt. 80 rpm **d) Gel 20% wt. 140 rpm**

Figure 5. 10. Stretching maps after 200 periods for all four cases shown in Table 5. 1

The mixing efficiency can be correlated to both the geometric and the arithmetic mean rates of stretching in chaotic flows represented by equations 2.44 and 2.45 respectively:

$$\langle\lambda\rangle = \left(\prod_{\mathrm{i}=1}^{N_p} \lambda_{\mathrm{i}}\right)^{\frac{1}{N_p}} \sim \mathrm{e}^{\Lambda n} \qquad \text{(Eq. 2.44 bis)}$$

$$\bar{\lambda} = \sum_{\mathrm{i}=1}^{N_p} \frac{\lambda_{\mathrm{i}}}{N_p} \sim \mathrm{e}^{\Theta n} \qquad \text{(Eq. 2.45 bis)}$$

where *Np* is the number of pairs of particles introduced in the flow, and *n* is the number of periods of flow. Λ and Θ are known as the Lyapunov exponent and the topological entropy, respectively (Paul et al., 2004).

The Lyapunov exponent has been used extensively to determine the rate of intermaterial area growth in chaotic mixing processes. However, computational studies have shown that the Lyapunov exponent underpredicts the true exponential rate of area growth, and that the topological entropy predicts more accurately this parameter (Alvarez et al., 1998, Muzzio et al., 2000). The topological entropy can be used to quantify mixing efficiency by indicating the increase over time of the interfacial area available between the fluids that are mixed. It is important to note that there is no reference value to quantify good mixing. Instead, topological entropy is used to compare mixing at different conditions for a specific mixer. Figure 5. 11 illustrates the evolution of $\bar{\lambda}$ as a function of the time periods (equivalent to half impeller revolution) for the four cases studied.

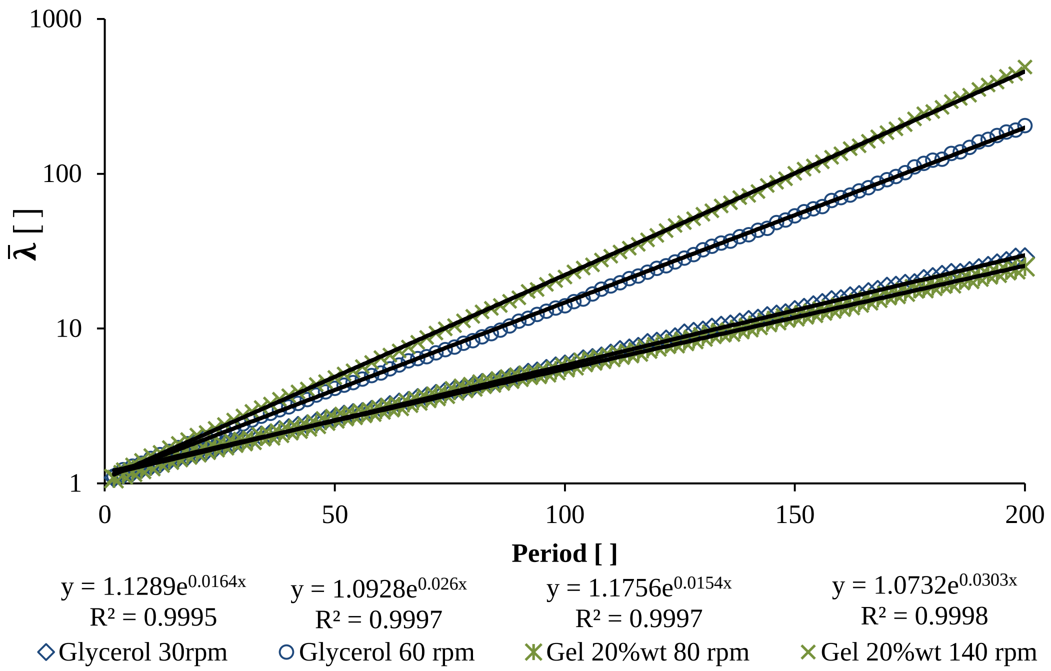

Figure 5. 11. evolution of $\bar{\lambda}$ as function of the time periods

As can be seen in Figure 5. 11, all four sets of $\bar{\lambda}$ increase linearly in a semi-logarithmic plot as function of time period with regression coefficients greater than 0.999. This is a characteristic feature of chaotic flows (Muzzio et al., 1991, Zalc et al., 2002). It can be seen that, for the flow conditions covered in this study, for each fluid increasing the impeller speed translates into better mixing. If both fluids are considered simultaneously, one can see that an increase in Reynolds number translates to an increase in the topological entropy.

5.5. Conclusions

In this chapter, the mixing properties of a vessel equipped with a dual impeller with four flat blades were investigated in the laminar regime. The flow field had been previously discussed. The images obtained experimentally using the PLIF technique revealed that mixing is achieved by periodic operations of stretching and folding of the materials, which is a common feature of laminar mixing. The CFD simulations were able to reproduce the convective mixing, but the details of the concentration profile were lost. This indicates that finer grids are required when implementing the transport of species equation.

A preliminary attempt to model the mixing process using a Lagrangian particle tracking approach was conducted. The mixing time predictions were comparable with the experimental results for both cases studied, although further research is needed in this direction to determine the real success of this approach.

The mixing structures were computed for glycerol and for a mixture of glycerol and a carbomer gel with Reynolds numbers ranging from 8 to 25. The Poincaré maps revealed that in all four cases, the main bulk of the tank was able to provide chaotic mixing, and regular zones were found near the walls of the tank and near the free surface of the liquids. The analysis of the stretching fields showed that the mixing efficiency is correlated to the Reynolds number; the mixing efficiency is the greatest for case 4 (Re = 26.8) followed by case 2 (Re = 18.8), while cases 1 and 3 are almost identical (Re= 9.42 and 9.94, respectively).

6. Conclusions

In this chapter, the findings of the three results chapters are highlighted and then recommendations for future research are presented.

6.1. Final remarks

Mixing of complex non-Newtonian fluids is common in industrial processes, and optimal design and operational criteria are often based on experience rather than scientific insight. Computational fluid dynamics is identified as a powerful tool to assist the design of such processes. The objective of this research was to develop a CFD model to study the mixing of glycerol with a carbomer gel made of carbomer and Polyethylene glycol, which is a critical step in the manufacturing of non-aqueous toothpastes. The main advantages of this include the identification of high shearing zones that can damage the product and of stagnant zones where no effective mixing happens. The necessary mixing time could also be studied for different fluid mixtures and rotation speeds.

In Chapter 2, the relevant literature for this research was summarised. It was found that CFD models have been implemented in the past to study mixing tanks, and typically, these studies focus on at least one of the following areas: (i) calculation of the power requirement for agitation, (ii) study of the velocity profiles generated by different types of mixers and hence identification of their suitability for mixing, and (iii) estimation of mixing time. In all cases, the validation of the CFD models was fundamental to ensure the trustworthiness of the results.

In Chapter 3, a CFD model of a simple stirred tank to model the flow behaviour of different mixtures of the glycerol and carbomer gel was implemented. The rheological properties of the mixtures of these two fluids were comprehensively studied to provide the CFD model with an adequate constitutive equation for the viscosity. The CFD model was validated against accurate experimental results of power consumption obtained in a stirred vessel equipped with a frictionless air bearing and a load cell. As it was expected, the power consumption of the mixer increased as the gel mass fraction and the impeller speed increased and as the temperature decreased.

The gel is a viscoelastic material. Above a certain magnitude of the shear stress, the viscous behaviour of the material dominates over the elastic one. In all cases studied, the average magnitude of the shear stress of the impeller was above that threshold. At gel mass fractions below 20% wt., the elastic behaviour is negligible. The rheological models used in Chapter 3 are the shear thinning and the Herschel-Bulkley ones. Both rheological models gave similar results.

Chapter 3 set a solid ground to understand the applicability of CFD to model complex fluids in stirred tanks to increase the complexity of the mixing system towards a more geometrically similar version to the real mixer.

In Chapter 4, a simplified scaled down version of a pilot plant mixer was developed, keeping the main features similar. The agitator consisted of long flat blades with holes on them, while the external impeller of the industrial vessel was substituted by two baffles. The ratio of the diameter of the agitator over the diameter of the tank, and the ratio of the diameter of the scraper and the diameter of the tank were maintained in the model mixer.

A CFD model to study the fluid dynamics in the laboratory-scale mixer was implemented. The impeller performance was assessed both qualitatively and quantitatively. Velocity streamlines were calculated, which revealed that the impeller generates strong angular motion compared with the axial and radial components. Then, the regions in which the fluid is agitated more vigorously (with higher velocity) were identified, and the percentage of the fluid that has speeds above given thresholds was quantified. I concluded with this study that the impeller minimizes stagnant zones but most of the fluid has a velocity ten times smaller than that of the tip of the blade. This situation is worsened for fluids with higher viscosity and higher shear thinning behaviour (e.g. 20% gel). The effect of the holes in the fluid flow was evaluated; they increase the shear rate locally by increasing the perimeter of the edges of the impeller, which is positive for shear thinning fluids.

The simulations were validated with the PIV technique. The experimental errors were thoroughly assessed and presented in the form of error bars. The interrogation error was found to be the most significant in this case. The maximum uncertainty when comparing the computational and experimental results was also evaluated. Overall, experiments and simulations agreed quite well. This study intended to demonstrate the importance of performing careful studies when designing mixers to deal with complex fluids.

In Chapter 5, the PLIF technique was used to investigate the mixing time in glycerol and glycerol (80% wt.)/carbomer gel (20% wt.) solutions, using a fluorescent tracer in the laboratory-scale mixer described in Chapter 4. The PLIF images revealed that mixing is achieved by periodic operations of stretching and folding of the materials, which is a common feature of laminar mixing.

The CFD model developed in Chapter 4 was used to investigate the mixing time for four cases: a glycerol solution and a mixture of glycerol with the carbomer gel at two different impeller speeds each in the laminar regime. The CFD model was modified to include the transport of species equation, and it was used to simulate the transient mixing process of glycerol with a tracer. The simulations were far too computationally expensive because of the timeframe of the real mixing process, while the mixing structures were captured with low resolution. The simulated mixing process was faster than in reality, which indicates that a finer grid is needed if this approach is to be pursued.

An alternative Lagrangian scheme was also used to evaluate the mixing time. The CFD grid was discretised with 10,080 elements of the same size, and 100,800 massless particles were placed into the flow at the top of the vessel. The number of particles was counted on each element over time. The overall mixing pattern observed was similar to the experimental one, but the resolution of this method was also low, and the mixing structures were not possible to be observed in detail. Additionally, the number of particles and the size of the elements have a direct impact on the predicted mixing time, and a systematic study is needed to determine the number of cell elements and particles for the predicted mixing time to be independent of these two variables.

As the Reynolds numbers of all cases studied in Chapter 5 are low, the mixing was considered to happen in the laminar regime. Poincaré maps and stretching fields were plotted for all cases studied. The Poincaré maps revealed that in all four cases considered, the main bulk of the tank provides chaotic mixing, and regular zones with little mixing were found near the walls of the tank and near the free surface of the liquids. The analysis of the stretching fields showed that the mixing efficiency is correlated to the Reynolds number independently of the fluid used.

6.2. Suggestions for further research

This work originated from the industrial need of understanding the mechanisms of mixing complex fluids, and it helps to better understand this particular process. In this research, CFD has been used as a tool to obtain relevant knowledge of the mixing process of glycerol and carbomer gel, and experimental work has been conducted to validate the different models implemented in CFD.

Overall, CFD has proven to be successful in applications where steady state models can be used. Transient simulations were also conducted with CFD, but the need of using very fine grids for long processes increased prohibitively the computational cost and time. This is precisely the case of laminar mixing. For this reason, it is recommended to redefine the approach of the study towards one more experimentally based.

If the computational approach is to be pursued, a more systematic methodology is needed. For the Eulerian perspective, it would be necessary to conduct a study to find an independent grid for the transport of species equation. This should minimise the presence of numerical diffusion, and help the visualisation of the mixing structures. For the Lagrangian case, a systematic methodology to determine the minimum number of particles to inject to the flow, and the number and size of the elements to calculate the concentration of the particles, and subsequently the tracer, are needed.

For future experiments and simulations, it is recommended to build an exact scale-down version of the mixer used in the industrial process, as the results would be even more relevant for the industrial purpose. This is a rather challenging task because of the coaxial impeller and of the conical shape of the bottom of the tank. Nevertheless, it would be the next step towards the investigation of the real mixing process, and it would potentially help to identify optimal operating conditions of the real mixer.

In contrast, alternative mixing processes of the fluids studied in this thesis, such as static mixers, are also relevant research topics. A comparative study of the different mixing strategies in terms of mixing time and rheological properties of the final product would provide valuable insight towards the optimisation of the process.

Finally, the manufacturing of toothpastes is a process with several mixing stages. In this thesis I have studied one of them, which is early in the flowchart and it is a critical one in terms of processing time, but the subsequent stages are even more complex because of the addition of solids into the mixture. In particular, it would be interesting to investigate the fundamentals mechanisms of mixing highly viscous non-Newtonian fluids with high loads of polydisperse solid particles.

References

ADAMS, L. & BARIGOU, M. 2007. CFD analysis of caverns and pseudo-caverns developed during mixing of non-Newtonian fluids. *Chemical Engineering Research and Design*, 85**,** 598-604.

ADRIAN, R. J. & WESTERWEEL, J. 2011. *Particle image velocimetry*, Cambridge University Press.

ALVAREZ, M. M., MUZZIO, F. J., CERBELLI, S., ADROVER, A. & GIONA, M. 1998. Self-similar spatiotemporal structure of intermaterial boundaries in chaotic flows. *Physical Review Letters*, 81**,** 3395-3398.

ALVAREZ, M. M., ZALC, J. M., SHINBROT, T., ARRATIA, P. E. & MUZZIO, F. J. 2002. Mechanisms of mixing and creation of structure in laminar stirred tanks. *Aiche Journal*, 48**,** 2135-2148.

AMANULLAH, A., HJORTH, S. A. & NIENOW, A. W. 1997. Cavern sizes generated in highly shear thinning viscous fluids by SCABA 3SHP1 impellers. *Food and Bioproducts Processing*, 75**,** 232-238.

AMEUR, H. 2015. Energy efficiency of different impellers in stirred tank reactors. *Energy*, 93**,** 1980-1988.

ANDERSON, J. D. & WENDT, J. 1995. *Computational fluid dynamics*, Springer.

ANTON-PAAR 2009. The Modular Rheometer Series. *In:* MCR, P. (ed.).

AREF, H. 1984. Stirring by Chaotic Advection. *Journal of Fluid Mechanics*, 143**,** 1-21.

AREF, H. 2002. The development of chaotic advection. *Physics of Fluids*, 14**,** 1315-1325.

ARRATIA, P. E., KUKURA, J., LACOMBE, J. & MUZZIO, F. J. 2006. Mixing of shear-thinning fluids with yield stress in stirred tanks. *Aiche Journal*, 52**,** 2310-2322.

ASCANIO, G. 2015. Mixing time in stirred vessels: A review of experimental techniques. *Chinese Journal of Chemical Engineering*, 23**,** 1065-1076.

ASCANIO, G., CASTRO, B. & GALINDO, E. 2004. Measurement of power consumption in stirred vessels - A review. *Chemical Engineering Research & Design*, 82**,** 1282-1290.

BARRY, B. & MEYER, M. 1979. The rheological properties of carbopol gels I. Continuous shear and creep properties of carbopol gels. *International journal of pharmaceutics*, 2**,** 1-25.

BATES, R., FONDY, P. L. & CORPSTEIN, R. 1963. Examination of some geometric parameters of impeller power. *Industrial & Engineering Chemistry Process Design and Development*, 2**,** 310-314.

BAUMANN, K. H. & MÜHLFRIEDEL, K. 2002. Mass Transfer Studies with Laser-Induced Fluorescence across Liquid/Liquid Phase Boundaries. *Chemical engineering & technology*, 25**,** 697-700.

BIRD, R. B. 2002. Transport phenomena. *Applied Mechanics Reviews*, 55**,** R1-R4.

BLAUSEN-GALLERY. 2014. *Tooth Anatomy* [Online]. Blausen.com: Wikiversity Journal of Medicine. [Accessed January 2016].

BONACUCINA, G., MARTELLI, S. & PALMIERI, G. F. 2004. Rheological, mucoadhesive and release properties of Carbopol gels in hydrophilic cosolvents. *International Journal of Pharmaceutics*, 282**,** 115-130.

BULNES-ABUNDIS, D. & ALVAREZ, M. M. 2013. The simplest stirred tank for laminar mixing: Mixing in a vessel agitated by an off-centered angled disc. *Aiche Journal*, 59**,** 3092-3108.

CHAPPLE, D., KRESTA, S., WALL, A. & AFACAN, A. 2002. The effect of impeller and tank geometry on power number for a pitched blade turbine. *Chemical Engineering Research and Design,* 80**,** 364-372.

CHHABRA, R. P. & RICHARDSON, J. F. 2011. *Non-Newtonian flow and applied rheology: engineering applications*, Butterworth-Heinemann.

CORONEO, M., MONTANTE, G., PAGLIANTI, A. & MAGELLI, F. 2011. CFD prediction of fluid flow and mixing in stirred tanks: Numerical issues about the RANS simulations. *Computers & Chemical Engineering,* 35**,** 1959-1968.

CORTADA-GARCIA, M., DORE, V., MAZZEI, L. & ANGELI, P. 2017. Experimental and CFD studies of power consumption in the agitation of highly viscous shear thinning fluids. *Chemical Engineering Research and Design,* 119**,** 171-182.

CORTADA-GARCIA, M., WEHELIYE, W. H., DORE, V., MAZZEI, L. & ANGELI, P. 2018. Computational fluid dynamic studies of mixers for highly viscous shear thinning fluids and PIV validation. *Chemical Engineering Science,* 179**,** 133-149.

COUERBE, G., FLETCHER, D. F., XUEREB, C. & POUX, M. 2008. Impact of thixotropy on flow patterns induced in a stirred tank: Numerical and experimental studies. *Chemical Engineering Research & Design,* 86**,** 545-553.

COUSSOT, P., NGUYEN, Q. D., HUYNH, H. T. & BONN, D. 2002. Avalanche behavior in yield stress fluids. *Physical Review Letters,* 88.

COUSSOT, P., TOCQUER, L., LANOS, C. & OVARLEZ, G. 2009. Macroscopic vs. local rheology of yield stress fluids. *Journal of Non-Newtonian Fluid Mechanics,* 158**,** 85-90.

D'ERRICO, G., ORTONA, O., CAPUANO, F. & VITAGLIANO, V. 2004. Diffusion coefficients for the binary system glycerol plus water at 25 degrees C. A velocity correlation study. *Journal of Chemical and Engineering Data,* 49**,** 1665-1670.

DANCKWERTS, P. V. 1952. The definition and measurement of some characteristics of mixtures. *Applied Scientific Research, Section A,* 3**,** 279-296.

DENTON, J. & SINGH, U. Time marching methods for turbomachinery flow calculation. In Von Karman Inst. for Fluid Dyn. Appl. of Numerical Methods to Flow Calculations in Turbomachines 47 p (SEE N80-12365 03-34), 1979.

FARHAT, M., FRADETTE, L. & TANGUY, P. A. 2008. Revisiting the performance of a coaxial mixer. *Industrial & Engineering Chemistry Research,* 47**,** 3562-3567.

FISCHMAN, S. 1992. Hare's teeth to fluorides, historical aspects of dentifrice use. *Clinical and Biological Aspects of Dentifrices. New York, Oxford Medical Publications***,** 1-7.

FISCHMAN, S. L. 1997. The history of oral hygiene products: how far have we come in 6000 years? *Periodontol 2000,* 15**,** 7-14.

FOUCAULT, S., ASCANIO, G. & TANGUY, P. A. 2004. Coaxial mixer hydrodynamics with Newtonian and non-Newtonian fluids. *Chemical Engineering & Technology,* 27**,** 324-329.

FRADETTE, L., THOME, G., TANGUY, P. A. & TAKENAKA, K. 2007. Power and mixing time study involving a Maxblend (R) impeller with viscous Newtonian and non-Newtonian fluids. *Chemical Engineering Research & Design,* 85**,** 1514-1523.

GREEN, D. W. 2008. Perry's chemical engineers' handbook. *McGraw-Hill, New York, Section,* 8**,** 48-49.

GSK 2015. Annual Report 2014.

HALL, J. F., BARIGOU, M., SIMMONS, M. J. H. & STITT, E. H. 2004. Mixing in unbaffled high-throughput experimentation reactors. *Industrial & Engineering Chemistry Research,* 43**,** 4149-4158.

HARMAN, R. J. 2001. *Handbook of pharmacy health education*, Pharmaceutical Press.

HENCH, L. L. 2006. The story of Bioglass. *J Mater Sci Mater Med,* 17**,** 967-78.

HOUCINE, I., VIVIER, H., PLASARI, E., DAVID, R. & VILLERMAUX, J. 1996. Planar laser induced fluorescence technique for measurements of concentration fields in continuous stirred tank reactors. *Experiments in Fluids,* 22**,** 95-102.

HURTADO, F. J., KAISER, A. S. & ZAMORA, B. 2015. Fluid dynamic analysis of a continuous stirred tank reactor for technical optimization of wastewater digestion. *Water Research,* 71**,** 282-293.

IRANSHAHI, A., DEVALS, C., HENICHE, M., FRADETTE, L., TANGUY, P. A. & TAKENAKA, K. 2007. Hydrodynamics characterization of the Maxblend impeller. *Chemical engineering science,* 62**,** 3641-3653.

IRANSHAHI, A., HENICHE, M., BERTRAND, F. & TANGUY, P. A. 2006. Numerical investigation of the mixing efficiency of the Ekato Paravisc impeller. *Chemical Engineering Science,* 61**,** 2609-2617.

IRWIN, C. R. & MCCUSKER, P. 1997. Prevalence of dentine hypersensitivity in a general dental population. *J Ir Dent Assoc,* 43**,** 7-9.

ISLAM, M. T., RODRIGUEZ-HORNEDO, N., CIOTTI, S. & ACKERMANN, C. 2004. Rheological characterization of topical carbomer gels neutralized to different pH. *Pharmaceutical Research,* 21**,** 1192-1199.

JAWORSKI, Z., NIENOW, A. & DYSTER, K. 1996. An LDA study of the turbulent flow field in a baffled vessel agitated by an axial, down-pumping hydrofoil impeller. *The Canadian Journal of Chemical Engineering,* 74**,** 3-15.

KARASSO, P. S. & MUNGAL, M. G. 1997. PLIF measurements in aqueous flows using the Nd:YAG laser. *Experiments in Fluids,* 23**,** 382-387.

KAZEMZADEH, A., EIN-MOZAFFARI, F., LOHI, A., PAKZAD, L. 2016. Effect of the Rheological Properties on the Mixing of Herschel-Bulkley Fluids with Coaxial Mixers: Applications of Tomography, CFD, and Response Surface Methodology. *Canadian Journal of Chemical Engineering,* 9999**,** 1-13.

KHAN, F. R., RIELLY, C. D. & HARGRAVE, G. K. 2004. A Multi-Block Approach to Obtain Angle-Resolved PIV Measurements of the Mean Flow and Turbulence Fields in a Stirred Vessel. *Chemical engineering & technology,* 27**,** 264-269.

KIM, J. Y., SONG, J. Y., LEE, E. J. & PARK, S. K. 2003. Rheological properties and microstructures of Carbopol gel network system. *Colloid and Polymer Science,* 281**,** 614-623.

KRESTA, S. M., ETCHELLS III, A. W., DICKEY, D. S. & ATIEMO-OBENG, V. A. 2015. *Advances in Industrial Mixing*.

KRESTA, S. M. & WOOD, P. E. 1993. The Mean Flow Field Produced by a 45-Degrees Pitched Blade Turbine - Changes in the Circulation Pattern Due to Off Bottom Clearance. *Canadian Journal of Chemical Engineering,* 71**,** 42-53.

KUKUKOVA, A., AUBIN, J. & KRESTA, S. M. 2009. A new definition of mixing and segregation: Three dimensions of a key process variable. *Chemical Engineering Research & Design,* 87**,** 633-647.

KUKUKOVA, A., AUBIN, J. & KRESTA, S. M. 2011. Measuring the Scale of Segregation in Mixing Data. *Canadian Journal of Chemical Engineering,* 89**,** 1122-1138.

LIU, M. Y. 2011. Computational study of convective-diffusive mixing in a microchannel mixer. *Chemical Engineering Science,* 66**,** 2211-2223.

LUO, J. Y., ISSA, R. I. & GOSMAN, A. D. 1994. Prediction of Impeller-Induced Flows in Mixing Vessels Using Multiple Frames of Reference. *IChemE Symposium Series,* 136 549–556.

MACOSKO, C. W. 1994. *RHEOLOGY: Principles, Measurements, and Applications*.

MARSHALL, E. M. & BAKKER, A. 2004. Computational fluid mixing. *Handbook of Industrial Mixing: Science and Practice***,** 257-343.

METZNER, A. & OTTO, R. 1957. Agitation of non-Newtonian fluids. *AIChE Journal,* 3**,** 3-10.

METZNER, A. B. & TAYLOR, J. S. 1960. Flow Patterns in Agitated Vessels. *Aiche Journal,* 6**,** 109-114.

MOFFAT, R. J. 1988. Describing the uncertainties in experimental results. *Experimental thermal and fluid science,* 1**,** 3-17.

MUZZIO, F. J., ALVAREZ, M. M., CERBELLI, S., GIONA, M. & ADROVER, A. 2000. The intermaterial area density generated by time- and spatially periodic 2D chaotic flows. *Chemical Engineering Science,* 55**,** 1497-1508.

MUZZIO, F. J., SWANSON, P. D. & OTTINO, J. M. 1991. The Statistics of Stretching and Stirring in Chaotic Flows. *Physics of Fluids a-Fluid Dynamics,* 3**,** 822-834.

NIENOW, A. & MILES, D. 1969. A dynamometer for the accurate measurement of mixing torque. *Journal of Physics E: Scientific Instruments,* 2**,** 994.

NIENOW, A. W., EDWARDS, M. & HARNBY, N. 1997. *Mixing in the process industries*, Butterworth-Heinemann.

NIENOW, A. W. & MILES, D. 1978. Effect of Impeller-Tank Configurations on Fluid-Particle Mass-Transfer. *Chemical Engineering Journal and the Biochemical Engineering Journal,* 15**,** 13-24.

OLIVIERI, G., GARGIULO, L., LETTIERI, P., MAZZEI, L., SALATINO, P. & MARZOCCHELLA, A. 2015. Photobioreactors for microalgal cultures: A Lagrangian model coupling hydrodynamics and kinetics. *Biotechnology Progress,* 31**,** 1259-1272.

OTTINO, J. 1989. The Kinematics of mixing: stretching, chaos, and transport. *Cambrige UP, Cambrige*.

PAKZAD, L., EIN-MOZAFFARI, F., UPRETI, S. R. & LOHI, A. 2013a. Agitation of Herschel-Bulkley fluids with the Scaba-anchor coaxial mixers. *Chemical Engineering Research & Design,* 91**,** 761-777.

PAKZAD, L., EIN-MOZAFFARI, F., UPRETI, S. R. & LOHI, A. 2013b. Characterisation of the mixing of non-newtonian fluids with a scaba 6SRGT impeller through ert and CFD. *Canadian Journal of Chemical Engineering,* 91**,** 90-100.

PAKZAD, L., EIN-MOZAFFARI, F., UPRETI, S. R. & LOHI, A. 2013c. A novel and energy-efficient coaxial mixer for agitation of non-Newtonian fluids possessing yield stress. *Chemical Engineering Science,* 101**,** 642-654.

PAPANASTASIOU, T. C., GEORGIOU, G. & ALEXANDROU, A. N. 2000. *Viscous Fluid Flow*, CRC-Press.

PATEL, D., EIN-MOZAFFARI, F. & MEHRVAR, M. 2011. Dynamic Performance of Continuous-Flow Mixing of Pseudoplastic Fluids Exhibiting Yield Stress in Stirred Reactors. *Industrial & Engineering Chemistry Research,* 50**,** 9377-9389.

PATEL, D., EIN-MOZAFFARI, F. & MEHRVAR, M. 2012. Improving the dynamic performance of continuous-flow mixing of pseudoplastic fluids possessing yield stress using Maxblend impeller. *Chemical Engineering Research & Design,* 90**,** 514-523.

PATEL, D., EIN-MOZAFFARI, F. & MEHRVAR, M. 2015. Effect of rheological parameters on non-ideal flows in the continuous-flow mixing of biopolymer solutions. *Chemical Engineering Research & Design,* 100**,** 126-134.

PAUL, E. L., ATIEMO-OBENG, V. A. & KRESTA, S. M. 2004. *Handbook of industrial mixing: science and practice,* Hoboken, NJ, John Wiley & Sons.

PAUL, P., VAN CRUYNINGEN, I., HANSON, R. & KYCHAKOFF, G. 1990. High resolution digital flowfield imaging of jets. *Experiments in fluids,* 9**,** 241-251.

RAMSAY, J., SIMMONS, M. J. H., INGRAM, A. & STITT, E. H. 2016. Mixing of Newtonian and viscoelastic fluids using "butterfly" impellers. *Chemical Engineering Science,* 139**,** 125-141.

REES, J. S. 2000. The prevalence of dentine hypersensitivity in general dental practice in the UK. *J Clin Periodontol,* 27**,** 860-5.

REES, J. S. & ADDY, M. 2002. A cross-sectional study of dentine hypersensitivity. *J Clin Periodontol,* 29**,** 997-1003.

RIEGER, F. & NOVAK, V. 1973. Power consumption of agitators in highly viscous non-Newtonian liquids. *Trans. Inst. Chem. Eng.,* 51**,** 105–111.

RUSHTON, J., COSTICH, E. & EVERETT, H. 1950. POWER CHARACTERISTICS OF MIXING IMPELLERS. 1. *Chemical Engineering Progress,* 46**,** 395-404.

SCHRAMM, G. 1994. *A practical approach to rheology and rheometry,* Haake Karlsruhe.

SHEKHAR, S. M. & JAYANTI, S. 2002. CFD study of power and mixing time for paddle mixing in unbaffled vessels. *Chemical Engineering Research and Design,* 80**,** 482-498.

SOSSA-ECHEVERRIA, J. & TAGHIPOUR, F. 2014. Effect of Mixer Geometry and Operating Conditions on Flow Mixing of Shear Thinning Fluids with Yield Stress. *Aiche Journal,* 60**,** 1156-1167.

SOSSA-ECHEVERRIA, J. & TAGHIPOUR, F. 2015. Computational simulation of mixing flow of shear thinning non-Newtonian fluids with various impellers in a stirred tank. *Chemical Engineering and Processing: Process Intensification,* 93**,** 66-78.

STOBIAC, V., FRADETTE, L., TANGUY, P. A. & BERTRAND, F. 2014. Pumping Characterisation of the Maxblend Impeller for Newtonian and Strongly Non-Newtonian Fluids. *Canadian Journal of Chemical Engineering,* 92**,** 729-741.

THIBAULT, F. & TANGUY, P. A. 2002. Power-draw analysis of a coaxial mixer with Newtonian and non-Newtonian fluids in the laminar regime. *Chemical Engineering Science,* 57**,** 3861-3872.

TORREZ, C. & ANDRE, C. 1999. Simulation of a Rushton turbine mixing yield stress fluids: Application of the Metzner-Otto concept. *Chemical Engineering & Technology,* 22**,** 701-706.

VERSTEEG, H. K. & MALALASEKERA, W. 2007. *An introduction to computational fluid dynamics: the finite volume method*, Pearson Education.

WESTERWEEL, J. & SCARANO, F. 2005. Universal outlier detection for PIV data. *Experiments in Fluids,* 39**,** 1096-1100.

YIANNESKIS, M., POPIOLEK, Z. & WHITELAW, J. 1987. An experimental study of the steady and unsteady flow characteristics of stirred reactors. *Journal of Fluid Mechanics,* 175**,** 537-555.

ZALC, J. M., SZALAI, E. S., ALVAREZ, M. M. & MUZZIO, F. J. 2002. Using CFD to understand chaotic mixing in laminar stirred tanks. *Aiche Journal,* 48**,** 2124-2134.

ZHANG, L. P., ZHANG, J., LI, C. H. & BAO, J. 2014. Rheological characterization and CFD modeling of corn stover-water mixing system at high solids loading for dilute acid pretreatment. *Biochemical Engineering Journal,* 90**,** 324-332.

ZHU, H., KIM, Y. & DE KEE, D. 2005. Non-Newtonian fluids with a yield stress. *Journal of Non-Newtonian Fluid Mechanics,* 129**,** 177-181.

ZLOKARNIK, M. 2003. *Stirring*, Wiley Online Library.

Appendixes

Appendix I. Rheology function in a parallel plate

In a parallel plate rheometer, the torque applied to the upper plate is (Chhabra and Richardson, 2011):

$$M = \int_{0}^{R} 2\pi\, \tau(r)\, r^2\, dr \qquad \text{(Eq. API.1)}$$

The shear rate at the rim of the plate for any type of fluid is as:

$$\dot{\gamma}_R = \frac{\Omega R}{h} \qquad \text{(Eq. API.2)}$$

The shear stress at the rim of the plate of a Newtonian fluid is as:

$$\tau_{R,N} = \frac{2M}{\pi R^3} \qquad \text{(Eq. API.3)}$$

The relation of the shear rate with the radius of the plate and the derivative of it is as:

$$r = \frac{\dot{\gamma} h}{\Omega} \qquad \text{(Eq. API.4)}$$

$$dr = \frac{h}{\Omega} d\dot{\gamma} \qquad \text{(Eq. API.5)}$$

It is necessary to change the integration variable from r to $\dot{\gamma}$:

$$M = \int_{0}^{\dot{\gamma}_R} 2\pi\, \dot{\gamma}^2 \left(\frac{h}{\Omega}\right)^2 \tau(\dot{\gamma}) \frac{h}{\Omega}\, d\dot{\gamma} \qquad \text{(Eq. API.6)}$$

Taking the constant terms out of the integral:

$$M = 2\pi\left(\frac{h}{\Omega}\right)^3 \int_0^{\dot{\gamma}_R} \dot{\gamma}^2\tau(\dot{\gamma})\, d\dot{\gamma} \qquad \text{(Eq. API.7)}$$

Combining Eq. API.3 and Eq. API.7:

$$\tau_{R,N}\frac{\pi R^3}{2} = 2\pi\left(\frac{R}{\dot{\gamma}}\right)^3 \int_0^{\dot{\gamma}_R} \dot{\gamma}^2\tau(\dot{\gamma})\, d\dot{\gamma} \qquad \text{(Eq. API.8)}$$

Rearranging Eq. API.8:

$$\tau_{R,N}\dot{\gamma}^3 = 4\int_0^{\dot{\gamma}_R} \dot{\gamma}^2\tau(\dot{\gamma})\, d\dot{\gamma} \qquad \text{(Eq. API.9)}$$

Derivating both sides of Eq. API.9 by $\dot{\gamma}$:

$$3\tau_{R,N}\dot{\gamma}^2 + \dot{\gamma}^3\frac{d\tau_{R,N}}{d\dot{\gamma}} = 4\dot{\gamma}^2\tau \qquad \text{(Eq. API.10)}$$

Dividing Eq. API.10 by $\dot{\gamma}^2$:

$$\tau_R = \frac{3}{4}\tau_{R,N} + \frac{\dot{\gamma}}{4}\frac{d\tau_{R,N}}{d\dot{\gamma}} \qquad \text{(Eq. API.11)}$$

Combining Eq. API.3 with Eq. API.11:

$$\tau_R = \frac{3}{4}\frac{2M}{\pi R^3} + \frac{\dot{\gamma}}{4}\frac{d\left(\frac{2M}{\pi R^3}\right)}{d\dot{\gamma}} \qquad \text{(Eq. API.12)}$$

Rearranging Eq. API.12:

$$\tau_R = \frac{M}{2\pi R^3}\left(3 + \frac{\dot{\gamma}}{M}\frac{d(M)}{d\dot{\gamma}}\right) \qquad \text{(Eq. API.13)}$$

The derivative of a natural logarithm is as:

$$\frac{1}{x}\,\mathrm{d}(x) = \mathrm{d}\ln(x) \qquad \text{(Eq. API.14)}$$

Finally, combining Eq. API.13 with Eq. API.14:

$$\tau_R = \frac{M}{2\pi R^3}\left[3 + \frac{\mathrm{d}\ln(M)}{\mathrm{d}\ln(\dot{\gamma}_R)}\right] \qquad \text{(Eq. API.15)}$$

I would like to thank Simona Miglozzi for the help provided in this Appendix I.

Appendix II. Coefficients of the power law model

In this Appendix II provide the values of the power law model coefficients (Eq. 2.7) that can be used to predict the viscosity of mixtures of the carbomer gel and glycerol for shear rates in the range of 1 – 250 s^{-1} and temperatures in the range of 25 – 85 ºC) (Tables APII. 1 and APII. 2).

The averaged percentage errors in the estimation of the *K* and *n* coefficients to be used in the power law model are presented in Table APII. 3.

Table APII. 1. Values of K [kg $s^{(n-2)}$ m^{-1}] for different temperatures and gel mass fractions

T [ºC]\ Gel mass fraction [ ]	1	0.9	0.8	0.7	0.6	0.5	0.4	0.3	0.2	0.1	0
25	518.9	499.8	407.2	431.0	284.4	268.45	132.5	69.56	32.77	6.123	1.000
30	360.3	358.4	310.8	317.5	222.3	180.75	102.1	45.88	22.11	3.604	0.600
35	301.2	320.8	275.5	276.1	194.1	156.20	84.99	37.79	17.84	2.834	0.400
40	291.5	287.1	249.6	247.5	172.6	137.82	73.88	32.28	14.85	2.279	0.300
45	266.9	262.9	227.8	225.3	155.8	123.35	65.71	28.21	12.78	1.848	0.200
50	243.6	242.1	209.9	206.0	141.5	111.70	59.11	25.12	11.09	1.519	0.150
55	222.6	220.0	190.3	186.0	128.8	101.90	51.58	22.48	9.732	1.243	0.120
60	200.1	204.2	175.3	171.9	119.0	94.16	45.91	19.98	8.326	0.9898	0.090
65	183.7	188.1	164.1	160.2	110.9	86.38	42.48	18.16	7.446	0.8405	0.070
70	172.2	178.4	154.8	151.0	103.3	81.31	38.77	17.27	7.048	0.7789	0.055
75	157.9	165.2	143.1	141.1	96.27	76.50	33.50	16.28	6.503	0.7199	0.040
80	144.5	153.5	131.5	132.0	91.35	71.79	28.93	15.26	5.889	0.6618	0.033
85	132.0	141.8	119.7	124.0	85.61	67.69	24.62	14.25	5.333	0.6181	0.026

Table APII. 2. Values of *n* for different temperatures and gel mass fractions

T [ºC]\ Gel mass fraction [ ]	**1**	**0.9**	**0.8**	**0.7**	**0.6**	**0.5**	**0.4**	**0.3**	**0.2**	**0.1**	**0**
25	0.3781	0.3868	0.3867	0.4112	0.4437	0.4453	0.4923	0.5533	0.6148	0.768	1.000
30	0.3732	0.3826	0.3911	0.4006	0.4342	0.4526	0.4833	0.5714	0.6403	0.8367	1.000
35	0.3663	0.3654	0.3779	0.3918	0.4223	0.4379	0.474	0.5604	0.6307	0.8271	1.000
40	0.3476	0.3574	0.3674	0.3798	0.4089	0.4259	0.4633	0.5493	0.6214	0.8179	1.000
45	0.3342	0.345	0.3551	0.3671	0.3963	0.4141	0.4512	0.5381	0.6096	0.8115	1.000
50	0.3245	0.3321	0.3415	0.3558	0.3845	0.4015	0.4392	0.5262	0.6006	0.805	1.000
55	0.3119	0.3277	0.3375	0.3509	0.3746	0.3883	0.436	0.5171	0.5933	0.8041	1.000
60	0.3266	0.328	0.3393	0.3462	0.3695	0.3843	0.4409	0.5176	0.6072	0.8198	1.000
65	0.3187	0.3229	0.3309	0.3379	0.357	0.3761	0.4273	0.5089	0.598	0.8117	1.000
70	0.2843	0.2859	0.2996	0.3112	0.3362	0.3492	0.402	0.4796	0.5617	0.7829	1.000
75	0.2741	0.2751	0.2898	0.2987	0.3275	0.3359	0.3974	0.4647	0.5495	0.7649	1.000
80	0.263	0.262	0.2818	0.286	0.31	0.3232	0.3937	0.4508	0.541	0.7488	1.000
85	0.2514	0.2504	0.2752	0.2721	0.2992	0.3071	0.3952	0.4396	0.5358	0.7294	1.000

Table APII. 3. Averaged percentage errors in the estimation of the *K* and *n* coefficients to be used in the power law model

T [ºC]\ Gel mass fraction [ ]	1	0.9	0.8	0.7	0.6	0.5	0.4	0.3	0.2	0.1	0
25	3.2%	4.3%	7.7%	4.8%	9.0%	6.3%	6.9%	6.7%	7.2%	7.5%	0.0%
30	7.7%	7.4%	8.2%	7.2%	8.3%	8.0%	7.0%	6.1%	5.0%	1.0%	0.0%
35	8.3%	8.1%	8.6%	7.0%	7.6%	7.7%	6.7%	5.6%	4.7%	0.9%	0.0%
40	8.1%	8.2%	8.4%	7.0%	7.5%	7.5%	6.5%	5.0%	4.3%	0.8%	0.0%
45	8.6%	8.5%	8.6%	7.2%	7.6%	7.4%	6.7%	4.8%	4.3%	0.8%	0.0%
50	8.9%	9.0%	9.1%	7.5%	7.9%	7.8%	6.8%	4.7%	4.2%	0.7%	0.0%
55	10.2%	9.0%	9.0%	7.6%	8.1%	7.9%	6.5%	4.6%	4.2%	0.6%	0.0%
60	7.2%	7.4%	7.4%	7.1%	7.5%	7.7%	5.7%	4.2%	2.9%	3.5%	0.0%
65	7.2%	7.1%	7.2%	7.0%	8.0%	7.8%	6.1%	4.3%	2.9%	2.7%	0.0%
70	10.4%	10.6%	9.9%	9.2%	9.5%	9.5%	7.6%	6.1%	5.2%	0.4%	0.0%
75	11.1%	11.2%	10.3%	10.0%	9.8%	9.9%	8.1%	6.7%	5.5%	0.7%	0.0%
80	11.7%	12.0%	10.4%	10.7%	10.8%	10.7%	8.4%	7.3%	5.8%	1.1%	0.0%
85	12.5%	12.6%	10.6%	11.6%	11.2%	11.4%	8.2%	7.8%	5.7%	1.7%	0.0%

Appendix III. Coefficients of the Herschel Bulkley model

In this Appendix, I provide the values of the Herschel-Bulkley model parameters (Eq. 2.9) that can be used to predict the viscosity of mixtures of the carbomer gel and glycerol for shear rates in the range of 1 – 250 s^{-1} and temperatures in the range of 25 – 85 ºC (Tables APIII. 1, APIII. 2 and APIII. 3).

The averaged percentage errors in the estimation coefficients to be used in the Herschel-Bulkley model are presented in Table APIII. 4.

Table APIII. 1. Values of τ_0 [Pa] for different temperatures and gel mass fractions for the Herschel-Bulkley model

T [ºC]\ Gel mass fraction [ ]	1	0.9	0.8	0.7	0.6	0.5	0.4	0.3	0.2	0.1	0
25	39.24	38.00	39.24	37.78	30.66	27.78	15.27	9.232	0	0	0
30	34.17	34.14	30.72	30.55	23.63	20.34	11.78	6.062	0	0	0
35	29.46	29.91	27.00	25.70	19.63	16.62	9.459	4.757	0	0	0
40	26.30	26.55	23.62	22.64	16.87	14.25	7.949	3.853	0	0	0
45	21.83	23.96	21.38	20.31	15.25	12.43	6.989	3.285	0	0	0
50	21.51	22.02	19.61	18.44	13.42	11.16	6.154	2.858	0	0	0
55	19.86	19.37	17.01	16.38	12.43	10.14	5.276	2.515	0	0	0
60	14.76	15.30	13.44	13.39	10.08	8.160	4.143	1.509	0	0	0
65	13.45	13.91	12.18	12.30	9.424	7.446	3.774	1.644	0	0	0
70	14.71	15.49	13.42	13.11	9.406	7.804	3.845	1.913	0	0	0
75	13.50	14.44	12.28	12.27	8.902	7.267	3.380	1.798	0	0	0
80	12.35	13.40	11.06	11.53	8.401	6.774	2.912	1.680	0	0	0
85	11.35	17.94	9.939	10.88	7.707	6.427	2.462	1.552	0	0	0

Table APIII. 2. Values of *K* [kg s(n^{-2}) m^{-1}] for different temperatures and gel mass fractions for the Herschel-Bulkley model

T [ºC]\ Gel mass fraction [ ]	1	0.9	0.8	0.7	0.6	0.5	0.4	0.3	0.2	0.1	0
25	480.9	463.0	370.6	395.4	263.0	243.1	118.9	61.66	32.77	6.123	1.000
30	328.4	326.5	282.3	289.1	199.9	162.4	91.56	40.70	22.11	3.604	0.600
35	294.2	292.7	250.4	252.0	175.9	141.1	76.49	33.67	17.84	2.834	0.400
40	266.7	262.2	227.4	226.2	156.1	124.8	66.68	28.89	14.85	2.279	0.300
45	245.2	240.3	207.7	206.1	141.8	111.9	59.35	25.31	12.78	1.848	0.200
50	223.2	221.3	191.5	188.6	129.2	101.4	53.49	22.58	11.09	1.519	0.150
55	203.8	201.6	174.2	170.5	118.0	92.50	46.75	20.23	9.732	1.24	0.120
60	185.7	189.4	162.3	159.0	110.5	86.45	42.02	18.58	8.326	0.9898	0.090
65	170.6	174.6	152.3	148.4	103.3	79.33	38.94	16.63	7.446	0.8405	0.070
70	158.1	163.6	142.0	138.5	95.68	74.00	35.21	15.55	7.048	0.7789	0.055
75	145.0	151.4	131.4	129.4	90.10	69.67	30.38	14.66	6.503	0.7199	0.040
80	132.7	140.6	120.9	121.0	85.05	65.41	26.24	13.74	5.889	0.6618	0.033
85	121.1	125.0	110.2	113.6	79.75	61.62	22.34	12.84	5.333	0.6181	0.026

Table APIII. 3. Values of *n* for different temperatures and gel mass fractions for the Herschel-Bulkley model

T [ºC]\ Gel mass fraction [ ]	**1**	**0.9**	**0.8**	**0.7**	**0.6**	**0.5**	**0.4**	**0.3**	**0.2**	**0.1**	**0**
25	0.3970	0.4061	0.4060	0.4318	0.4463	0.4670	0.5170	0.5810	0.6148	0.7680	1
30	0.3919	0.4018	0.4106	0.4206	0.4483	0.4752	0.5074	0.6000	0.6403	0.8367	1
35	0.3786	0.3837	0.3968	0.4114	0.4334	0.4598	0.4977	0.5884	0.6307	0.8271	1
40	0.3650	0.3753	0.3858	0.3987	0.4233	0.4472	0.4865	0.5768	0.6214	0.8179	1
45	0.3509	0.3623	0.3728	0.3855	0.4090	0.4348	0.4738	0.5650	0.6096	0.8115	1
50	0.3407	0.3487	0.3585	0.3735	0.4019	0.4216	0.4612	0.5525	0.6006	0.8050	1
55	0.3275	0.3441	0.3543	0.3684	0.3905	0.4077	0.4578	0.5429	0.5933	0.8041	1
60	0.3429	0.3444	0.3563	0.3635	0.3885	0.4035	0.4629	0.5378	0.6072	0.8198	1
65	0.3346	0.3390	0.3474	0.3548	0.3791	0.3949	0.4486	0.5333	0.5980	0.8117	1
70	0.2985	0.3002	0.3145	0.3268	0.3580	0.3666	0.4221	0.5036	0.5617	0.7829	1
75	0.2878	0.2888	0.3043	0.3136	0.3455	0.3527	0.4173	0.4879	0.5495	0.7649	1
80	0.2762	0.2751	0.2959	0.3003	0.3313	0.3394	0.4134	0.4733	0.5410	0.7488	1
85	0.2640	0.2630	0.2890	0.2857	0.3228	0.3225	0.4150	0.4616	0.5358	0.7294	1

Table APIII. 4. Errors in the Herschel-Bulkley model

T [ºC]\ Gel mass fraction [ ]	1	0.9	0.8	0.7	0.6	0.5	0.4	0.3	0.2	0.1	0
25	2.1%	3.0%	7.0%	3.5%	7.3%	5.7%	5.9%	5.5%	7.2%	7.5%	0.0%
30	7.3%	7.0%	7.7%	6.6%	7.5%	7.3%	6.2%	4.7%	5.0%	1.0%	0.0%
35	7.2%	7.7%	8.2%	6.3%	7.1%	6.9%	5.9%	4.2%	4.7%	0.9%	0.0%
40	7.7%	7.8%	7.9%	6.4%	6.9%	6.8%	6.2%	3.6%	4.3%	0.8%	0.0%
45	8.2%	8.1%	8.3%	6.7%	7.5%	6.8%	6.0%	3.4%	4.3%	0.8%	0.0%
50	8.6%	8.7%	8.8%	7.0%	7.1%	7.2%	6.2%	3.4%	4.2%	0.7%	0.0%
55	9.6%	8.3%	8.3%	6.9%	7.9%	7.9%	5.9%	3.5%	4.2%	0.6%	0.0%
60	6.6%	6.7%	6.8%	6.4%	6.5%	6.6%	4.7%	3.3%	2.9%	3.5%	0.0%
65	6.7%	6.5%	6.5%	6.3%	6.5%	6.9%	5.1%	3.1%	2.9%	2.7%	0.0%
70	10.2%	10.2%	9.7%	8.9%	8.3%	9.4%	7.1%	5.3%	5.2%	0.4%	0.0%
75	10.9%	11.1%	10.1%	9.8%	9.0%	10.0%	7.7%	6.0%	5.5%	0.7%	0.0%
80	11.6%	11.9%	10.2%	10.6%	9.8%	10.6%	8.0%	6.8%	5.8%	1.1%	0.0%
85	12.4%	13.5%	10.3%	11.5%	9.9%	11.8%	7.8%	7.3%	5.7%	1.7%	0.0%

Appendix IV. Power curves for all experiments in Chapter 3

In this Appendix, I present all the power curves from Chapter 3 in Figures APIV. 1 to APIV. 10.

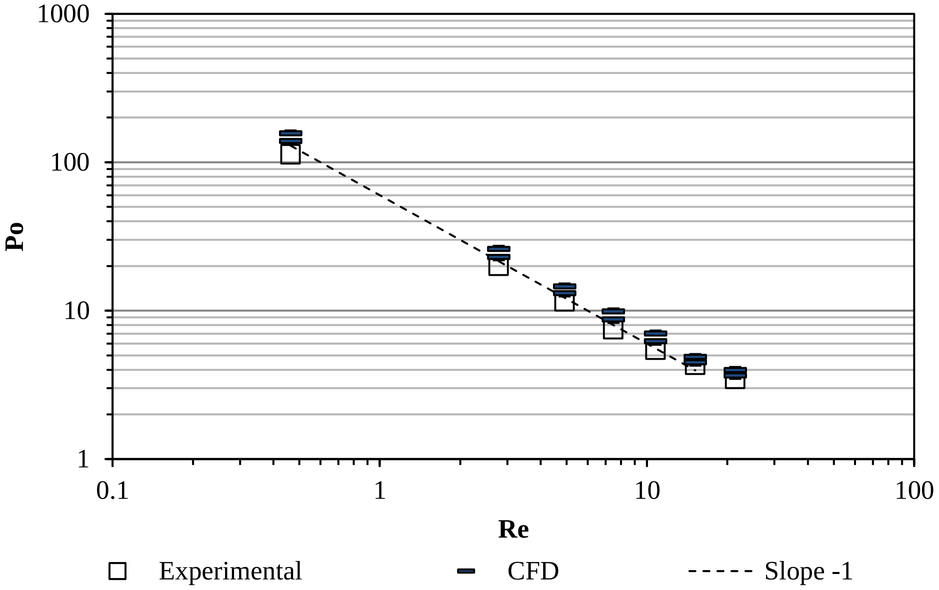

Figure APIV. 1. Power curve for 20% gel mass fraction and 40 ºC

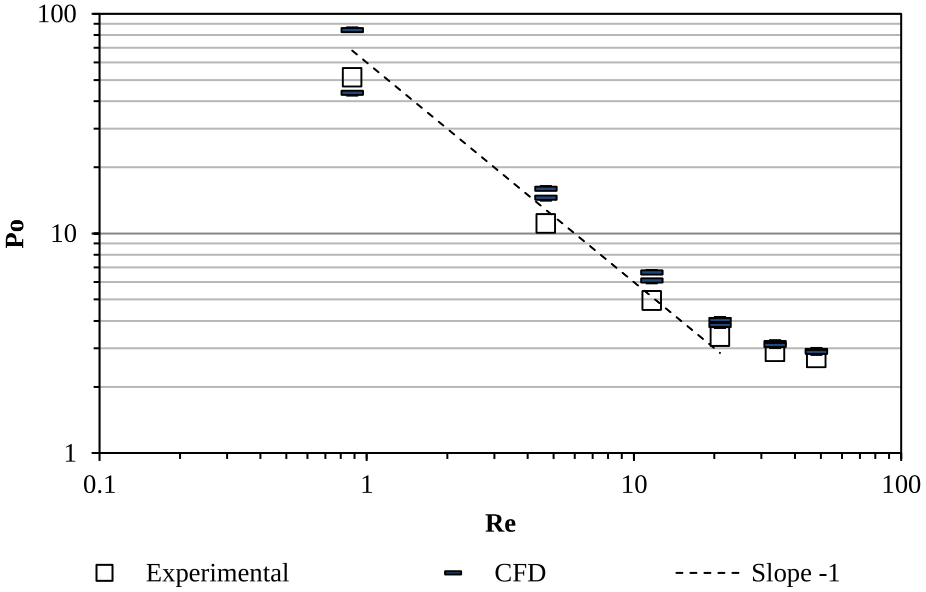

Figure APIV. 2. Power curve for 20% gel mass fraction and 60 ºC

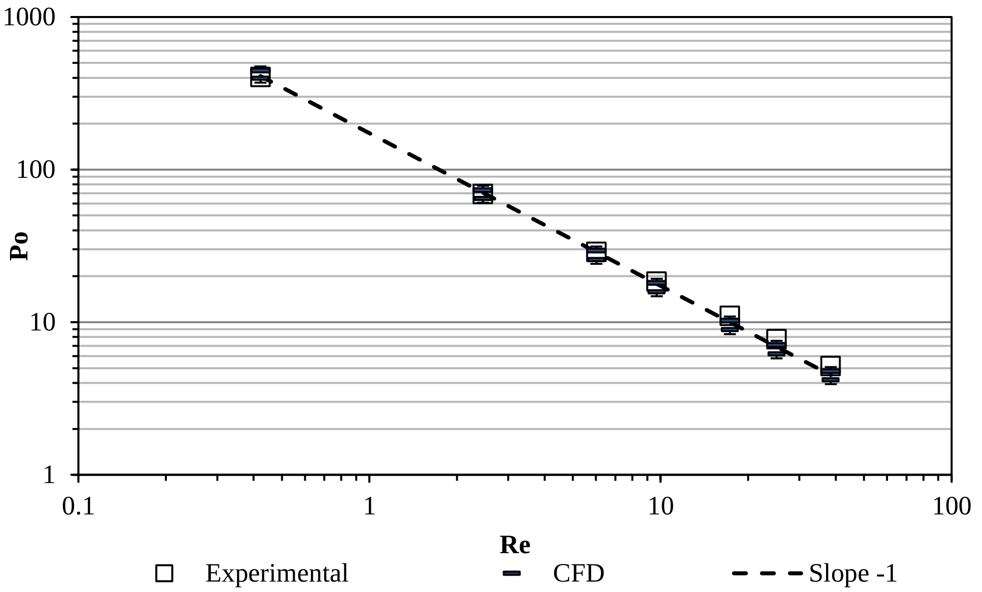

Figure APIV. 3. Power curve for 40% gel mass fraction and 40 ºC

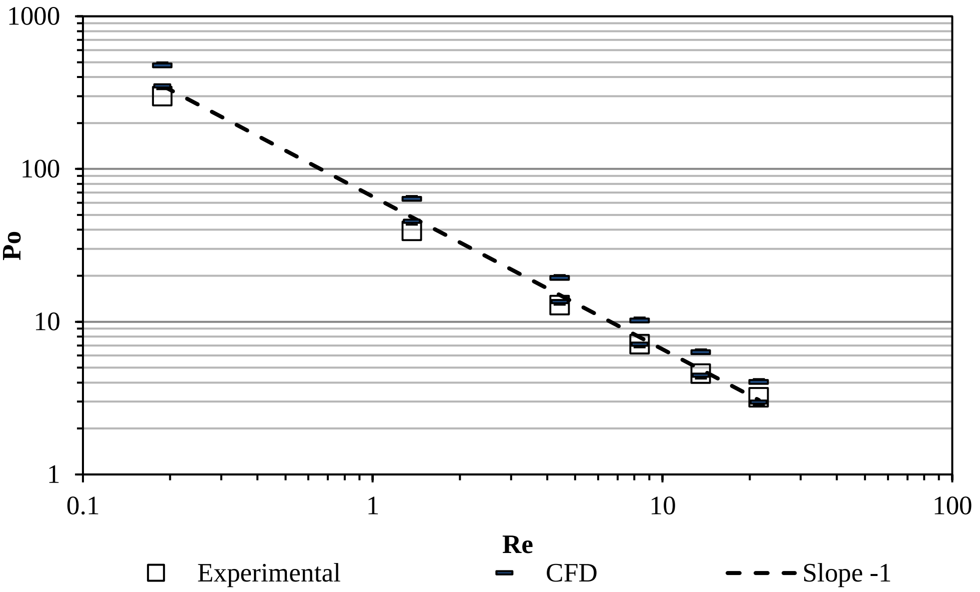

Figure APIV. 4. Power curve for 40% gel mass fraction and 60 ºC

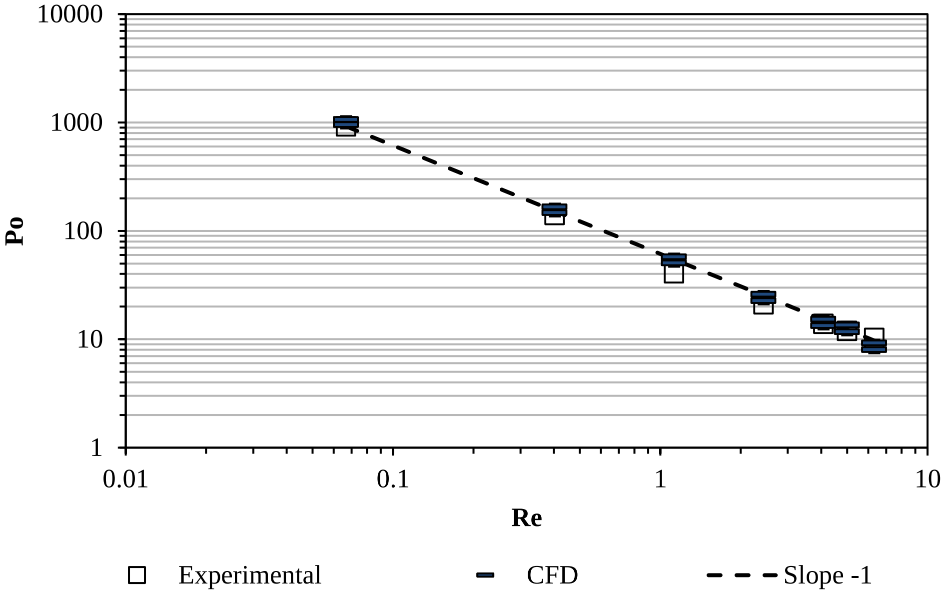

Figure APIV. 5. Power curve for 60% gel mass fraction and 40 ºC

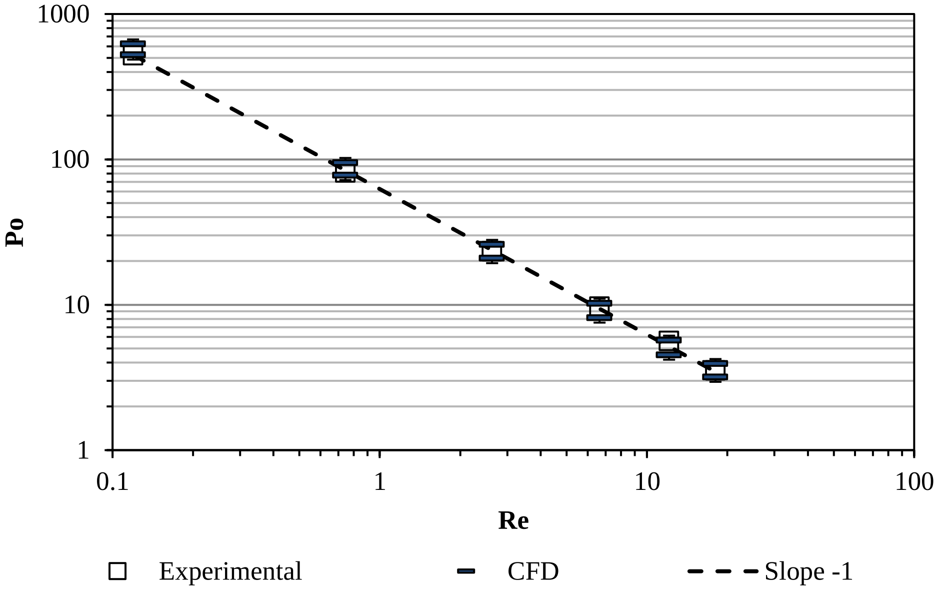

Figure APIV. 6. Power curve for 60% gel mass fraction and 60 ºC

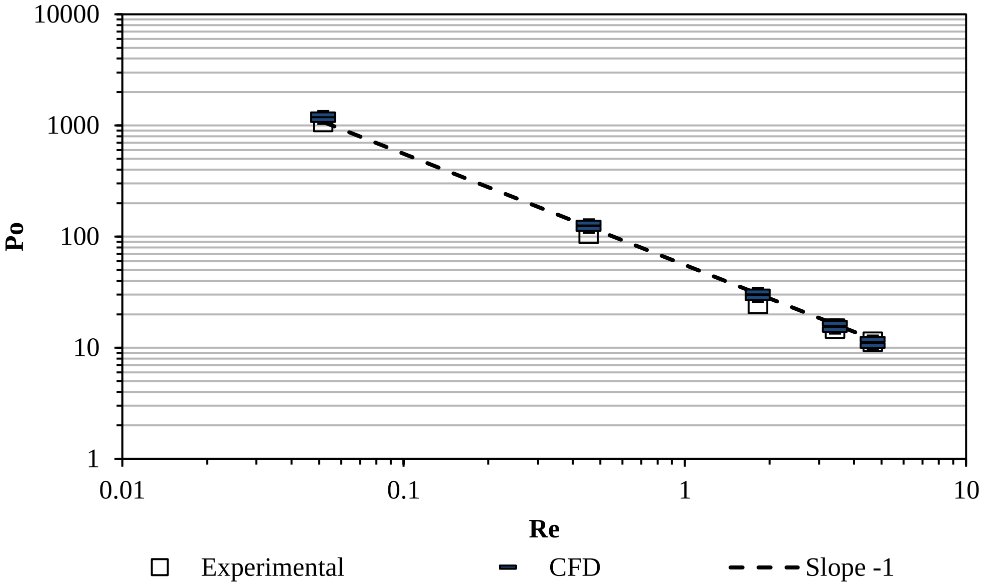

Figure APIV. 7. Power curve for 80% gel mass fraction and 40 ºC

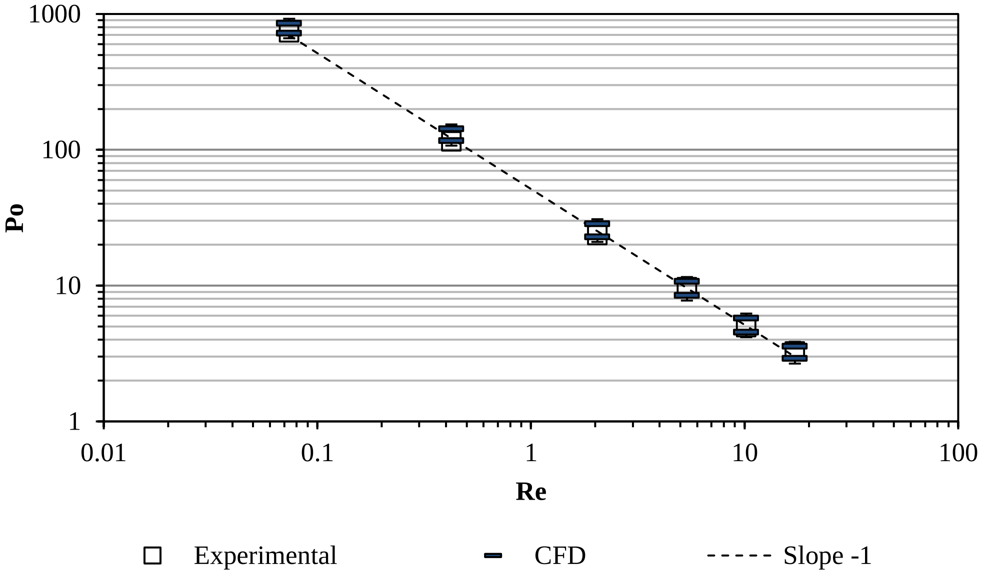

Figure APIV. 8. Power curve for 80% gel mass fraction and 60 ºC

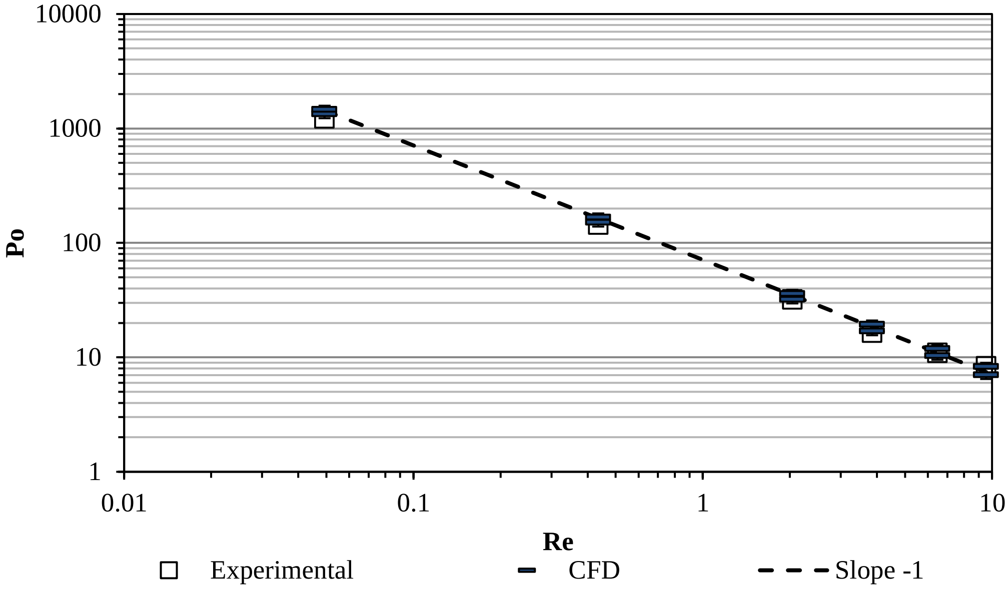

Figure APIV. 9. Power curve for 100% gel mass fraction and 40 ºC

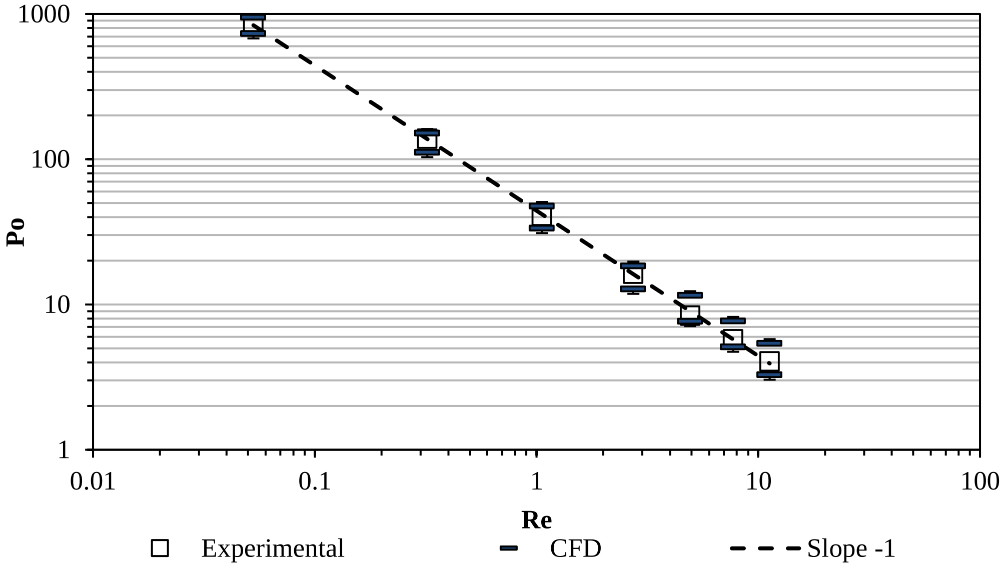

Figure APIV. 10. Power curve for 100% gel mass fraction and 60 ºC

Appendix V. Eulerian vs Lagrangian stretching

In this Appendix, I aim to prove that the Eulerian formulation of the stretching is equivalent to the Lagrangian one. I divide this Appendix into two subsections; the first one considers a simple two-dimensional shear flow and the second one considers a simple rotational flow.

Appendix V.1. Simple two-dimensional shear flow

Let me take as an example a 2D shear flow between 2 parallel plates separated by **L** on the vertical direction. The top one moves at a velocity of $\mathbf{v_t} = \begin{bmatrix} u \\ 0 \end{bmatrix}$, and the one on the bottom is stationary: $\mathbf{v_b} = \begin{bmatrix} 0 \\ 0 \end{bmatrix}$. Let me assume that the fluid in-between the parallel plates has a Newtonian behaviour. The velocity profile can be represented as in Figure APV.1:

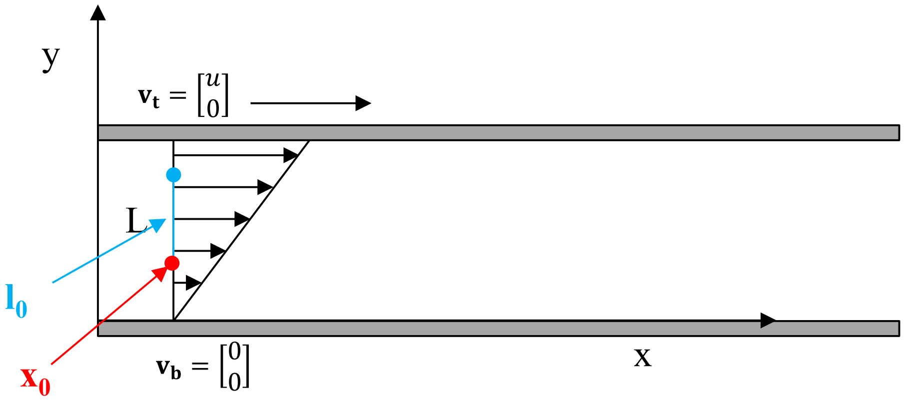

Figure APV. 1. Velocity profile of a simple shear flow produced by two parallel plates where the top one moves at v_t and the bottom one is stationary. A flow element is represented in light blue for the Eulerian perspective. Additionally, two particles are introduced in the flow, one on each extreme of the flow element for the Lagrangian study.

Appendix V.1.1. Eulerian approach

A fluid element of infinitesimal size l_0 with origin on x_0 is introduced in the flow. This is also shown in Figure APV.1. I aim to find an analytical solution for the stretching of the fluid element. To do so, I use Equations 5.8 and 5.9.

$$\frac{d\mathbf{l}}{dt} = (\nabla\mathbf{v})^T \cdot \mathbf{l}, \qquad \text{(Eq. 5.8 bis)}$$

$$\lambda(t) = \frac{|\mathbf{l}(t)|}{|\mathbf{l}_0|} \qquad \text{(Eq. 5.9 bis)}$$

The velocity at any point of the fluid element is:

$$\mathbf{v} = \begin{bmatrix} u(y) \\ 0 \end{bmatrix} \qquad \text{(Eq. APV.1)}$$

The transposed of the velocity gradient is:

$$(\boldsymbol{\nabla}\mathbf{v})^T = \begin{bmatrix} 0 & \frac{u}{L} \\ 0 & 0 \end{bmatrix} \qquad \text{(Eq. APV.2)}$$

In this case, Eq 5.8 is rearranged as:

$$\frac{d}{dt}\begin{bmatrix} l_x \\ l_y \end{bmatrix} = (\nabla\mathbf{v})^T \cdot \begin{bmatrix} l_x \\ l_y \end{bmatrix} = \begin{bmatrix} 0 & \frac{u}{L} \\ 0 & 0 \end{bmatrix} \cdot \begin{bmatrix} l_x \\ l_y \end{bmatrix} = \begin{bmatrix} \frac{u}{L} l_y \\ 0 \end{bmatrix} \qquad \text{(Eq. APV.3)}$$

The analytical solution of Eq 5.8 is:

$$\begin{cases} \frac{d\, l_x}{dt} = \frac{u}{L} l_y \rightarrow l_x = \frac{u}{L} l_{y0} t + l_{x0} \\ \frac{d\, l_y}{dt} = 0 \rightarrow l_y = cnt = l_{y0} \equiv \mathrm{l}_0 \end{cases} \qquad \text{(Eq. APV.4)}$$

From the initial conditions of the example shown in Figure APV.1: $l_{x0} = 0$

Appendix V.1.2. Lagrangian approach

An alternative approach to compute the stretch is to compute the distance between the two extremes of the fluid element as function of time. This can be done through a Lagrangian tracking of massless particles introduce on each extreme of the fluid element. In the absence of diffusion, the particles will move using the following equation:

$$\mathbf{x}_{t+1} = \mathbf{x}_t + \mathbf{v}\Delta t \qquad \text{(Eq. APV.5)}$$

where $\mathbf{x}_t$ and $\mathbf{x}_{t+1}$ are the positions of the particles at times t and t+1 respectively, Δt is the time difference between t and t+1, and $\mathbf{v}$ is the velocity of the particle. For this method to be successful, $\mathbf{v}$ must be known at each point of the domain. This is true for the system shown in Figure APV.1. For a particle at any $\mathbf{x}_0 = \begin{bmatrix} x_0 \\ y_0 \end{bmatrix}$, the equation that describes the movement of the particle is:

$$\begin{bmatrix} x_t \\ y_t \end{bmatrix} = \begin{bmatrix} x_0 \\ y_0 \end{bmatrix} + \begin{bmatrix} \frac{u}{L} y_0 \\ 0 \end{bmatrix} t \qquad \text{(Eq. APV.6)}$$

The position of the two particles can be tracked over time, and the stretch of the fluid element at any time is given by:

$$\lambda(t) = \frac{\sqrt{\left(x_{P1,t} - x_{P2,t}\right)^2 + \left(y_{P1,t} - y_{P2,t}\right)^2}}{\sqrt{\left(x_{P1,0} - x_{P2,0}\right)^2 + \left(y_{P1,0} - y_{P2,0}\right)^2}} \qquad \text{(Eq. APV.7)}$$

Appendix V.1.3. Comparison of the two approaches

The two methods are compared for the case shown in Figure APV.1. The conditions for this study are: $\mathbf{v} = \begin{bmatrix} 1 \\ 0 \end{bmatrix}$ [cm/s]; $L = 1$ [cm].

The initial conditions for the explicit case are: $\mathbf{x}_0 = \begin{bmatrix} 0 \\ 0.995 \end{bmatrix}$ [cm]; $\mathbf{l}_0 = \begin{bmatrix} 0 \\ 0.005 \end{bmatrix}$ [cm].

Similarly, the initial conditions for the particle tracking are: $\mathbf{x}_{P1,0} = \begin{bmatrix} 0 \\ 0.995 \end{bmatrix}$ [cm]; $\mathbf{x}_{P2,0} = \begin{bmatrix} 0 \\ 1 \end{bmatrix}$ [cm];

The stretch is computed using both methods for the first 6 seconds. The results are presented in Figure APV. 2. It is clear that both methods are equivalent.

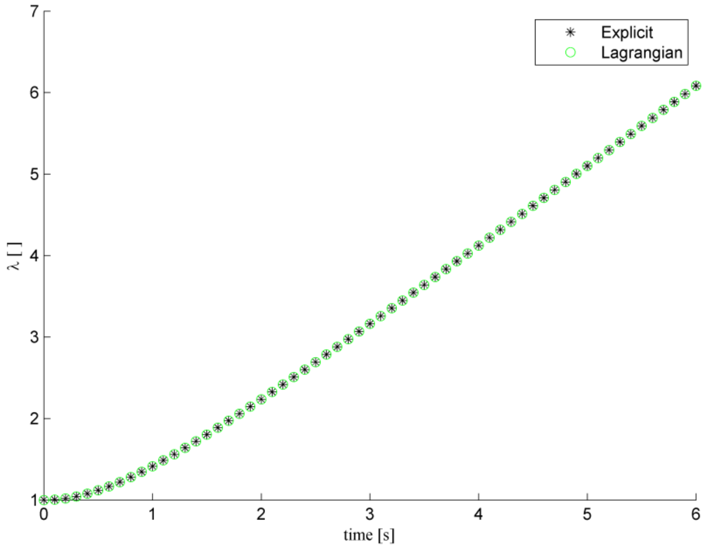

Figure APV. 2. Stretching of the fluid using both the Eulerian (Explicit) and the Lagrangian approaches

The position of the two particles is shown against time in Figure APV. 3.

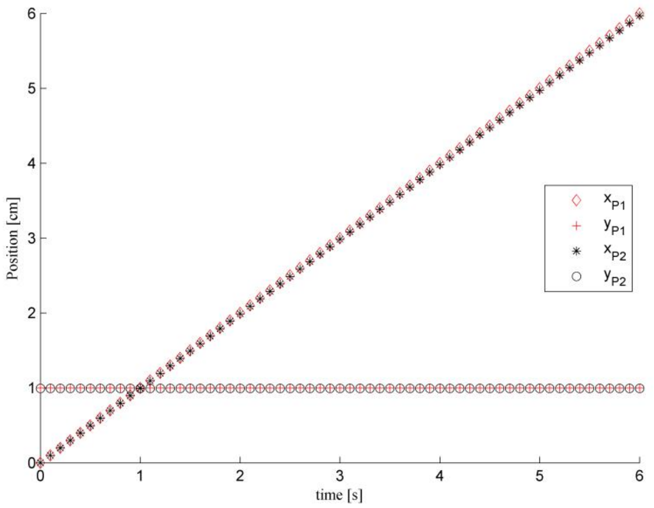

Figure APV. 3. Position of the two particles against time

Appendix V.2. Simple rotational flow

In Appendix V.1.3 it was shown that the computation of the stretch of a fluid element is equivalent using both the Eulerian and the Lagrangian interpretation of fluids for a simple two-dimensional linear shear flow. To fully convince myself that the Lagrangian tracking of particles can be used to compute the stretch of fluid elements in a mixing tank, I decided to first study the stretch of fluid elements in a simple rotational flow. The simplest case of a purely rotational flow is that of a circle that rotates at $\boldsymbol{\omega}$ [rad/s], as shown in Figure APV.4.

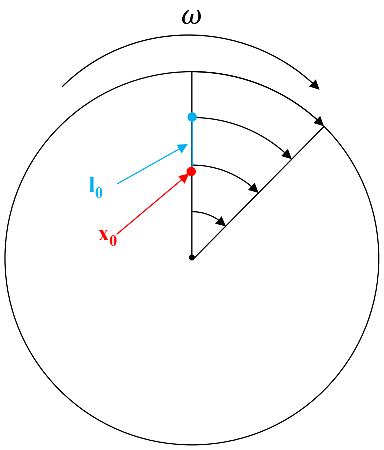

Figure APV. 4. Velocity profile of a simple rotational flow produced by a circle rotating at a constant angular speed ω. A flow element is represented in light blue for the Eulerian perspective. Additionally, two particles are introduced in the flow, one on each extreme of the flow element for the Lagrangian study.

Using the Cartesian coordinates system, any point inside the cylinder is defined:

$$\mathbf{x} = \begin{bmatrix} x \\ y \end{bmatrix} = \begin{bmatrix} r\cos(\theta) \\ r\sin(\theta) \end{bmatrix} \qquad \text{(Eq. APV.8)}$$

where $\theta = \theta_0 + \omega t$.

The velocity at any point of the fluid element is:

$$\mathbf{v} = \begin{bmatrix} v_x \\ v_y \end{bmatrix} = \begin{bmatrix} -\omega r \sin(\theta_0 + \omega r t) \\ \omega r \cos(\theta_0 + \omega r t) \end{bmatrix} = \begin{bmatrix} -\omega y \\ \omega x \end{bmatrix} \qquad \text{(Eq. APV.9)}$$

The transposed of the velocity gradient is:

$$(\boldsymbol{\nabla}\mathbf{v})^T = \begin{bmatrix} 0 & \omega \\ -\omega & 0 \end{bmatrix} \qquad \text{(Eq. APV.10)}$$

Using the equations 5.8 and APV.10:

$$\frac{d}{dt}\begin{bmatrix} l_x \\ l_y \end{bmatrix} = \begin{bmatrix} 0 & \omega \\ -\omega & 0 \end{bmatrix} \cdot \begin{bmatrix} l_x \\ l_y \end{bmatrix} = \begin{bmatrix} \omega l_y \\ -\omega l_x \end{bmatrix} \qquad \text{(Eq. APV.11)}$$

Now I have:

$$\begin{cases} \dfrac{dl_x}{dt} = \omega l_y \\ \dfrac{dl_y}{dt} = -\omega l_x \end{cases} \qquad \text{(Eq. APV.12)}$$

Differentiating both equations over time:

$$\begin{cases} \dfrac{d^2 l_x}{dt^2} = \omega \dfrac{dl_y}{dt} = -\omega^2 l_x \\ \dfrac{d^2 l_y}{dt^2} = -\omega \dfrac{dl_x}{dt} = -\omega^2 l_y \end{cases} \qquad \text{(Eq. APV.13)}$$

The analytical solution of Equations APV.12 is:

$$\begin{cases} l_x(t) = C_1 \cos(\omega t) + C_2 \sin(\omega t) \\ l_y(t) = C_3 \cos(\omega t) + C_4 \sin(\omega t) \end{cases} \qquad \text{(Eq. APV.14)}$$

The four constants need to be found. Using the initial conditions:

$$l_x(t=0) = 0 \rightarrow C_1 = 0 \qquad \text{(Eq. APV.15)}$$

$$l_y(t=0) = l_{y0} \rightarrow C_3 = l_{y0} \qquad \text{(Eq. APV.16)}$$

From the first part of EQ APV.12:

$$C_2 \omega \cos(\omega t) - C_1 \omega \sin(\omega t) = \omega[C_4 \sin(\omega t) + C_3 \cos(\omega t)] \qquad \text{(Eq. APV.17)}$$

Evaluating Eq. APV.17 at t=0:

$$C_2 = C_3 = l_{y0} \qquad \text{(Eq. APV.18)}$$

From the second part of EQ APV.12:

$$C_4\omega\cos(\omega t) - C_3\omega\sin(\omega t) = -\omega[C_2\sin(\omega t) + C_1\cos(\omega t)] \qquad \text{(Eq. APV.19)}$$

Evaluating Eq. APV.19 at t=0:

$$C_4 = -C_1 = 0 \qquad \text{(Eq. APV.20)}$$

Finally, the four constants are substituted in Eq. APV.14:

$$\begin{cases} l_x(t) = l_{y0}\sin(\omega t) \\ l_y(t) = l_{y0}\cos(\omega t) \end{cases} \qquad \text{(Eq. APV.21)}$$

The stretch of the fluid element at any time is given by:

$$\lambda(t) = \frac{l_{y0}\sqrt{(\sin(\omega t))^2 + (\cos(\omega t))^2}}{l_{y0}} = 1 \qquad \text{(Eq. APV.22)}$$

As can be seen from Eq. APV.22, the flow does not stretch the fluid.

To finalise this study, I also perform the Lagrangian tracking of particles at the end points of the fluid element. of each particle is Eq. APV.5. The stretch of the fluid element using the Lagrangian tracking is computed as in Eq. APV.7.

The two methods are compared for the case shown in Figure APV.4. The conditions for this study are: $\omega = 1$ [rad/s]**;** R= 1 [cm].

The initial conditions for the explicit case are:

$\mathbf{x}_0 = \begin{bmatrix} 0 \\ 0.95 \end{bmatrix}$ [cm]; $\mathbf{l}_0 = \begin{bmatrix} 0 \\ 0.05 \end{bmatrix}$ [cm];

Similarly, the initial conditions for the particle tracking are: $\mathbf{x}_{P1,0} = \begin{bmatrix} 0 \\ 0.95 \end{bmatrix}$ [cm]; $\mathbf{x}_{P2,0} = \begin{bmatrix} 0 \\ 1 \end{bmatrix}$ [cm];

The stretch is computed using both methods for the first 6 seconds. The results are presented in Figure APV.5. It is clear that both methods are also equivalent in this case.

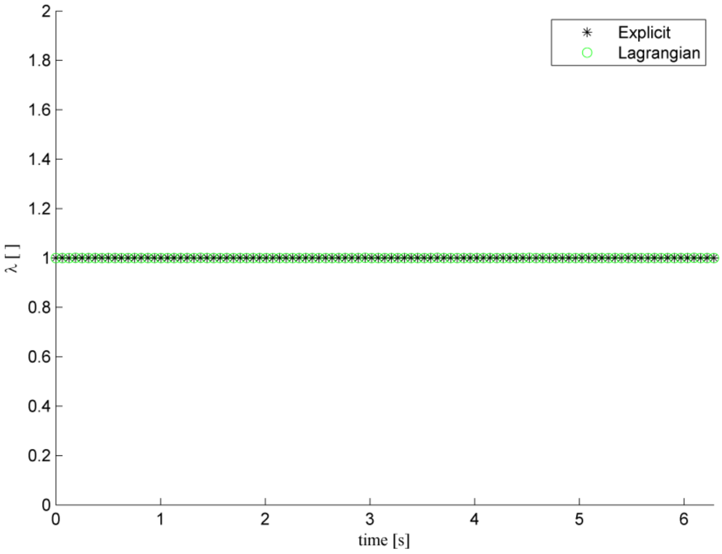

Figure APV. 5. Stretching of the fluid using both the Eulerian (Explicit) and the Lagrangian approaches

The position of the two particles is shown against time in Figure APV.6.

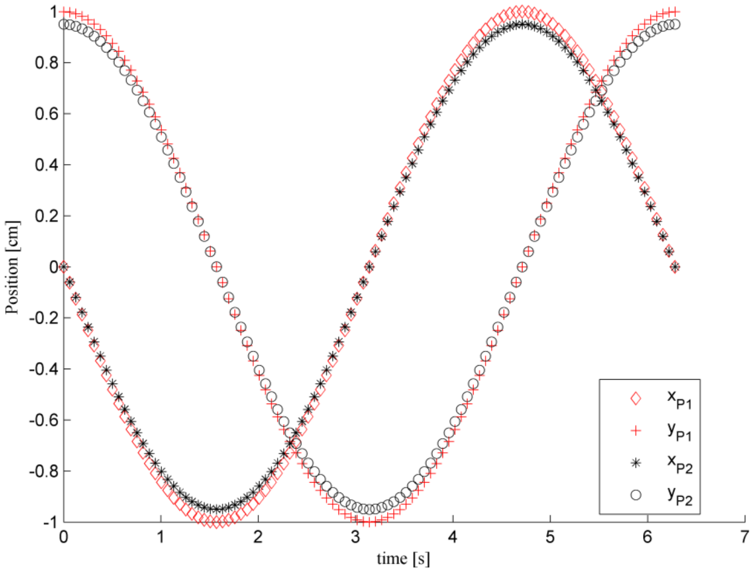

Figure APV. 6. Position of the two particles against time